Title

In Situ and Operando X-ray Spectroscopy Studies of Solid/Gas and Solid/Liquid Interfaces

Permalink

https://escholarship.org/uc/item/5g21n37z

Author

Wu, Chenghao

Publication Date

2015

Peer reviewed|Thesis/dissertation

In Situ and *Operando* X-ray Spectroscopy Studies of Solid/Gas and Solid/Liquid Interfaces

by

Chenghao Wu

A dissertation submitted in partial satisfaction of the

requirements for the degree of

Doctor of Philosophy

in

Chemistry

in the

Graduate Division

of the

University of California, Berkeley

Committee in Charge:

Professor Miquel B. Salmeron, Co-Chair
Professor Tanja Cuk, Co-Chair
Professor Gabor A. Somorjai
Professor Nitash P. Balsara

Summer 2015

In Situ and *Operando* X-ray Spectroscopy Studies of Solid/Gas and Solid/Liquid Interfaces

Copyright © 2015

by Chenghao Wu

Abstract

In Situ and *Operando* X-ray Spectroscopy Studies of Solid/Gas and Solid/Liquid

Interfaces

by

Chenghao Wu

Doctor of Philosophy in Chemistry

University of California, Berkeley

Professor Miquel B. Salmeron, Co-Chair

Professor Tanja Cuk, Co-Chair

Gas-phase catalytic reactions and electrochemical reactions are two important categories of heterogeneous reactions. In order to determine the reaction mechanisms and potentially improve the technologies based on these reactions, it is essential to understand what happens at relevant solid/gas or solid/liquid interfaces under reaction conditions. X-ray photoelectron spectroscopy (XPS) and x-ray absorption spectroscopy (XAS) are two element-specific and chemical-state-specific characterization techniques. Recently, researchers have demonstrated that with proper modifications, these vacuum-requiring techniques can also be used to characterize various solid/gas or solid/liquid interface systems under ambient conditions, which opens the way towards *in situ* and *operando* characterization of many heterogeneous reaction systems. In this dissertation, the studies on two solid/gas interface systems and two solid/liquid interface systems are presented.

The solid/gas interface systems were characterized by ambient-pressure XPS (AP-XPS). In the study regarding Co catalyst for Fischer-Tropsch (F-T) synthesis, it was found that CO adsorbs strongly on Co surface; but small amount of sulfur substantially weakens the CO adsorption and consequently poisons the F-T reaction. Under reaction conditions, Co surface remains metallic. At lower temperatures, water molecules in the reaction products can potentially oxidize the Co surface and thereby hinder the catalytic reaction. When the reaction temperature is above 250°C, H_2 is responsible for reducing Co to its metallic phase and keeping the catalyst active. In the study of Co_xPd_y alloy nanoparticles for catalyzing CO oxidation reaction, a clear dependence of catalytic activities on

1

nanoparticle composition was observed. AP-XPS results revealed that Co segregates to the surface and stays in the oxide form after the pretreatment process. Small amount of Co coexisting with Pd on the surface can promote the CO oxidation reaction synergistically and the synergetic effect becomes more prominent with increasing Co content. However, when Co/Pd ratio is too high, after the cleaning processes, the surface of the nanoparticles is fully covered by thin layers of CoO_x, preventing CO molecules from binding with Pd, which leads to significant drop in catalytic activity of the alloy nanoparticles.

The solid/liquid interface systems were characterized by our newly developed *in situ* and *operando* XAS technique. Total electrode yield (TEY) signal collected through the working electrode can provide information that is sensitive to the solid/liquid interfaces. At Au/H_2O interfaces, the hydrogen-bonding network is greatly disrupted by the interface, leaving more broken hydrogen bonds than in bulk water. But the delocalization of the LUMO orbitals of water molecules into the gold substrate, greatly suppresses the pre-edge feature in O*1s* XAS spectrum that is typically associated with broken hydrogen bonds. These polar molecules can respond to external electrical field and reorient at the interface, producing potential-dependent O*1s* TEY XAS spectra. At Pt/H_2SO_4(aq) or Au/H_2SO_4(aq) interfaces, similar water reorientation behaviors were observed in the negative potential region. In the positive potential regions, the evolution of O*1s* XAS spectra is different from that of Au/H_2O system. The changes in the spectra are possibly related to the adsorption of sulfate ions at the interface, contradicting many reports that proposed an oxide formation or oxygen/ hydroxyl adsorption processes.

The studies on four interface systems presented in this dissertation illustrate the capabilities and great potentials of these two *in situ* x-ray spectroscopy techniques, i.e., AP-XPS and *in situ*/*operando* XAS, in the investigation of interfacial phenomena and reaction mechanisms in various heterogeneous reactions. Such mechanistic information can potentially provide insightful guidance for better designs of catalysts and electrode materials.

Dedicated to my dearest parents and grandparents.

Table of Contents

Acknowledgements

Until this day, I still have a vivid memory about the moment when I received the offer letter from UC Berkeley. I was so excited that I couldn't help spreading the good news right away. In August 2009, I first set foot on the United States and started my new adventure in a foreign country. Back then, I was this young man, who had never travelled abroad, or known anyone in Berkeley, or even spoken English for a full day. I was a little scared, but also quite enthusiastic about the new life here, as well as all kinds of new opportunities in it.

Time flies and it has been six years since then. It started smoothly at the beginning. I made some friends shortly after I arrived. Some of them became my best friends later on, who were extremely helpful and supportive during my entire PhD, especially during my most difficult time in 2012. After two months of searching, I joined a research group that I really liked and started to work on a project that I was really excited about. However, the situation started to deteriorate in the second year. I couldn't move my project forward for some reasons and my advisor began to lose faith in me. I was frequently asked to switch projects in my third year, which made me struggle quite a bit. At the end of my third year, I had achieved very little, no first-author publications, no conference presentations. Nevertheless, I had learned a great deal from my fellow students and colleagues, not only the knowledge regarding semiconductor physics, electrochemistry, materials characterization and related skills, but also the strategy, philosophy, and ethics in academic research. I want to specially thank Dr. Anthony Fu and Dr. Anna P. Goldstein, my fellow students, who joined the group together with me in 2009. They were extremely helpful and I learned a lot from them. Particularly, with their help, my English was improved a lot during the first three years. All of us struggled together for three years, and they have already gone through the fight a little earlier than me. I wish them all the best in their future career. I also want to thank Dr. Chris Hahn, my mentor when I first joined the group, who taught me about materials synthesis, characterization and electrochemistry. I am also very grateful to many brilliant group members, visitors, and collaborators, including Dr. Yunjeong Hwang, Dr. Chong Liu, Dr. Sarah Brittman, Dr. Melissa Fardy, Dr. Sean Andrews, Dr. Ruoxue Yan, Dr. Michael Moore, Dr. Jongwoo Lim, Prof. Frank Tsung, Dr. Ziyang Huo, Prof. Jinyao Tang, Prof. Zhaoyu Zhang, Prof. Bin Liu, Prof. Hao-Ming Chen, Prof. Xing Yi Ling, Prof. Candace Chan, Dr. Tung-Po Hsieh, Prof. Hanwei Gao, Prof. Neil Dasgupta, Prof. Chen Chen, Prof. Yonghui Deng, Prof. Aidi Zhao, Dr. Steve Shelton, Dr. Andy Zheng.

My enthusiasm for research, as well as my pride, had been almost exhausted at the end of the third year. I even started to think about alternative way out, for example, quitting the

PhD program. I also tried to explore other possibilities, such as switching to data science, and I even got a M.A. degree in statistics as a byproduct. My hesitation and struggle continued for a couple of months, during which the feeling of uncertainty and insecurity tortured me constantly. At the beginning of my fourth year, inspired and encouraged by several friends, I made a decision: I wanted to give myself a second chance in academic research, but in a different research group. This was rather a difficult decision, especially in the fourth year of my PhD. When many of my classmates had started to think about when to finish up their PhD and about the next step after graduation, I started to search for a research group again. During that period, talking to many friends, colleagues, and faculty members really inspired me and helped me a lot in the searching process. I want to specially thank Prof. Miquel Salmeron, Prof. Tanja Cuk and Prof. Delia Milliron, who listened to me patiently, shared their own experience during their PhD period, and gave me invaluable and honest advice. I also want to thank Dr. Zhongwei Zhu, Dr. Xiaofeng Feng, Prof. Bin Liu, Prof. Frank Tsung, Prof. Qiao Zhang and many others friends, who were extremely supportive and helpful. In addition, I am very grateful to the department staff that helped me deal with all the complications during the transition period.

In October 2012, Prof. Miquel Salmeron offered me a position to work on *in situ* and *operando* x-ray spectroscopy. Joining his group turned out to be one of the best decisions that I have ever made. I am extremely grateful to Prof. Salmeron for offering me a second chance in my PhD. He has been incredibly understanding, kind and supportive, and let me explore many of my "stupid" ideas since then. I also want to specially thank Dr. Juan J. Velasco-Velez and Dr. Sophie Carenco, whom I closely worked with for about two years. They were extremely patient with me, although I had absolutely no experience in synchrotron spectroscopy at that time. They taught me a lot about XAS and AP-XPS, which led to what I have achieved so far. I also want to thank many other members in the Salmeron group, including Dr. Xiaofeng Feng, Dr. Baran Eren, Mr. Huixin Wang, Prof. Haitao Fang, Ms. Mahati Chintapalli, Dr. Barbara A.J. Lechner, Dr. Sara Barja, Dr. Nikos Liakakos, Dr. Robert S. Weatherup, Dr. Christian Heine, Dr. Yingjie Zhang, Dr. Wei Bao, Mr. Alex Buyanin.

In the meantime, I have been involved in several collaboration projects, such as Li-S battery project with Prof. Nitash Balsara and his group, time-resolved XPS and XAS study of interfacial charge transfer with Dr. Oliver Gessner and his group, and first-principle XAS simulations with Dr. Prendergast and his group. Through these collaborations, I learned plenty of new knowledge from the experts in these different fields. I am grateful to all of these brilliant minds that I worked with, in particular, Dr. Tod Pascal, Mr. Kevin Wujcik, Dr. Stefan Neppl, and Dr. David Prendergast.

Because I intensively worked at the Advanced Light Source, I had a lot of interaction with the scientists, staff and students there. Without their hard work to maintain the machines and provide user support, I could not get this far. In particular, I want to thank the beamline scientists, Dr. Jinghua Guo at BL 8.0.1 and BL 6.3.1, Dr. Hendrik Bluhm at BL 11.0.2, Dr. Zhi Liu and Dr. Ethan Crumlin at BL 9.3.2, as well as their groups. The great support from many people at ALS, such as Dr. Yi-Sheng Liu, Dr. Andrey Shavorskiy, Dr. Per-Anders Glans-Suzuki, Dr. Xuefei Feng, Mr. Yifan Ye, Mr. Duo Zhang, Mr. Yu-Cheng Shao, Ms. Kaiqi Nie, is greatly appreciated.

I want to thank all my friends, especially those at Berkeley during my PhD, to keep me optimistic and happy in my life outside the lab. These friends include Dr. Lei Cheng, Dr. Xiaofeng Feng, Dr. Pengcheng Zhang, Dr. Ziyang Huo, Dr. Miao Zhang, Dr. Hongwei Li, Ms. Fangfang Ren, Dr. Jie Zhang, Dr. Ying Qiao, Dr. Zhaoyi Kang and many others. I want to specially thank Dr. Zhongwei Zhu, my best friend, who was also my roommate for almost four years. I cannot imagine how I could survive the six years without his help.

At last, I want to thank my dearest parents and grandparents. Thank you so much for indulging me to pursue the seemingly endless PhD in a foreign country. Thank you for being there for me no matter what difficult situations or bad mood I was in. I am truly sorry that I didn't get many opportunities to go back home and accompany them. Now it is almost the end. I want to dedicate this dissertation to them, my dearest parents and grandparents.

Chapter 1

Introduction

Abstract

This chapter discusses the importance of solid/gas interfaces and solid/liquid interfaces with relevance to gas-phase catalysis and electrochemistry, and the difficulties to characterize these interfaces under realistic conditions. Deep understanding of the physical and chemical properties of these interfaces, especially under catalysis- or electrochemistry-relevant conditions, is essential in the mechanistic study of various heterogeneous reactions. Existing *in situ* characterization techniques are also briefly introduced and their drawbacks are discussed.

1.1 Heterogeneous Reactions and Interfaces

Chemical reactions can generally be divided into two categories: homogeneous reactions and heterogeneous reactions. Homogeneous reactions occur in a single phase, gas, liquid, or solid, for example, the combustion of flammable gases, the reactions between acid and base in aqueous solutions, etc. In homogeneous reactions, the substances that participate in the reactions are distributed in the system as simple gas molecules, solvent molecules, solvated ions, and the like. The reaction mechanisms of such reactions primarily depend on the interactions of the reacting substances, which are simpler and easier to understand from the theoretical point of view.

Heterogeneous reactions involve multiple phases with at least one condensed phase, because gaseous substances are always well mixed into one phase. In almost all the heterogeneous reactions, different reactants need to migrate to the interfaces between different phases, encounter with each other, and then undergo chemical changes at the interfaces. Consequently, heterogeneous reactions are inevitably influenced by many factors other than just the interactions between reactants, for instance, the transport properties of the reactants in each phase, the chemical composition and physical properties of the interfaces, and the chemical and physical changes that some reactants undergo when they pass through the interfaces. All these factors make heterogeneous reactions much more complicated than homogeneous reactions and thus more difficult to understand.

Gas-phase catalysis and electrochemical reactions are two categories of heterogeneous reactions that attract most attention in the research community. Both of them have a great many important industrial applications. Two distinct types of interfaces are involved in these two categories of heterogeneous reactions: solid/gas interfaces in gas-phase catalysis and solid/liquid interfaces in electrochemical reactions. Each type of the interfaces has its own unique properties and presents different challenges for *in situ* characterization. The physical properties of the interfaces and the chemical processes at the interfaces are the key information for the understanding of reaction mechanisms and kinetics in these heterogeneous reactions.

1.1.1 Gas-Phase Catalysis and Solid/Gas Interfaces

Gas-phase reactions are typically considered as homogeneous reactions. But for some of the gas-phase reactions, the participation of a solid catalyst, such as metal nanoparticles, mesoporous oxides, or metal nanoparticles dispersed on oxide support, can alter the reaction pathway and substantially reduce the activation barrier of the reactions, which further leads to faster kinetics, lower reaction temperatures, and potentially lower energy

input and production cost. Many of the reactions in oil refinery and related industry involve such gas-phase catalysis, which produce petroleum and other important chemicals such as additives, lubricants, and raw materials for other chemical industry.[1,2] Another example is the CO oxidation and NO_x decomposition reactions catalyzed on various metal surfaces,[3,4] such as platinum, palladium, ruthenium, and copper, or transition metal oxides.[5] Such reactions convert poisonous and polluting exhaust gases into non-toxic molecules, such as CO_2 and N_2, and therefore have positive environmental impact. Many automobile manufacturers have already incorporated such catalysts in different cars, to reduce the air pollution caused by exhaust gases. Other gas-phase catalytic reactions of industrial importance include ammonium synthesis, Fischer-Tropsch synthesis, water gas shift reaction, steam reforming reaction, etc.

Figure 1-1 schematically illustrates a typical solid/gas interface. The gas-phase catalytic reaction at such interface involves a series of complex processes. The first step usually involves the adsorption of one or more reactant gas molecules at different sites on the catalyst surface, as illustrated in the purple circle A. The interaction between the adsorbed molecules and the catalyst can profoundly alter the surface structure of the catalyst, as well as the electronic structure of both the adsorbate and the substrate. Some molecules
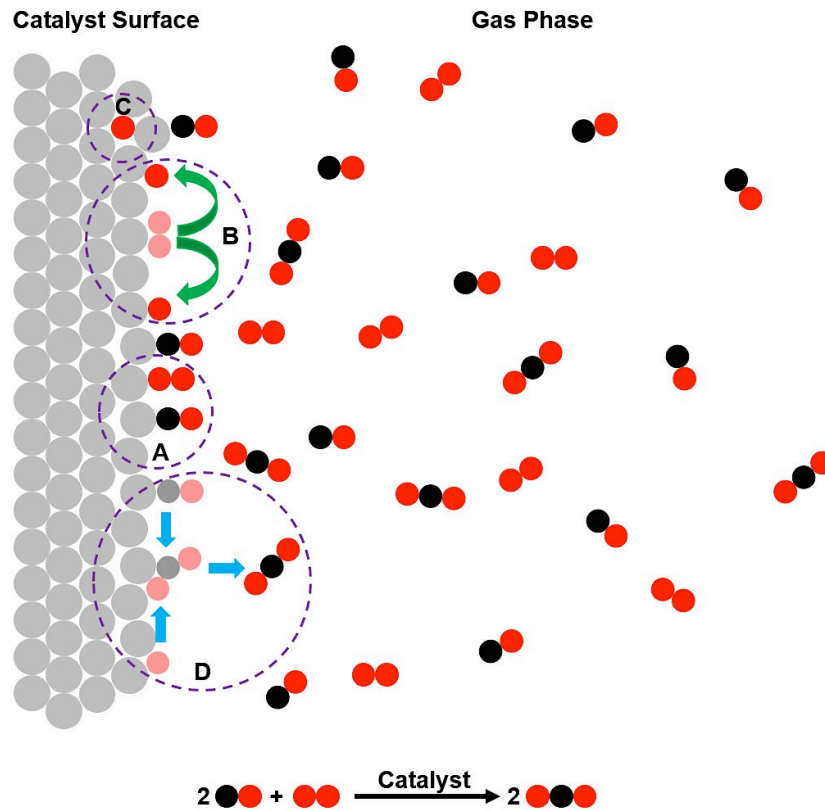

Figure 1-1. A schematic illustration of a typical solid/gas interface.

3

will decompose on the catalyst surface and break into reactive fragments such as radicals and atomic species, as illustrated in circle B. Some atomic species can even penetrate into the sub-surface regions (circle C). These activated molecules and reactive fragments can migrate on the catalyst surface at reaction temperatures. When they encounter with each other, reaction intermediates start to form and eventually evolve into the reaction products and desorb from the catalyst surface (circle D).

In the past, various single crystal surfaces, as model catalysts, have been studied by a variety of surface techniques, such as scanning tunneling microscopy (STM), low energy electron diffraction (LEED), and x-ray photoelectron spectroscopy (XPS). However, traditional surface techniques require ultra-high vacuum (UHV).[1,6] Therefore, most of the measurements on different catalyst surfaces were performed in vacuum by brief exposure of the surface to the reactants. In order to obtain a low desorption rate compatible with the low partial pressure required, the surfaces are often kept at cryogenic temperatures. Such experimental conditions are far from equilibrium and thus the information obtained may not be entirely relevant in the catalysis context. It has been demonstrated in recent years that more realistic conditions, i.e. higher pressures ($>10^{-6}$ Torr) and higher temperatures (at least room temperature), can profoundly alter the structure of the catalyst surfaces, or more precisely the solid/gas interfaces.[7,8] For instance, at pressure of 10^{-6} Torr and above, the surface is usually covered with a dense layer of adsorbates. Moreover, the surface species, not only the adsorbates but also the substrates, can be extremely dynamic.[9,10]

1.1.2 Electrochemistry and Solid/Liquid Interfaces

Electrochemical reactions also have serious impact on different aspects of industry as well as our daily life. For instance, electrochemical corrosion of different metals and anti-corrosion coatings have serious impact on the long-term stability of these metals immersed in various electrolytes such as sea water, and therefore the long-term safety of large vessels that are made of these metal materials. More importantly, the global demand for energy has increased tremendously in the past few decades. Many researchers around the world are devoted to improve the current technologies or develop sustainable new technologies to boost overall energy production and enable effective storage of this energy. Electrochemistry stands at the center of many energy technologies. For example, the lithium intercalation into the electrode materials is the key process in various lithium ion batteries, which power all the portable electronic devices or even electrical vehicles nowadays. Efficient electrolysis, particularly the (photo)electrolysis of water and (photo) reduction of CO_2, can potentially produce clean chemical fuels, such as hydrogen gas or hydrocarbons, by using clean energy source such as sun light. In order to improve the efficiency or performance of energy-related technologies, it is important and necessary to

understand the reaction mechanism in these important electrochemical systems.

According to classical electrochemistry theory, the solid/liquid interface, as illustrated in Figure 1-2, also known as electrical double layer (EDL) or Helmholtz layer, plays a vital role in many electrochemical systems.[11] Most important elemental processes take place at such interfaces, for example, the accumulation and selective adsorption of ions on the electrode surface, the solvation/de-solvation process of ions and the re-organization of solvent molecules, charge transfer between the electrode and electrolyte, ion intercalation into the electrode, etc. Although classical EDL theories, mostly continuum theories, have been established and widely accepted for almost a century, the molecular-level details of such interfaces during electrochemical reaction are much less well understood. For example, in a lithium ion battery system, the following questions remain (at least partly) unanswered: How does the solid/electrolyte interface or interphase (SEI) form? What is the composition of the SEI layer? How do the solvated lithium ions escape from the solvation shell, pass through the SEI layer and intercalate into the electrode materials? Considering the importance of the SEI formation and ion intercalation mechanism in battery systems, the answer to these questions will provide useful insights relevant to the development and improvement of the next-generation batteries.
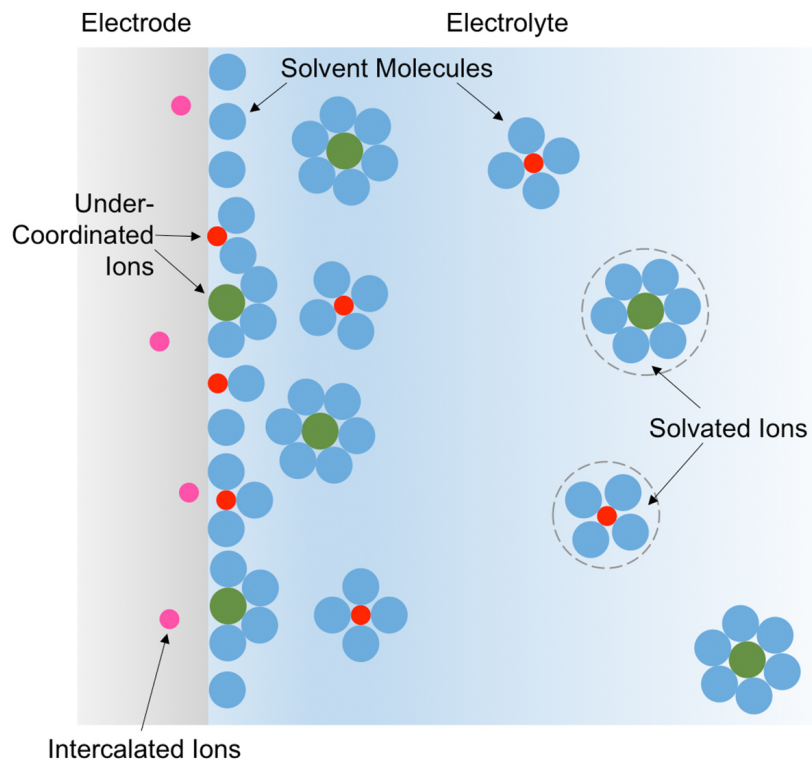

Figure 1-2. A schematic illustration of a typical solid/liquid interface.

Nevertheless, to experimentally characterize such solid/liquid interface is even more challenging than characterizing solid/gas interface. The difficulties mostly arise from the large-quantity of condensed matter on both sides of the interface. A variety of *ex-situ* characterization techniques have been explored in the past to characterize such interfaces,[12–18] but in most cases the electrode surfaces, as well as the loosely adsorbed species at the interface, undergo inevitable changes when taken out of the solution and transferred into the measurement chamber.[19]

1.2 Existing *In Situ* Techniques for Interface Characterization

Over the past decades, a variety of *in situ* characterization techniques have emerged, allowing scientists to investigate various solid/gas interfaces under realistic conditions. Examples include environmental scanning electron microscopy (E-SEM),[20] environmental transmission electron microscopy (E-TEM),[21,22] surface-sensitive or surface-enhanced vibrational spectroscopy,[23,24] grazing-incidence hard x-ray diffraction and spectroscopy,[6] etc. E-TEM is a particularly powerful technique. With the development of aberration-corrected high-resolution TEM and incorporation of differentially pumped sample stages, researchers are now able to study the detailed structure and chemical changes of nano-catalysts under different gas environment. Another useful technique is sum frequency generation (SFG) spectroscopy. The selection rules governing the non-linear optical processes in SFG guarantee a very high surface sensitivity.[25]

Although the UHV requirement once limited the application of the traditional surface science techniques in the characterization of solid/gas interface under realistic conditions, in the past decade, scientists have successfully demonstrated that, with proper modifications, traditional surface characterization techniques can be used for *in situ* and *operando* characterization of solid/gas interfaces. High-pressure STM (HP-STM)[26] and ambient-pressure XPS (AP-XPS)[7,27] are two of the successful examples. It has been demonstrated in our group that with a home-built STM instrument housed in a high-pressure cell,[26] one can measure various single crystal surfaces under different gas environment, up to 700 Torr. It is also possible to implement HP-STM techniques at elevated temperatures, where high-speed scanning is required to cope with the thermal drift.[28,29] By incorporating differential pumping systems as well as electrostatic focusing system into the XPS analyzer,[27] one can collect XPS spectra *in situ* and *operando* in the presence of different gases, up to a few Torr. These modifications bring the traditional surface characterization into the catalysis-relevant temperature and pressure range, which enables new discoveries in various catalytic systems under realistic conditions.[7,8] AP-

XPS is the main technique used in the studies of solid/gas interfaces presented in this dissertation. The details about the AP-XPS instrumentation will be described in Chapter 2.

In situ characterization of solid/liquid interfaces is even more challenging than that of solid/gas interfaces. In order to characterize solid/liquid interfaces *in situ*, one would need a probe, such as a metal tip, photons, or electrons, which can penetrate the solid and/or the liquid layer, while generating collectable signals solely from the interface layer (typically several nanometers thick) without interference from the bulk solid or bulk liquid. Meanwhile, because of Brownian motion and other thermal movement, the interface, especially the interfacial liquid layer, is extremely dynamic under ambient conditions. Therefore, fast probing tools are needed, at least faster than the time scale of the thermal movement of interfacial species; otherwise, the signal will simply average out both in space and in time domains.

Many of the above-mentioned *in situ* techniques for solid/gas interface characterization have been explored for solid/liquid interface characterization, such surface-sensitive and surface-enhanced vibrational spectroscopy,[25,30–35] grazing-incidence hard x-ray diffraction/scattering[19,36,37] and spectroscopy,[38–41] E-TEM,[42–44] etc. STM technique can also be modified into so-called electrochemical STM (EC-STM) to characterize solid/liquid interface *in situ* and *operando*. Although the information obtained from *in situ* studies by these techniques has collectively enriched the knowledge of various solid/liquid interfaces, each of the methods has their own advantages and disadvantages.

EC-STM has been utilized to investigate many electrochemical systems, including the adsorption of various halide ions on different metal surfaces,[45,46] Cu under-potential deposition[15,47] on noble metal surfaces, interfaces between various metals and H_2SO_4 solutions,[48–50] to name a few. Various absorbate-induced surface superstructures were observed at these interfaces. However, such scanning probe techniques have a few obvious drawbacks. First of all, such techniques typically require single crystal surfaces or large domains of atomically flat surfaces, which limits their application in more practical electrochemical systems, where the electrode surfaces are usually polycrystalline and rough. Secondly, scanning requires physical movement of the tip, which dictates the slow imaging rate, with respect to the time scale of the thermal movement of the species at the interfaces. As a result, STM can only be used to measure the structural changes of the electrode surface or the surface adsorbates that are strongly bonded to the surface and barely move. Another potential problem with proximal probes (STM, or atomic force microscope, AFM) is the sub-nanometer distance between the probe and the surface, which can perturb the structure of the EDL during the measurement.

Photon-matter and electron-matter interactions are usually much faster than Brownian motion in a solution or at the solid/liquid interface. Therefore, probing the interface with beams of photons and electrons makes it possible to capture snapshots of the dynamic interfaces. Surface-sensitive and surface-enhanced vibrational spectroscopies, such as surface-enhanced infrared and Raman spectroscopy[34,35,50] and sum frequency generation (SFG) spectroscopy,[25] use infrared and/or visible photons to probe the vibrations of the chemical bonds at the interfaces. But vibrational spectroscopies can only provide information regarding chemical bonds at the interface, meaning that the structural information at the interface can only be derived indirectly. X-ray diffraction and scattering are capable of determining the long-range or short-range periodicity based on the diffraction or elastic scattering of x-ray photons by the structure of the specimen. Operating in grazing-angle incidence or reflection geometry can greatly reduce the probing depth of x-ray photons, which is typically referred to as surface x-ray diffraction and scattering.[19,36,37] However, grazing-incidence and reflection geometry imposes stringent requirements on the surface flatness of the sample. Moreover, the data analysis typically requires extensive curve fitting and heavily relies on prior knowledge of the interface, such as presumed reconstructed superstructures at the electrode surfaces. TEM and related techniques (such as energy dispersive x-ray spectroscopy, EDS, and electron energy loss spectroscopy, EELS) use electrons to probe the detailed structure as well as element distribution of miniature objects. The development of E-TEM enables such observations of liquid samples[42,43,51–53] and even solid/liquid interfaces.[54] Because the electrons have to pass through the entire thickness of the specimen in TEM, the thickness of the specimen has to be very thin, typically tens of nanometers. As a result, the application of TEM and related techniques is most successful in the observation of nanoparticles or other miniature structures sandwiched inside liquid cells.

1.3 Organization of Thesis

This dissertation is organized in 5 chapters. Chapter 1 discusses the importance of solid/gas and solid/liquid interfaces with relevance to gas-phase catalysis and electrochemistry, and the difficulties to characterize these interfaces *in situ*. Chapter 2 discusses the basic principles of x-ray core-level spectroscopies, particularly XPS and XAS, and the approaches to implement these two spectroscopic techniques for *in situ* and *operando* characterization of solid/gas and solid/liquid interfaces. Chapter 3 presents two case studies on solid/gas interfaces by AP-XPS, including cobalt catalyst for Fischer-Tropsch synthesis and palladium-cobalt alloy nanoparticles for CO oxidation reaction. Chapter 4 discusses *in situ* and *operando* XAS characterization of gold/water interface and noble metal/sulfuric acid solution interface. Chapter 5 summarizes the dissertation

and discusses the potential optimization as well as future directions of *in situ* and *operando* investigation of solid/gas and solid/liquid interfaces.

1.4 References

1   G. A. Somorjai and Y. Li, *Introduction to Surface Chemistry and Catalysis*, John Wiley & Sons, Inc.: Hoboken, NJ, 2010, 2nd ed., 1997.

2   G. Ertl, H. Knözinger, F. Schüth and J. Weitkamp, *Handbook of Heterogeneous Catalysis*, VCH-Wiley, Weinheim, Germany, 2008.

3   H. Ostrom, H. Oberg, H. Xin, J. LaRue, M. Beye, M. Dell'Angela, J. Gladh, M. L. Ng, J. A. Sellberg, S. Kaya, G. Mercurio, D. Nordlund, M. Hantschmann, F. Hieke, D. Kuhn, W. F. Schlotter, G. L. Dakovski, J. J. Turner, M. P. Minitti, A. Mitra, S. P. Moeller, A. Fohlisch, M. Wolf, W. Wurth, M. Persson, J. K. Norskov, F. Abild-Pedersen, H. Ogasawara, L. G. M. Pettersson and A. Nilsson, *Science*, 2015, **347**, 978–983.

4   G. Chen, Y. Zhao, G. Fu, P. N. Duchesne, L. Gu, Y. Zheng, X. Weng, M. Chen, P. Zhang, C.-W. Pao, J.-F. Lee and N. Zheng, *Science.*, 2014, **344**, 495–499.

5   S. Royer and D. Duprez, *ChemCatChem*, 2011, **3**, 24–65.

6   J. W. Niemantsverdriet, *Spectroscopy in Catalysis - An Introduction*, Wiley-VCH Verlag GmbH & Co. KGaA, 3rd edn.

7   M. Salmeron and R. Schlogl, *Surf. Sci. Rep.*, 2008, **63**, 169–199.

8   C. Escudero and M. Salmeron, *Surf. Sci.*, 2013, **607**, 2–9.

9   B. L. M. Hendriksen, S. C. Bobaru and J. W. M. Frenken, *Surf. Sci.*, 2004, **552**, 229–242.

10   D. R. Butcher, Z. Zhu, B. Mao, H. Wang, Z. Liu, M. Salmeron and G. A. Somorjai, *Chem. Commun.*, 2013, **49**, 6903–5.

11   A. J. Bard and L. R. Faulkner, *Electrochemical Methods: Fundamentals and Applications*, Wiley, 1980.

12   K. E. R. England, *Mineral. Mag.*, 1999, **63**, 559–566.

13   M. V. Lebedev, W. Calvet, T. Mayer and W. Jaegermann, *J. Phys. Chem. C*, 2014, **118**, 12774–12781.

14   R. Qiao, I. T. Lucas, A. Karim, J. Syzdek, X. Liu, W. Chen, K. Persson, R. Kostecki and W. Yang, *Adv. Mater. Interfaces*, 2014, **1**, 1300115.

15   C. Stuhlmann, Z. Park, C. Bach and K. Wandelt, *Electrochim. Acta*, 1998, **44**, 993–998.

16   F. T. Wagner and P. N. Ross, *Surf. Sci. Lett.*, 1985, **160**, A500–A501.

17   F. Lin, I. M. Markus, D. Nordlund, T.-C. Weng, M. D. Asta, H. L. Xin and M. M. Doeff, *Nat. Commun.*, 2014, **5**, 3529.

18   Y. Li, F. El Gabaly, T. R. Ferguson, R. B. Smith, N. C. Bartelt, J. D. Sugar, K. R. Fenton, D. A. Cogswell, A. L. D. Kilcoyne, T. Tyliszczak, M. Z. Bazant and W. C. Chueh, *Nat. Mater.*, 2014, **13**, 1149–1156.

19   M. Fleischmann and B. W. Mao, *J. Electroanal. Chem. Interfacial Electrochem.*, 1987, **229**, 125–139.

20   A. M. Donald, *Nat. Mater.*, 2003, **2**, 511–516.

21   H. Zheng, Y. S. Meng and Y. Zhu, *MRS Bull.*, 2015, **40**, 12–18.

22   H. L. Xin, S. Alayoglu, R. Tao, A. Genc, C.-M. Wang, L. Kovarik, E. a Stach, L.-W. Wang, M. Salmeron, G. A. Somorjai and H. Zheng, *Nano Lett.*, 2014, **14**, 3203–7.

23   P. Chen, K. Y. Kung, Y. R. Shen and G. A. Somorjai, *Surf. Sci.*, 2001, **494**, 289–297.

24   P. Chen, S. Westerberg, K. Y. Kung, J. Zhu, J. Grunes and G. A. Somorjai, *Appl. Catal. A Gen.*, 2002, **229**, 147–154.

25   Y. R. Shen and V. Ostroverkhov, *Chem. Rev.*, 2006, **106**, 1140–54.

26   F. Tao, D. Tang, M. Salmeron and G. A. Somorjai, *Rev. Sci. Instrum.*, 2008, **79**, 084101.

27   D. F. Ogletree, H. Bluhm, G. Lebedev, C. S. Fadley, Z. Hussain and M. Salmeron, *Rev. Sci. Instrum.*, 2002, **73**, 3872.

28   L. L. Patera, C. Africh, R. S. Weatherup, R. Blume, S. Bhardwaj, C. Castellarin-Cudia, A. Knop-Gericke, R. Schloegl, G. Comelli, S. Hofmann and C. Cepek, *ACS Nano*, 2013, **7**, 7901–7912.

29   M. A. van Spronsen, G. J. C. van Baarle, C. T. Herbschleb, J. W. M. Frenken and I. M. N. Groot, *Catal. Today*, 2015, **244**, 85–95.

30   H. Noguchi, T. Okada and K. Uosaki, *Electrochim. Acta*, 2008, **53**, 6841–6844.

31   D. Verreault, V. Kurz, C. Howell and P. Koelsch, *Rev. Sci. Instrum.*, 2010, **81**, 063111.

32   Z. D. Schultz, S. K. Shaw and A. A. Gewirth, *J. Am. Chem. Soc.*, 2005, **127**, 15916–22.

33   M. J. Iedema, M. J. Dresser, D. L. Doering, J. B. Rowland, W. P. Hess, A. A. Tsekouras and J. P. Cowin, *J. Phys. Chem. B*, 1998, **102**, 9203–9214.

34   M. Osawa and M. Tsushima, *J. Phys. Chem. C*, 2008, **112**, 4248–4256.

35   Z.-Q. Tian and B. Ren, *Annu. Rev. Phys. Chem.*, 2004, **55**, 197–229.

36   M. Fleischmann, A. Oliver and J. Robinson, *Electrochim. Acta*, 1985, **31**, 899–906.

37   T. Kondo, J. Morita, K. Hanaoka, S. Takakusagi, K. Tamura, M. Takahasi, J. Mizuki and K. Uosaki, *J. Phys. Chem. C*, 2007, **111**, 13197–13204.

38   G. G. Long, J. Kruger, D. R. Black and M. Kuriyama, *J. Electrochem. Soc.*, 1983, **130**, 240.

39   A. J. Davenport, *J. Electrochem. Soc.*, 1991, **138**, 337.

40 L. J. Oblonsky, *J. Electrochem. Soc.*, 1998, **145**, 1922.

41 G. S. Frankel, A. J. Davenport, H. S. Isaacs, A. G. Schrott, C. V Jahnes and M. A. Russak, *J. Electrochem. Soc.*, 1992, 139, 1812.

42 J. M. Yuk, J. Park, P. Ercius, K. Kim, D. J. Hellebusch, M. F. Crommie, J. Y. Lee, A. Zettl and A. P. Alivisatos, *Science*, 2012, 336, 61–64.

43 Q. Chen, J. M. Smith, J. Park, K. Kim, D. Ho, H. I. Rasool, A. Zettl and A. P. Alivisatos, *Nano Lett.*, 2013, **13**, 4556–4561.

44 J. Park, H. Elmlund, P. Ercius, J. M. Yuk, D. T. Limmer, Q. Chen, K. Kim, S. H. Han, D. A. Weitz, A. Zettl and A. P. Alivisatos, *Science*, 2015, **349**, 290–295.

45 P. Broekmann, M. Wilms, M. Kruft, C. Stuhlmann and K. Wandelt, *J. Electroanal. Chem.*, 1999, **467**, 307–324.

46 M. Wilms, P. Broekmann, M. Kruft, Z. Park, C. Stuhlmann and K. Wandelt, *Surf. Sci.*, 1998, **402-404**, 83–86.

47 H. Yee and H. Abruna, *J. Phys. Chem.*, 1993, **97**, 6278–6288.

48 A. M. Funtikov, U. Linke, U. Stimming and R. Vogel, *Surf. Sci.*, 1995, **324**, L343–L348.

49 B. Braunschweig and W. Daum, *Langmuir*, 2009, **25**, 11112–11120.

50 K. Ataka, T. Yotsuyanagi and M. Osawa, *J. Phys. Chem.*, 1996, **100**, 10664–10672.

51 H. Zheng, R. K. Smith, Y.-W. Jun, C. Kisielowski, U. Dahmen and A. P. Alivisatos, *Science*, 2009, **324**, 1309–1312.

52 H.-G. Liao, L. Cui, S. Whitelam and H. Zheng, *Science*, 2012, **336**, 1011–1014.

53 H.-G. Liao, D. Zherebetskyy, H. Xin, C. Czarnik, P. Ercius, H. Elmlund, M. Pan, L.-W. Wang and H. Zheng, *Science*, 2014, **345**, 916–919.

54 Z. Zeng, W. Liang, H. Liao, H. L. Xin, Y. Chu and H. Zheng, *Nano Lett.*, 2014, **14**, 1745–1750.

Chapter 2

X-ray Core-Level Spectroscopies and *In Situ* Apparatus

Abstract

This chapter describes the basic principles of x-ray core-level spectroscopy, in particular x-ray photoelectron spectroscopy (XPS) and x-ray absorption spectroscopy (XAS). The designs of *in situ* and *operando* apparatus based on XPS and XAS are also described and illustrated with detailed diagrams.

2.1 X-ray Core-Level Spectroscopies

X-ray is a useful probe to selectively access the core level information of the target atoms. An x-ray photon with sufficient energy can excite a core-level electron to an unoccupied state at higher energy level or even into the continuum vacuum level, as shown in Figure 2-1a. Following the excitation event, the relaxation of the short-lived core-hole states can result in emission of electrons and photons through various mechanisms, some of which are illustrated in Figure 2-1b. Measuring the absorption event itself or the characteristics of the emitted electrons and photons provides rich information regarding the chemical states and chemical environment of the probed atoms. Depending on which step within the entire excitation-relaxation process is being detected, x-ray core-level spectroscopies can be divided into several basic categories:

- X-ray photoelectron spectroscopy (XPS)
- X-ray absorption spectroscopy (XAS)
- X-ray emission spectroscopy (XES)
- Resonant inelastic x-ray scattering (RIXS)
- Other core-level spectroscopies, such as x-ray Raman scattering (XRS)

X-ray photoelectron spectroscopy (XPS) measures the kinetic energy distribution of the photoelectrons ejected out of the sample surface with an electron analyzer, which can be used to extract binding energies of core levels from which photoelectrons are excited. In x-ray absorption spectroscopy (XAS), core-level electrons are excited to the unoccupied states with tunable x-ray energies across the absorption edge and x-ray absorbance is recorded as a function of x-ray energy; therefore, XAS spectra carry information regarding the unoccupied states of the materials. X-ray emission spectroscopy (XES) measures the energy profile of the emitted photons from the radiative recombination process of an x-ray-excited core-hole and an electron that occupies a higher energy level, which provides information about the occupied states. Resonant inelastic x-ray scattering (RIXS) is a resonant photon-in/photon-out technique where the incident x-ray wavelength coincides with, and hence resonates with one of the absorption edges. Such resonance greatly enhances the cross-sections of inelastic scattering processes, and provides information about both occupied and unoccupied states in a convolved manner. X-ray Raman spectroscopy (XRS) is analogous to the Raman scattering with visible light excitation. The XRS process is in principle similar to the XAS process, but it is not the absorption of x-ray photons that excites the core-level electrons, but the energy transfer from high-energy x-ray photons instead.
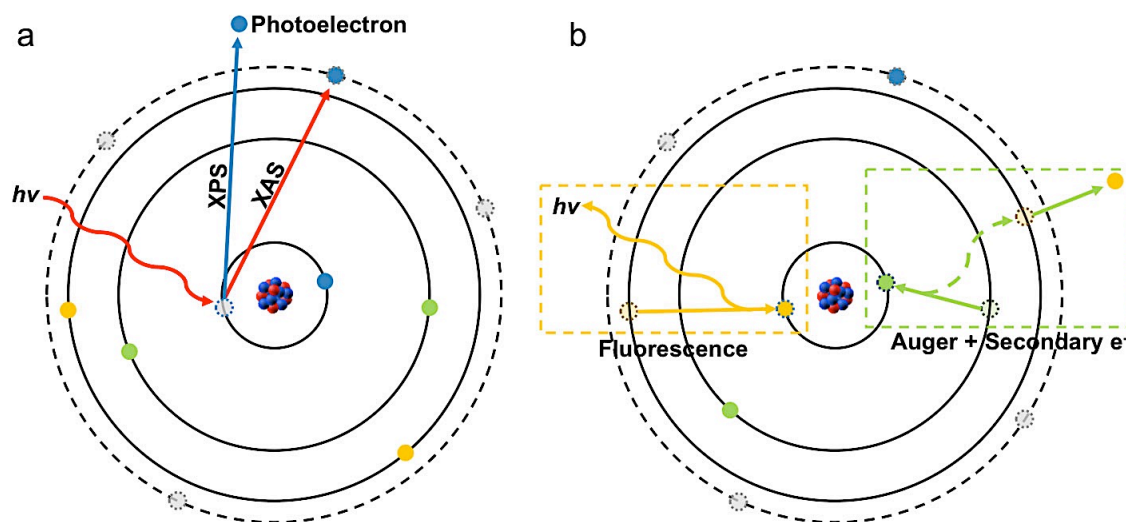
Figure 2-1. Schematic diagrams that illustrate: (a) the excitation processes of a core-level electron by an x-ray photon; (b) two relaxation pathways of the excited core-hole states, i.e. the fluorescence and Auger + secondary electron pathways.

In all of these x-ray core-level spectroscopies, core-level electrons are excited to higher energy states. The energies of these transitions are characteristic of different elements. Therefore, all these x-ray core-level spectroscopies are element-specific. Moreover, the electrons in valence level, which shield core-level electrons, or even directly participate in the transition-relaxation processes, are sensitive to the local geometry and chemical bonding of the excited atoms. Therefore, all these x-ray core-level spectroscopies can provide information regarding the chemical environment of the probed elements.

XPS and XAS are the main techniques used in the studies presented in this dissertation, which will be introduced in more detail in the following sections.

2.1.1 Basic Principles of X-ray Photoelectron Spectroscopy

X-ray photoelectron spectroscopy is based on the photoelectric effect that electrons are emitted from materials after absorbing photons with high enough energy.[1] The distribution of the kinetic energy of the ejected photoelectrons is what is actually being measured in XPS by an electron analyzer. When the intensity of photoelectrons is plotted against their kinetic energies, a serious of peaks can be identified. Each of peaks corresponds to one transition process from one particular core level or valence level to vacuum, as illustrated in Figure 2-1a. According the energy diagram of XPS measurement (Figure 2-2), the corresponding binding energy of electrons in the core levels or valence levels can be calculated by

$$E_B = h\nu - E_k - \Phi_S - (\Phi_A - \Phi_S) = h\nu - E_k - \Phi_A,$$

where $h\nu$ is the incident photon energy, E_k is the kinetic energy of ejected photoelectrons, Φ_S and Φ_A are the work functions of the sample and the analyzer, respectively. Electrons at the Fermi level in the sample are set to have zero binding energy. A typical XPS spectrum is a plot of photoelectron intensity versus binding energy.
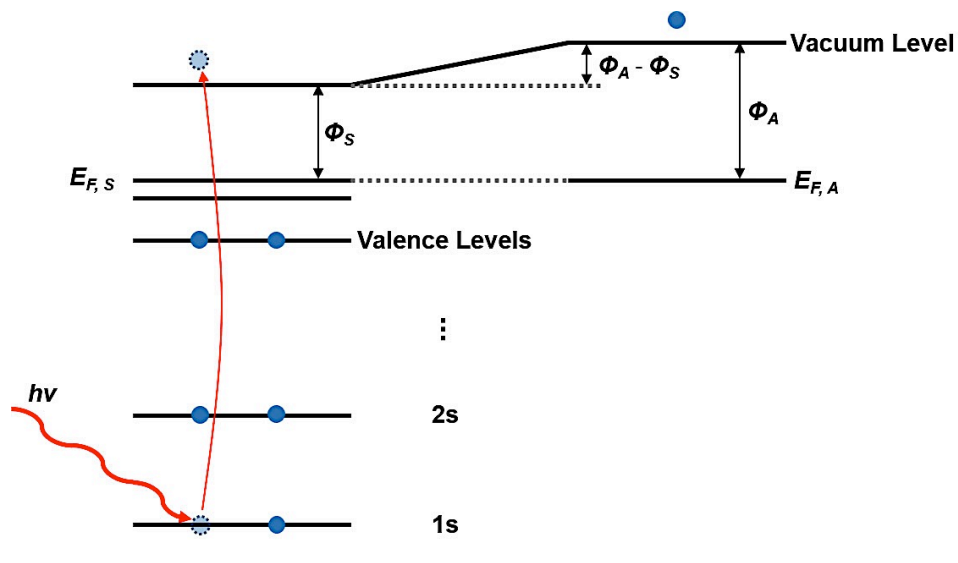

Figure 2-2. The energy diagram of XPS measurement.

The most commonly used lab x-ray sources are generated from the *Kα* emission lines of Mg (1253.6 eV) and Al (1486.3 eV). Synchrotron x-ray sources, particularly soft x-rays, are also used for various XPS measurement. According to the electron mean free path (MFP) universal curve, in solid materials, the MFP of electrons with kinetic energy below 1500eV is typically below 2nm.[2,3] Therefore the probing depth of the photoelectrons excited by these common x-ray sources is typically less than 2nm, which makes XPS a surface-sensitive technique. Because the binding energies of core level electrons are characteristic of each element, XPS peaks can be used to identify different elements contained in the surface layer of the sample. Besides element identification, the atomic fraction of each constituent element, as well as the relative concentration of different chemical states of the same element, can also be quantitatively determined by XPS, via peak integration and proper deconvolution. Since each atomic level has its own possibility to interact with photons, relative sensitivity factors, also known as photoemission cross-sections, must be taken into consideration for quantification.

2.1.2 Basic Principles of X-ray Absorption Spectroscopy

When a beam of monochromatic x-rays passes through matter, the intensity of the x-ray

beam drops because of the strong interaction between x-ray photons and atoms in the materials. Similarly as the ultraviolet-visible (UV-vis) absorption, the intensity drops exponentially with distance. If the material is homogeneous, the intensity after transmission is:

$$I = I_0 e^{-\rho\mu(E)t} ,$$

where I and I_0 are the transmitted and the incident x-ray intensities, respectively; ρ is the mass density of the material; $\mu(E)$ is the absorption coefficient as a function of incident x-ray photon energy E; t is the thickness of the sample or penetration depth of the light beam. In the energy range of x-rays, i.e., hundreds to tens of thousands electron volts, absorption coefficients decrease smoothly with increasing photon energy, except for certain photon energies, where the coefficients increase abruptly. These sharp features are known as absorption edges, where the incident photons have just enough energy to promote a core-level electron to an unoccupied valence level or into the continuum. The transition probability of such process is largest when the photon energy matches the energy difference between the initial and final states in the transition process, which gives rise to the abrupt increase in absorption coefficient. After each absorption edge, the absorption coefficient will continue to decrease with increasing photon energy.

The absorption edge together with the neighboring region is what XAS measurements focus on.[4] Because the electrons excited by x-ray photons come from core levels, the energy required for such excitation is characteristic of probed atoms, which provides the element specificity in XAS measurements. Meanwhile, because the absorption events also involve valence-level states, such as the lowest unoccupied molecular orbital (LUMO) of a molecule or the conduction band of a solid, the detailed shape of the absorption edge depend on the electronic structure of the unoccupied valence levels, which is why x-ray absorption spectra are sensitive to chemical environment of the probed atoms.

Figure 2-3 shows an example of Pt L_3-edge x-ray absorption spectrum. The spectral features close to the absorption edge, typically from the pre-edge region to about 50 - 100 eV above the edge, are sometimes referred to as near-edge x-ray absorption fine structure (NEXAFS). When the core-level electrons are excited by x-ray photons with higher photon energies than the absorption edge, for example, 100 eV and more above the absorption edge, the excited electrons can leave the probed atom and will be weakly backscattered by neighboring atoms. This extended part of an XAS spectrum usually has a sinusoidal shape, the frequency of which is a function of interatomic distances, the number of neighbors, and the type of coordinating atoms. This part of spectrum is called extended x-ray absorption fine structures (EXAFS). In order to reliably extract information from EXAFS spectra, one needs to scan the region up to several hundred
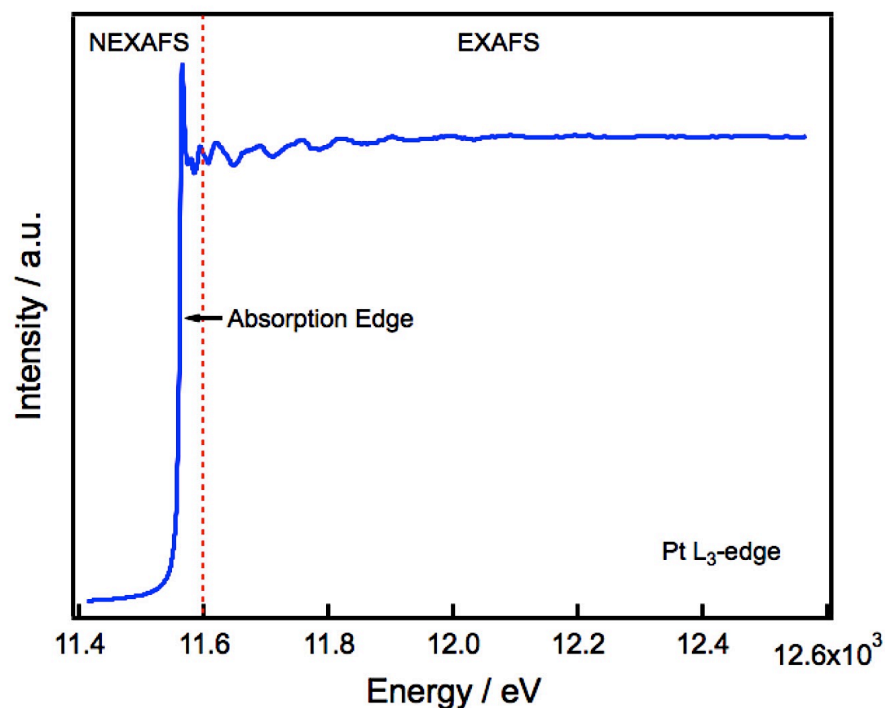
Figure 2-3. An example of Pt L_3-edge XAS spectrum including both near-edge (NEXAFS) and extended (EXAFS) region, measured at Beamline 10.3.2.

electron volts above the absorption edge. Therefore, EXAFS spectra can only be measured in the hard x-ray region, as in the soft x-ray region (100 - 1000 eV), the absorption edges of different elements are very close to each other.

In this dissertation, all the XAS results were measured within the soft x-ray region, and only NEXAFS spectra were analyzed.

2.1.3 Different Detection Modes of X-ray Absorption Spectroscopy

UV-vis absorption measurement is typically performed in transmission geometry, where the light source and the detector locate on two opposite sides of the sample. The detector measures the intensity of light I that passes through the sample, which can be used to extract the absorption coefficient according to the relationship below:

$$I = I_0 e^{-\rho\mu(E)t}$$

In the soft x-ray region, the absorption coefficient of most materials is so large that the intensity of the x-rays will drop to zero within very small distance, typically on the orders of micrometers or hundreds of nanometers. In order to measure XAS in the transmission mode, the thickness of the sample has to be kept extremely small, which very much limits the types of samples that can be measured. One type of sample that has been measured by XAS in the transmission mode is liquid thin film sandwiched between two x-ray-

17

transparent membranes, for example, water films sandwiched between two ultra-thin Si_3N_4 membranes.[5]

For regular samples, XAS measurement in transmission mode is obviously not feasible. Alternatively, the electrons or photons emitted after the relaxation of the core-holes, as shown in Figure 2-1b, can be detected. Naturally, the intensity of these secondary signals (I_p or I_e) should be proportional to the intensity of the absorbed x-rays:

$$I_p \text{ or } I_e \sim I_0 - I = I_0(1 - e^{-\rho\mu(E)t}).$$

If the exponential term $\rho\mu(E)t$ is small enough, i.e., $\rho\mu(E)t \ll 1$, we can use Taylor expansion to approximate the exponential term and ignore the second and higher order terms:

$$e^{-x} = 1 - x + o(x^2) \approx 1 - x.$$

Now the relationship between I_p or I_e and $\mu(E)$ can be approximated as:

$$I_p \text{ or } I_e \sim I_0 - I = I_0(1 - e^{-\rho\mu(E)t}) \approx I_0\rho\mu(E)t \propto \mu(E)$$

For fluorescent photons, the Taylor expansion can be problematic because the MFP of soft x-ray photons is typically hundreds of nanometers. When the condition $\rho\mu(E)t \ll 1$ is not satisfied, the non-diminishing higher order terms can substantially alter the linearity between fluorescence yield (FY) signal and $\mu(E)$. Moreover, secondary absorption of the emitted photons in the materials can also contribute to the distortion of the FY spectra. Nonetheless, FY spectra still provide useful qualitative information of the bulk materials, because of the large probing depth of fluorescence photons.

For photoelectrons, Auger electrons, and most secondary electrons, their MFPs in condensed matters are very small, typically several nanometers,[2,6–8] so that only the electrons generated very close to the surface can be ejected and detected. As a result, for electrode yield (EY) signals, either Auger electron yield (AEY), partial electron yield (PEY), or total electron yield (TEY), the sampling depth t, is extremely small; hence the linear correlation between EY signals and $\mu(E)$ is valid in most cases. It is noteworthy that AEY or PEY signal is usually measured by an electron analyzer, such as the one used in XPS, whereas TEY signal is usually measured as a current between the sample and the ground. Because electron analyzers can selectively collect electrons with specific kinetic energies or within certain energy ranges, the probing depth of AEY or PEY is relatively well defined. In TEY detection mode, the electrons with different kinetic energies cannot be distinguished in a simple current measurement. Since the electrons with different kinetic energies have different MFPs in condensed matters, therefore the probing depth of TEY signal is not as well-defined as AEY or PEY. Nonetheless, within the soft x-ray energy range (100-1000 eV), the MFPs of electrons are all below 2nm and

thus the assumption in the Taylor expansion, $\rho\mu(E)t <<1$, is still valid in most cases.

2.1.4 Synchrotron Radiation

When charged particles, such as electrons, are accelerated in a storage ring or a synchrotron, electromagnetic radiation including x-rays can be produced. With the development of high-brilliance synchrotron facilities all around the world, more and more x-ray-based characterization techniques are being developed, optimized, and utilized in many different areas of scientific research.

XAS measurement requires tunable x-ray source, therefore it is only feasible at synchrotron facilities. Although XPS measurement can be done with lab x-ray sources, using synchrotron x-ray source for XPS measurement is beneficial in multiple ways. First of all, synchrotron x-ray source is much brighter than regular lab source, which can substantially improve the signal intensity and reduce the data acquisition time. Secondly, with tunable x-ray source, it is possible to selectively choose the excitation photon energy to achieve optimum surface sensitivity for each element. Last but not least, with tunable x-ray source, PEY or AEY XAS measurement can be realized using the electron analyzer inside the XPS chamber.

All the experiments presented in this dissertation were performed at the Advanced Light Source (ALS), a third-generation synchrotron facility operated by Lawrence Berkeley National Laboratory, which specializes in soft x-rays. The *in situ* XPS experiments were performed at two ambient-pressure XPS (AP-XPS) stations at Beamline 9.3.2 and
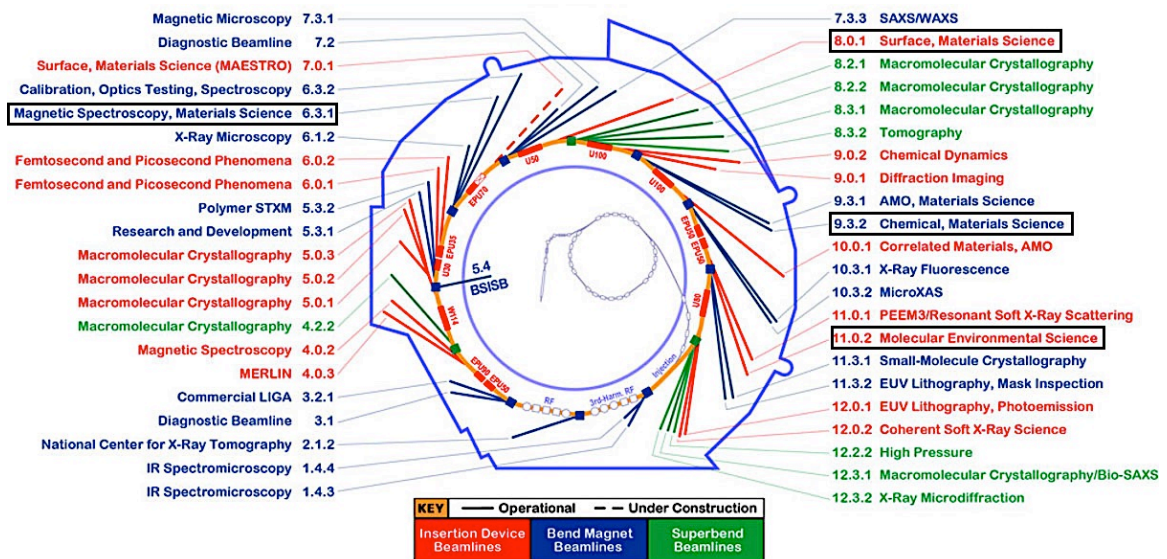

Figure 2-4. ALS Beamlines, highlighting the four beamlines involved in the studies presented in this dissertation. Modified from ALS website: www-als.lbl.gov.

Beamline 11.0.2, respectively. The *in situ* XAS experiments were performed at the wet-RIXS station at the Beamline 8.0.1 and the ISAAC station at Beamline 6.3.1.

It is worth mentioning that, despite all the benefits, high brilliance x-ray source may cause undesired beam-induced effects, such as degradation of organic materials,[9] decomposition of metal complexes,[10] oxidation of metals,[11] and the like. At two of the undulator beamlines, Beamline 8.0.1 and 11.0.2, such beam-induced effects have been indeed observed in some experimental systems. Therefore, special care needs to be taken at these beam lines to minimize, if not eliminate, such beam-induced effects. The precautions include defocusing the x-ray beam, frequently moving the beam spot on the sample, or even compromising the photon flux if necessary.

2.1.5 Limitations of Traditional X-ray Photoelectron and Absorption Spectroscopy

With the development of synchrotron facilities providing high-brilliance x-rays, x-ray core-level spectroscopies, such as XPS and XAS, have been extensively utilized in materials science research. As hard x-rays, whose photon energy is typically thousands or even tens of thousands electron volts, don't require ultra-high vacuum (UHV) chambers due to their penetration ability, *in situ* hard x-ray techniques are far more straightforward to implement compared to *in situ* soft x-ray techniques. Therefore, most attempts so far to use x-ray spectroscopies to characterize ambient-condition interface systems *in situ* have involved hard x-ray NEXAFS and EXAFS with grazing-angle incidence or reflection geometry.[12–14]

However, hard x-rays are typically used to access the core levels of relatively heavy elements, with exceptions of x-ray Raman scattering and the like, most of which have extremely small scattering cross-sections. But most of the gas molecules involved in gas-phase catalysis, as well as the solvent molecules and solute species in electrochemical systems, contain exclusively light elements, such as carbon, nitrogen, oxygen, and lithium. To access the core levels of these elements, soft x-rays with typical energies of 50 - 1000 eV are necessary. But the requirement of vacuum for soft x-ray propagation and photoelectron detection has been a long-standing obstacle for the application of soft x-ray techniques under ambient conditions.

2.2 Ambient-Pressure X-ray Photoelectron Spectroscopy

2.2.1 The Development of Ambient-Pressure X-ray Photoelectron Spectroscopy

In XPS measurement, both incident x-ray and ejected photoelectrons can interact with

gas molecules. As a result, the introduction of ambient-pressure gases will substantially reduce the signal intensity. This is one of the main reasons why the conventional XPS chambers and electron analyzers are kept under UHV conditions. Nonetheless, the interaction between x-ray photons and gas molecules is much weaker than that between photoelectrons and gas molecules. For instance, when a soft x-ray beam with energy around the O$1s$ absorption edge (~535 eV) pass through a 1cm layer of room temperature 30 Torr O_2 gas, the transmission is more than 30% (estimated by the CXRO online simulation tool, http://henke.lbl.gov/optical_constants/gastrn2.html). Therefore, the transmission of x-ray beam under ambient-pressure gases is not a limiting factor for *in situ* XPS measurements. The interaction between photoelectrons and gas molecules, on the other hand, is much stronger than the photon-gas interaction and thus brings more serious issues for *in situ* measurement. In order to implement *in situ* XPS characterization, one would need a strategy to greatly reduce the electron-gas interaction on the trajectory of photoelectrons, from the sample surface all the way into the analyzer.

The history of ambient-pressure XPS dates back to the beginning of the method.[15] One successful strategy is the differential pumping system between analysis chamber filled with ambient-pressure gases and the electron analyzer kept in UHV.[16–18] On their
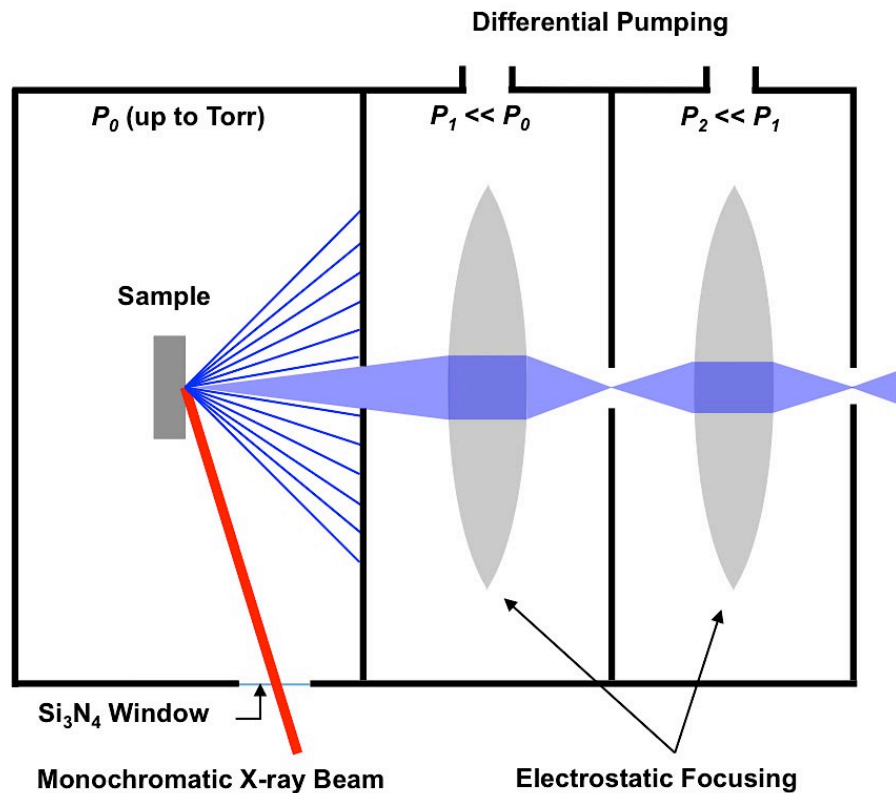

Figure 2-5. The conceptual design of ambient-pressure XPS first developed in 2002.

trajectory to the electron analyzer, the photoelectrons emitted from the sample surface pass through one or more pumping stages through small apertures, as illustrated in Figure 2-5. The pressure in each pumping stage is much smaller than the previous one, which greatly reduces the signal attenuation by gas scattering. The XPS instrument with differential pumping system was capable to operate at pressure up to 1 mbar.[16,17] In 2002, a new design was developed at the ALS, where an electrostatic lens system was used to focus the photoelectrons emitted through an aperture,[18] as illustrated in Figure 2-5. The electrostatic lens system substantially increases the fraction of collectable photoelectrons that would otherwise be lost because of the small solid angle captured by the apertures separating the pumping stages as well as the diverging nature of photoelectron trajectories. Since then, newer generations of AP-XPS instrument based on the original design in 2002 have been developed and constructed or under construction at many other synchrotron facilities around the world,[19–22] which led to rapidly growing efforts in *in situ* and *operando* characterization of various solid/gas or liquid/gas interfaces under ambient-pressure conditions.

2.2.2 The AP-XPS Endstations at the Advanced Light Source

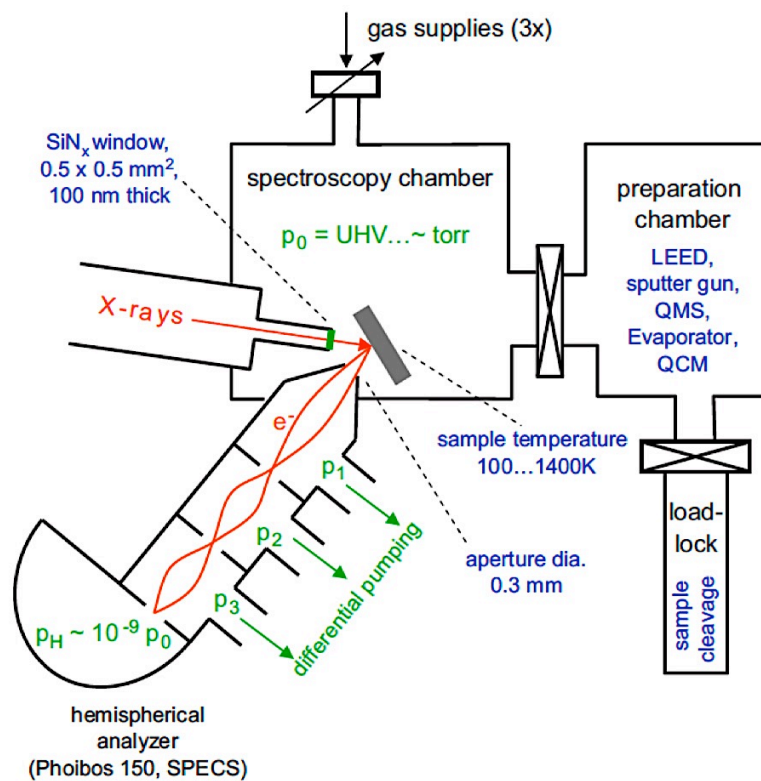The AP-XPS system at Beamline 11.0.2 at the ALS was designed with two chambers

Figure 2-6. Schematic design of the AP-XPS endstation at Beamline 11.0.2.[23]

separated by a gate valve, one for sample cleaning and preparation and the other for ambient-pressure measurements,[23] as illustrated in Figure 2-6. The base pressure of the preparation chamber is routinely kept in the 10^{-10} Torr range. A load-lock connected to the preparation chamber allows easy introduction of samples without significant perturbation to the base pressure. The preparation chamber is equipped with surface science instruments, such as ion sputtering, sample heating, and low energy electron diffraction (LEED), which is necessary to prepare clean single crystal samples.

After sample preparation, the sample can be transferred into the analysis chamber with a transfer rod. Multiple leak valves are connected to the analysis chamber, allowing the introduction of different gases up to total pressure of about 1 Torr. X-ray is delivered into the analysis chamber through a 100 nm thick Si_3N_4 window, preventing the gas molecules entering the x-ray source under UHV. A hemispherical analyzer is located at the end of the workstation and connected with the analysis chamber through an integrated differential pumping system. Photoelectrons enter the first pump stage through an exchangeable nozzle with a small aperture located very close to the sample surface and then travel through the entire differential pumping and electrostatic lens system towards the electron analyzer.

The sample is typically mounted on a ceramic button heater on the sample holder using tantalum or stainless steel clips, with thermocouple wires underneath to measure the surface temperature. The materials of the sample holder, clips, button heater, and thermocouple wires need to be carefully selected depending on the experiments, to avoid undesired catalytic reactions catalyzed by these components upon heating.

Since the analysis chamber is frequently exposed to different gases in different experiments, each time before our experiments, the analysis chamber (and sometimes the preparation chamber too) is carefully cleaned by a proper bake-out or ignition of nitrogen plasma or both. A clean chamber is crucial for meaningful AP-XPS measurements, as cross contamination from previous experiments can lead to detrimental consequences.

The design of AP-XPS endstation at Beamline 9.3.2[22] is very similar to Beamline 11.0.2. The main difference is the characteristics of the x-ray source. Beamline 11.0.2 is an undulator beamline, where the photon flux can reach 5×10^{12} photons/second under regular operation conditions. The x-ray energy range is 75 - 2000 eV, and thus the 2p orbitals of all 3d transition metals are accessible at this beamline. Beamline 9.3.2 is a bending magnet beamline, where the photon flux is much lower (up to 1.5×10^{11} photons/second). Moreover, the photon flux drops significantly beyond 800 eV, making it almost impossible to access the 2p orbitals of 3d transition metals beyond cobalt.

2.3 *In Situ* and *Operando* X-ray Absorption Spectroscopy

Because soft x-ray absorption spectroscopy typically operates in UHV environment, materials under ambient conditions cannot be directly characterized in regular XAS chambers. Over the past few years, many different strategies have been explored to resolve the compatibility issue between ambient-condition samples and the vacuum requirement. In particular, for liquid samples, high-speed liquid jet is one successful strategy, where ambient-condition liquid is ejected into the vacuum chamber at extremely high speed through a micrometer-diameter nozzle.[24–26] This strategy allows introduction of real ambient-condition liquid into a vacuum chamber, where XAS measurement can be carried out. Our strategy to introduce ambient-condition liquid into the XAS chamber under UHV conditions is using a specially designed liquid cell.[27–29]

2.3.1 The Liquid Cells for *In Situ* X-ray Absorption Measurements

Figure 2-7 illustrates the core part of the liquid cell. This type of liquid cell allows liquid to flow in and out during the measurement; therefore, it is referred to as flow liquid cell.

A 100 nm silicon nitride (Si_3N_4) membrane serves as an x-ray transparent window, which also separates the UHV environment in the chamber from the ambient environment inside the liquid cell. The Si_3N_4 membrane, typically 1mm × 1mm in area, is supported on 1cm × 1cm and 500μm-thick silicon frame. The entire piece is mounted on the open end of the small reaction chamber and seals the ambient-condition liquid underneath by O-rings or
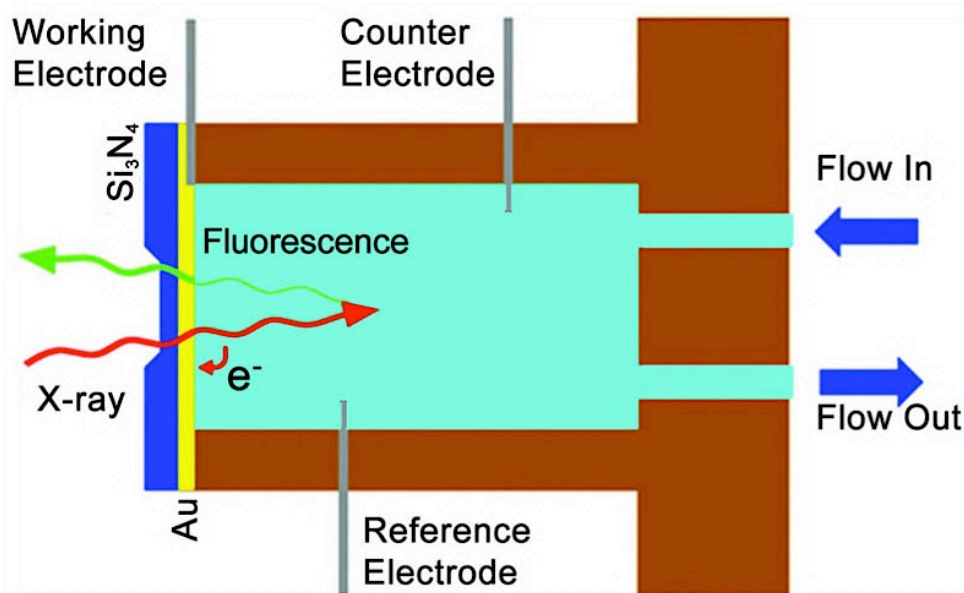

Figure 2-7. Schematic design of the flow liquid cell. From Reference [29]. Reprinted with permission from AAAS.

vacuum-compatible epoxy. The electrode materials of interest can be deposited on the flat side of the Si_3N_4 membrane, which function as both working electrode and secondary electron current collector. The thickness of the electrode is controlled to be very thin (typically less than 50 nm) to ensure sufficient transmission of incident x-rays. A copper wire is connected to one edge of the thin film electrode via silver paste, as electrical contact for the working electrode. A platinum wire and a silver wire are inserted into the reaction chamber as the counter electrode and the quasi-reference electrode, respectively. In a newer version of the flow cell,[28] the silver wire can be replaced by a miniature Ag/AgCl electrode as a standard reference electrode, although the miniature reference electrode is very fragile. The liquid inside the reaction chamber can be refreshed via two plastic tubes connected to the other end of the reaction chamber, allowing switching solutions during *in situ* experiments.

Most of the previous XAS studies involving the use of liquid cell mostly focused on the liquid itself[30–32] or the electrode materials.[27] For these bulk samples, the fluorescence signal, or total fluorescence yield (TFY) is more relevant, given that the MFP of fluorescence photons is on the order of hundred nanometers. On the other hand, the IMFP of electrons in water or other liquid are extremely small compared to x-ray photons, typically on the order of nanometers within the soft x-ray energy range,[6–8] as shown in Figure 2-8. Therefore, if the secondary electrons can be collected as a current through the electrode, it is possible to obtain interface-sensitive information. Whilst the short IMFP of secondary electrons in liquid ensures the interface sensitivity of these measurements,
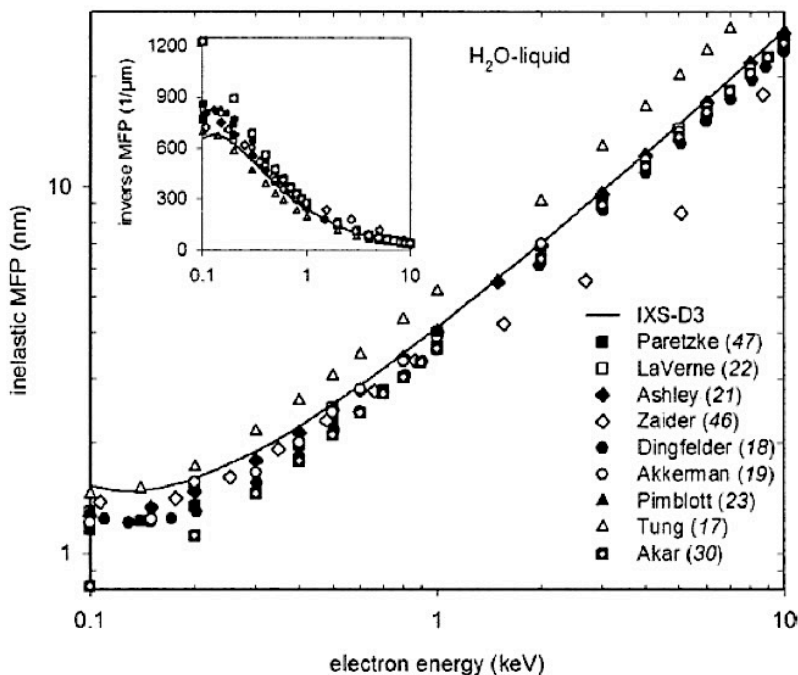

Figure 2-8. Calculated inelastic mean free path (IMFP) of electrons in liquid water.[8]

secondary electrons with different kinetic energies cannot be distinguished in a current measurement;[33] therefore, the spectra acquired in this mode are referred to as total electron yield (TEY) spectra.

Flow liquid cells require a special load-lock port attached to the XAS chamber. There is another type of liquid cells that is very similar in principle to the flow liquid cell but is much easier to operate. This type of cell adopts the similar dimensions as the regular sample holder at Beamline 8.0.1 or Beamline 6.3.1. Therefore, it can be transferred into the chamber through the regular load-lock, mounted onto the regular manipulator and measured very much like a regular sample. Figure 2-9 shows the design of such a liquid cell used at Beamline 8.0.1. The small amount of liquid, typically several hundred microliters, cannot be refreshed during one experiment; therefore, this type of cell is referred to as the static liquid cell.

(i) PEEK base
(ii) Si₃N₄ window
(iii) Working Electrode
(iv) Reference Electrode
(v) Counter Electrode
(vi) Oring
(vii) Liquid reservior

Electrochemical static liquid cell
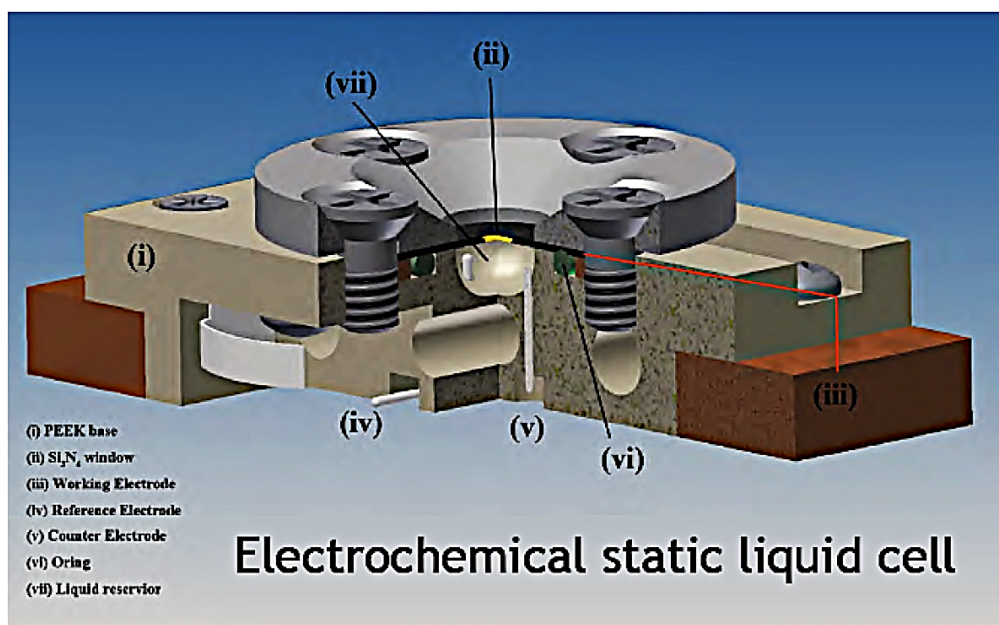
Figure 2-9. Schematic design of the static liquid cell used at Beamline 8.0.1.

Similar concept can also be used to construct a gas cell to investigate materials under ambient condition gases.[34] Integrated with a heating system and a gas distribution/mixing system, such gas cell apparatus enables the XAS characterization of solid/gas interfaces *in situ* and *operando*, as demonstrated by Tuxen et al.[35] Compared to AP-XPS, such gas cell apparatus can push the pressure limit of *in situ* characterization even further, up to 1-3 bar, depending on the mechanical strength of the Si_3N_4 membrane.

2.3.2 X-ray Modulation and *Operando* X-ray Absorption Measurements

The most important motivation behind *in situ* characterization of solid/liquid interfaces is

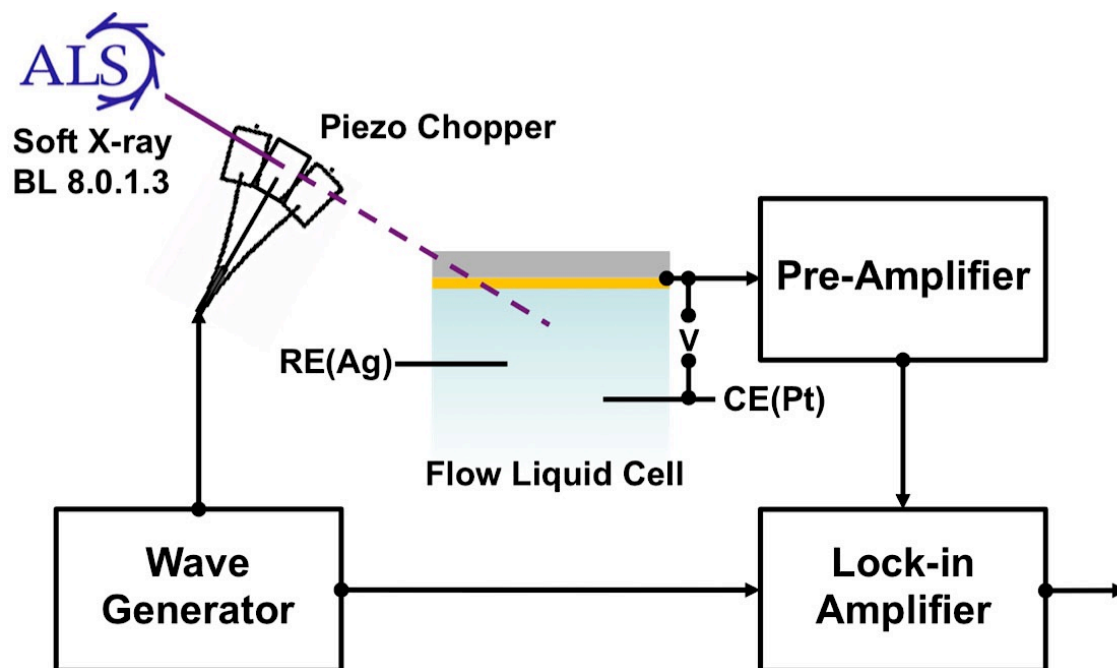**Figure 2-10.** Schematic design of *operando* XAS setup, including the liquid cell, x-ray chopper and other electronics.

electrochemistry. However, when electrochemical potentials are introduced to this *in situ* XAS system, the dominating ionic current (typically microamperes) severely hinders the collection of the tiny secondary electron current (typically nanoamperes).

One approach to separate the secondary electron current from the dominant DC current background is to make the electron yield signal an AC current, which can be extracted by lock-in amplifiers.[29] In order to make the secondary electron current alternating, a piezo-actuated chopper was installed in the x-ray tube located upstream of the XAS chamber. A function generator is used to generate a sinusoidal signal to drive the vibration of the chopper, which periodically blocks the incident x-ray. With such intermittent incident x-rays, the secondary electron current becomes an AC component and can be readily separated from the DC background. Combining the liquid cell and the x-ray modulation system, as schematically illustrated in Figure 2-10, it is possible to study solid/liquid interfaces *operando*.

2.4 References

1   S. Hüfner, *Photoelectron Spectroscopy - Principles and Applications*, Springer Berlin Heidelberg, Berlin, Heidelberg, 2003.

2   G. A. Somorjai and Y. Li, *Introduction to Surface Chemistry and Catalysis*, John Wiley & Sons, Inc.: Hoboken, NJ, 2010, 2nd ed., 1997.

3   C. J. Powell and A. Jablonski, *NIST Electron Inelastic Mean Free Path Database, version 1.1*, National Institute of Standards and Technology, Gaithersburg, MD, 2002.

4   J. Stöhr, *NEXAFS Spectroscopy*, Springer Berlin Heidelberg, Berlin, Heidelberg, 1992, vol. 25.

5   A. Nilsson, D. Nordlund, I. Waluyo, N. Huang, H. Ogasawara, S. Kaya, U. Bergmann, L.-Å. Näslund, H. Öström, P. Wernet, K. J. Andersson, T. Schiros and L. G. M. Pettersson, *J. Electron Spectros. Relat. Phenomena*, 2010, **177**, 99–129.

6   S. Thürmer, R. Seidel, M. Faubel, W. Eberhardt, J. C. Hemminger, S. E. Bradforth and B. Winter, *Phys. Rev. Lett.*, 2013, **111**, 173005.

7   B. Frazer, B. Gilbert, B. Sonderegger and G. De Stasio, *Surf. Sci.*, 2003, **537**, 161–167.

8   D. Emfietzoglou and H. Nikjoo, *Radiat. Res.*, 2007, **167**, 110–120.

9   K. Yoshihara and A. Tanaka, *Surf. Interface Anal.*, 2002, **33**, 252–258.

10   D. A. Cleary and D. R. Baer, *Chem. Mater.*, 1992, **4**, 112–116.

11   P. Jiang, S. Porsgaard, F. Borondics, M. Köber, A. Caballero, H. Bluhm, F. Besenbacher and M. Salmeron, *J. Am. Chem. Soc.*, 2010, **132**, 2858–9.

12   G. E. Brown, Jr. and G. Calas, *Geochemical Perspect.*, 2012, **1**, 483–742.

13   T. P. Trainor, J. P. Fitts, A. S. Templeton, D. Grolimund and G. E. Brown, *J. Colloid Interface Sci.*, 2001, **244**, 239–244.

14   J. R. Bargar, S. N. Towle, G. E. Brown and G. A. Parks, *Geochim. Cosmochim. Acta*, 1996, **60**, 3541–3547.

15   M. Salmeron and R. Schlogl, *Surf. Sci. Rep.*, 2008, **63**, 169–199.

16   R. W. Joyner, M. W. Roberts and K. Yates, *Surf. Sci.*, 1979, **87**, 501–509.

17   R. W. Joyner and M. W. Roberts, *Chem. Phys. Lett.*, 1979, **60**, 459–462.

18   D. F. Ogletree, H. Bluhm, G. Lebedev, C. S. Fadley, Z. Hussain and M. Salmeron, *Rev. Sci. Instrum.*, 2002, **73**, 3872.

19   V. Pérez-Dieste, L. Aballe, S. Ferrer, J. Nicolàs, C. Escudero, a Milán and E. Pellegrin, *J. Phys. Conf. Ser.*, 2013, **425**, 072023.

20   J. Schnadt, J. Knudsen, J. N. Andersen, H. Siegbahn, A. Pietzsch, F. Hennies, N. Johansson, N. Mårtensson, G. Öhrwall, S. Bahr, S. Mähl and O. Schaff, *J. Synchrotron Radiat.*, 2012, **19**, 701–704.

21   D. Frank Ogletree, H. Bluhm, E. D. Hebenstreit and M. Salmeron, *Nucl. Instruments Methods Phys. Res. Sect. A Accel. Spectrometers, Detect. Assoc. Equip.*, 2009, **601**, 151–160.

22   M. E. Grass, P. G. Karlsson, F. Aksoy, M. Lundqvist, B. Wannberg, B. S. Mun, Z. Hussain and Z. Liu, *Rev. Sci. Instrum.*, 2010, **81**, 053106.

23 H. Bluhm, K. Andersson, T. Araki, K. Benzerara, G. Brown, J. Dynes, S. Ghosal, M. Gilles, H. Hansen and J. Hemminger, *J. Electron Spectros. Relat. Phenomena*, 2006, **150**, 86–104.

24 K. R. Wilson, B. S. Rude, J. Smith, C. Cappa, D. T. Co, R. D. Schaller, M. Larsson, T. Catalano and R. J. Saykally, *Rev. Sci. Instrum.*, 2004, **75**, 725–736.

25 R. K. Lam, A. H. England, A. T. Sheardy, O. Shih, J. W. Smith, A. M. Rizzuto, D. Prendergast and R. J. Saykally, *Chem. Phys. Lett.*, 2014, **614**, 282–286.

26 J. W. Smith, R. K.-J. Lam, A. T. Sheardy, O. Shih, A. M. Rizzuto, O. Borodin, S. J. Harris, D. Prendergast and R. J. Saykally, *Phys. Chem. Chem. Phys.*, 2014, **16**, 23568–23575.

27 P. Jiang, J.-L. Chen, F. Borondics, P.-A. Glans, M. W. West, C.-L. Chang, M. Salmeron and J. Guo, *Electrochem. commun.*, 2010, **12**, 820–822.

28 D. K. Bora, P.-A. Glans, J. Pepper, Y.-S. Liu, C. Du, D. Wang and J.-H. Guo, *Rev. Sci. Instrum.*, 2014, **85**, 043106.

29 J. J. Velasco-Velez, C. H. Wu, T. A. Pascal, L. F. Wan, J. Guo, D. Prendergast and M. Salmeron, *Science*, 2014, **346**, 831–834.

30 J.-H. Guo, Y. Luo, A. Augustsson, J.-E. Rubensson, C. Såthe, H. Ågren, H. Siegbahn and J. Nordgren, *Phys. Rev. Lett.*, 2002, **89**, 137402.

31 J.-H. Guo, Y. Luo, A. Augustsson, S. Kashtanov, J.-E. Rubensson, D. K. Shuh, H. Ågren and J. Nordgren, *Phys. Rev. Lett.*, 2003, **91**, 157401.

32 L. Näslund, J. Lüning, Y. Ufuktepe, H. Ogasawara, P. Wernet, U. Bergmann, L. G. M. Pettersson and A. Nilsson, *J. Phys. Chem. B*, 2005, **109**, 13835–9.

33 B. Winter, *Nat. Chem.*, 2015, **7**, 192–194.

34 C. Escudero, P. Jiang, E. Pach, F. Borondics, M. W. West, A. Tuxen, M. Chintapalli, S. Carenco, J. Guo and M. Salmeron, *J. Synchrotron Radiat.*, 2013, **20**, 504–508.

35 A. Tuxen, S. Carenco, M. Chintapalli, C.-H. Chuang, C. Escudero, E. Pach, P. Jiang, F. Borondics, B. Beberwyck, A. P. Alivisatos, G. Thornton, W.-F. Pong, J. Guo, R. Perez, F. Besenbacher and M. Salmeron, *J. Am. Chem. Soc.*, 2013, **135**, 2273–8.

Chapter 3

Solid/Gas Interfaces Studied by Ambient-Pressure X-ray Photoelectron Spectroscopy

Abstract

This chapter presents two case studies on solid/gas interfaces by ambient-pressure x-ray photoelectron spectroscopy (AP-XPS). Both studies illustrate the capability of such *in situ* and *operando* characterization technique for investigating reaction mechanisms and other fundamental aspects of gas-phase catalysis. The first study concerns Co catalyst for Fischer-Tropsch (F-T) synthesis. It was found that CO adsorbs strongly on the Co surface; but small amount of sulfur contamination on the surface substantially weakens the CO adsorption and thus poisons the F-T reaction. Under reaction conditions, the Co surface remains metallic. The water molecules in the reaction products can potentially oxidize the Co surface and consequently hinder the catalytic reaction. When the temperature is high enough, H_2 is responsible for reducing Co to its metallic phase and keeping the catalyst active. The second study focuses on CO oxidation reaction catalyzed by Co_xPd_y alloy nanoparticles. Catalytic activity tests exhibited a clear dependence of activities on the nanoparticle compositions. AP-XPS results helped explain the origin of such dependence. It was found that Co segregates to the surface in the oxide form after the pretreatment processes. Small amount of Co coexisting with Pd on the surface can promote the CO oxidation reaction synergistically and the synergetic effect becomes more prominent with increasing Co content, up to 25%. However, when Co/Pd ratio is too high, after the cleaning processes, nanoparticle surfaces become fully covered by CoO_x layers, preventing CO molecules from binding with Pd and resulting in significant drop in catalytic activities.

3.1 Fischer-Tropsch Synthesis on Cobalt Foil Studied by AP-XPS

Fischer-Tropsch (F-T) process is a series of CO hydrogenation reactions that convert a gaseous mixture of CO and H_2 into long-chain hydrocarbons.[1] F-T process is a key component of gas-to-liquid (GTL) technology that produces synthetic lubricants and synthetic fuels (particularly low-sulfur diesel fuels). The gas mixture of CO and H_2, known as the syngas, is typically produced from natural gas and coal through a gasification process. Biomass is also considered as a viable syngas feedstock, which makes F-T synthesis more environmental friendly. Commonly used F-T catalysts include ruthenium, cobalt, iron, and nickel.[2]

Although F-T process was discovered almost a century ago and has been studied extensively since then, many fundamental questions regarding its reaction mechanism still remain open.[3] For example, does the surface structure of the catalyst changes under operating conditions? Does the surface of the catalysts stay metallic, or does it transform into some sort of oxides or even carbides? More fundamentally, in which steps in the reaction sequence does the C-O bond break? Is hydrogen necessary for CO decomposition? To answer all of these questions, one may need a series of *in situ* techniques to characterize the catalysts under operating conditions.

Cobalt, as an active F-T catalyst, has been studied by several *in situ* techniques. *In situ* x-ray diffraction (XRD)[4,5] and *in situ* x-ray absorption spectroscopy (XAS, mostly hard x-ray)[5–7] have shown the metallic nature of the catalyst under reaction conditions. But XRD cannot prove or disprove the existence of amorphous surface oxide layer. Deep penetration of hard x-rays in the XAS studies also poses the same concern. High-pressure STM results has suggested no obvious surface reconstructions on Co(0001) single crystal surfaces when syngas was introduced in the system.[3] However, the surfaces of the real catalysts are different from single crystal surfaces in many ways, such as much smaller size and thus higher stress, and a lot more under-coordinated edge and kink sites.

Metal foils are another type of model catalysts besides single crystals. Because of their polycrystalline nature, foils also have numerous edge sites, kink sites, defect sites, and grain boundaries, very much like the actual catalysts. On the other hand, unlike nanoparticles samples, foils can be cleaned thoroughly via traditional surface science cleaning procedures, which makes it possible to obtain clean surfaces, similarly as single crystal surfaces. Herein, we investigated a cobalt foil by AP-XPS, aiming to understand the fundamental aspects of Co catalysts under syngas. All the measurements were performed at the AP-XPS endstation at Beamline 11.0.2.

3.1.1 Cleaning Procedure of Cobalt Foil

Co is a very reactive metal, which makes it very difficult to clean. Moreover, the solubility of carbon in Co is relatively high, up to ~5% (atomic percentage) at 450°C.[8] As a result, surface carbon species may dissolve into the bulk Co upon heating and then precipitate to the surface during cooling as a result of super-saturation.

We have developed a recipe to thoroughly clean the Co foil inside the preparation chamber. The cleaning procedure involves the following steps:

(i). Pre-heat the foil in vacuum up to 400°C for initial degassing;

(ii). Repeated cycles of Ar^+ sputtering (4×10^{-5} Torr Ar, 1.5 kV, 5 mA) followed by thermal annealing up to 400°C;

(iii). Dose 1×10^{-7} Torr O_2 briefly (~10 seconds) at ~400°C;

(iv). Pump down O_2 and keep heating the foil in vacuum up to ~700°C;

(v). Repeat (iii) and (iv) if necessary and then cool down.

Step (iii) helps combusting the carbon on the surface, but the Co surface gets oxidized as well. Step (iv) is designed to decompose the Co oxide at high temperature. Repetition of steps (iii) and (iv) can potentially deplete the carbon impurities dissolved in the surface layer of Co foil. The effectiveness of these steps was verified by monitoring C*1s*, O*1s*, and Co*2p* XPS spectra *in situ* inside the analysis chamber.

Figure 3-1 shows a typical survey spectra measured on a clean Co surface during the final cooling process. Only very small oxygen and carbon peaks appear in the spectra. Co*2p* XPS spectrum (inset of Figure 3-1) indicates metallic nature of the surface, with a sharp asymmetric $2p^{3/2}$ peak at 778.1 eV. Unfortunately, Co is so active that a clean Co surface
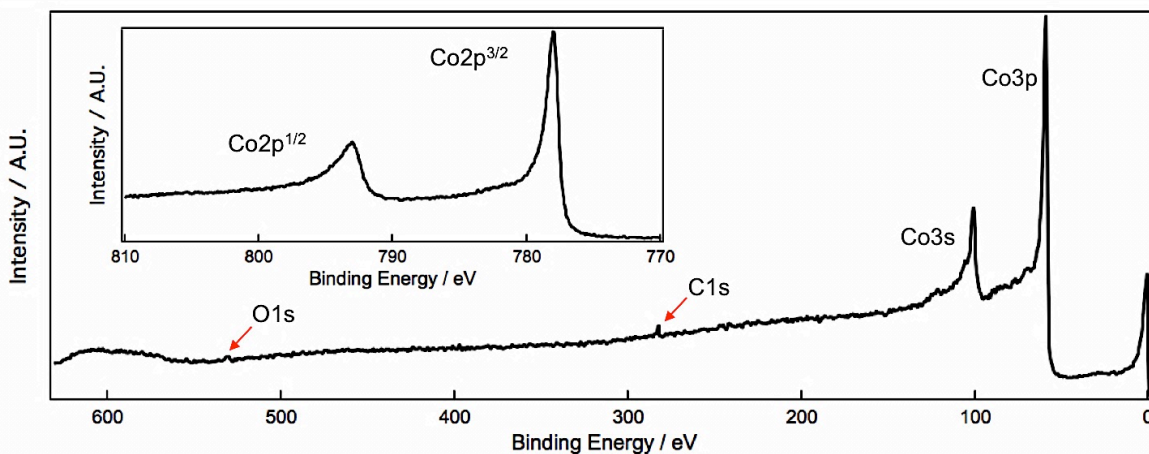

Figure 3-1. The survey spectra measured on the clean Co surface with 735 eV incident photon energy. The inset is the Co*2p* XPS spectra measured with 1000 eV photons.

cannot be maintained for a long time even in UHV. If we waited until the foil cooled down to room temperature in UHV, surface contaminants from the UHV background, such as CO and CH$_x$, could be spotted again in XPS spectra, especially after intensive experiments in the analysis chamber under ambient pressures of CO and H$_2$. Nonetheless, these surface contaminants did not oxidize the Co surface. Since we intended to study CO hydrogenation reactions, one strategy to circumvent this problem is to intentionally cover the surface with CO, to protect it from adsorbing the contaminants present in the UHV background. However, as will be discussed below, CO molecules can dissociate rapidly on Co surface at temperatures higher than 140°C. Therefore, CO can only be introduced below this temperature. Around 140°C, CO may still decompose slowly, resulting in small amount of carbide-like carbon and oxide-like oxygen species on the surface after the foil is cooled down to room temperature, as can be seen in some of the C$1s$ and O$1s$ spectra presented later.

3.1.2 XPS Measurement Parameters

The XPS spectra for each element were acquired with such incident photon energy that the kinetic energy of ejected photoelectrons is about 200 eV. For instance, 490 eV incident photon energy was used for C$1s$ spectra, 735 eV for O$1s$, and 1000 eV for Co$2p$. The energy scales were calibrated by shifting the Fermi edge positions measured with
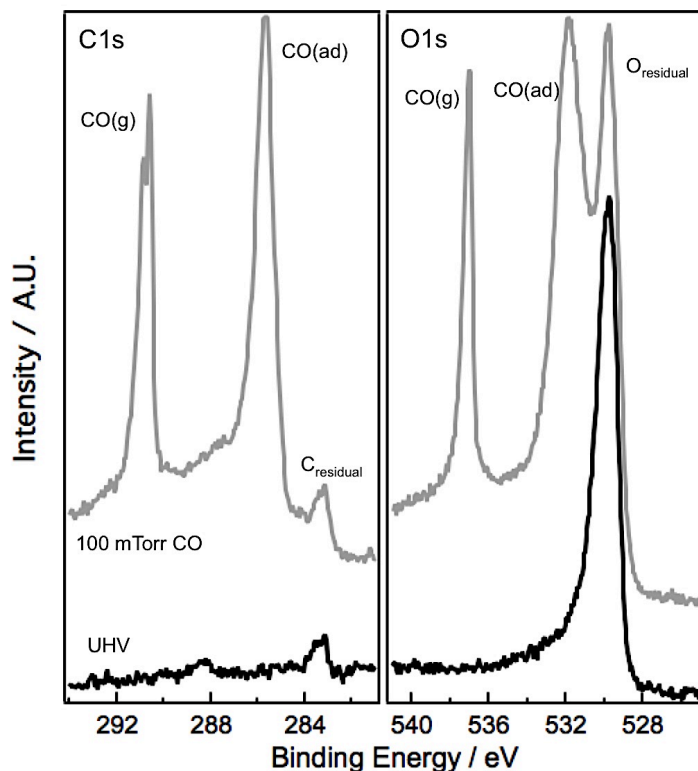

Figure 3-2. C$1s$ and O$1s$ XPS spectra before and after introducing 100 mTorr CO.

each photon energy to zero, except for Co*2p*. For Co*2p* spectra, the kinetic energy of those photoelectrons coming from the Fermi edge is about 1000 eV, which is out of the measureable energy range of the analyzer. Instead, the calibration was done by aligning the energy positions of O*1s* components measured with 735 eV and 1000 eV incident photon energies. According to the electron IMFP database, the probing depth of the photoelectrons with 200 eV kinetic energy is around 0.6 nm.[9]

3.1.3 CO Adsorption/Desorption on Cobalt Foil

Upon introduction of CO, new peaks could be immediately observed in O*1s* and C*1s* spectra, as shown in Figure 3-2. The new peak located at 285.7 eV in the C*1s* spectrum and the one at 531.8 eV in the O*1s* spectrum can be assigned to the surface adsorbed CO.
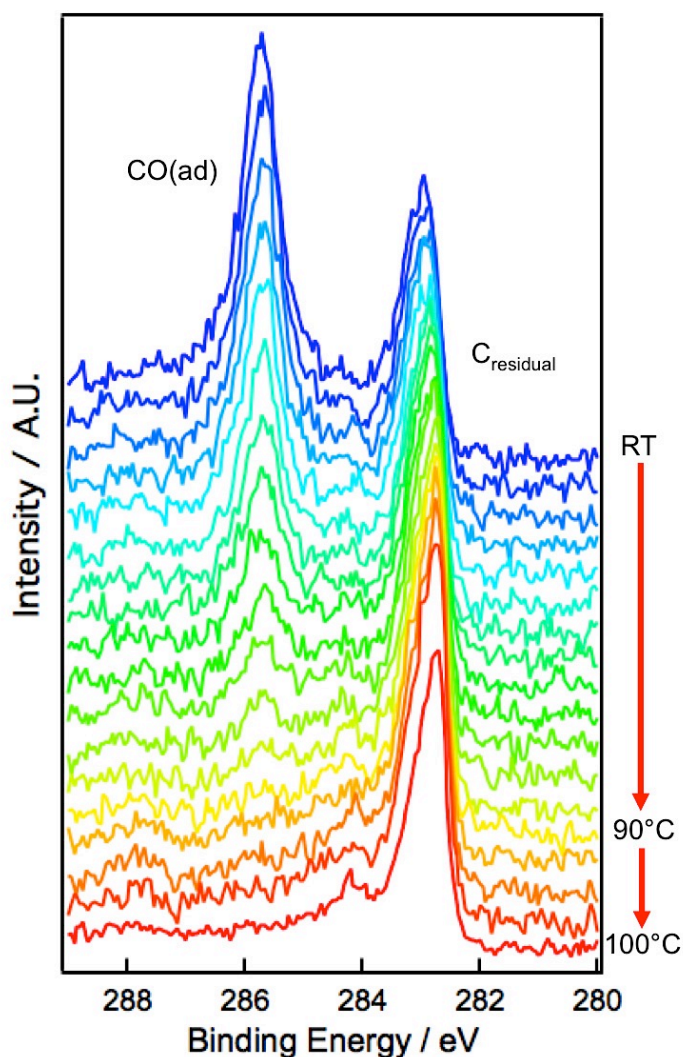

Figure 3-3. C*1s* XPS spectra measured in UHV at elevated temperatures, illustrating CO desorption on the Co surface.

When the CO pressure is higher than 50 mTorr, distinct gas-phase CO peaks appeared in both C*1s* and O*1s* spectra, at ~291 eV and ~537 eV, respectively.

When gas phase CO was evacuated, adsorbed CO molecules did not desorb completely. At elevated temperatures, adsorbed CO molecules started to desorb in UHV, as shown in the temperature-dependent C*1s* XPS spectra in Figure 3-3. Adsorbed CO molecules fully desorbed when the temperature reached about 90°C, leaving only carbide-like contaminants on the surface.

The cobalt foil that was used in this study contains ppm level of sulfur in the bulk. At the beginning of the experiment, sulfur segregated to the surface during high-temperature annealing, evidenced by S*2p* doublet peaks in the survey spectrum. Since sulfur is a common poison for many gas-phase catalysts,[10,11] we intentionally left small amount of sulfur (~0.05 ML) on the foil surface and investigated such surface as a model system for sulfur-poisoned catalysts. When CO was introduced, the same CO adsorption peaks appeared in both C*1s* and O*1s* XPS spectra. Upon evacuation of gas-phase CO, the peak related to adsorbed CO molecules substantially decreased (Figure 3-4), indicating much easier desorption on such sulfur-poisoned Co surface. Although the surface coverage of sulfur was very small, it seemed to have strong affect on the binding strength of CO on Co surface, which may contribute significantly in the poisoning effect of sulfur.
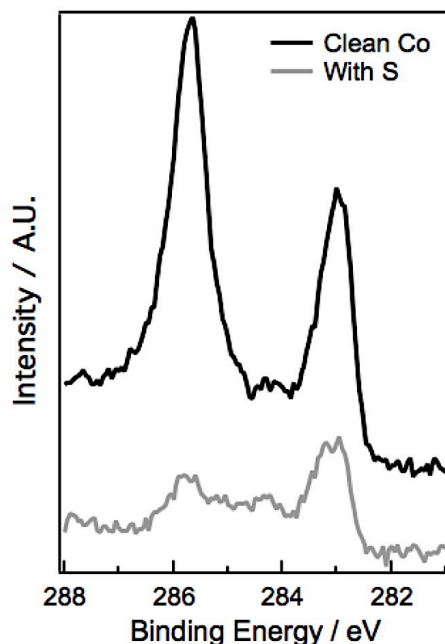

Figure 3-4. Comparison of C*1s* XPS spectra on clean and sulfur-poisoned Co surfaces after evacuating gas phase CO.

3.1.4 Cobalt Foil under Syngas

To investigate the chemical changes of Co foil under syngas, i.e. a mixture of CO and H_2, CO was first introduced during the cooling process, as the protecting agent. When the foil was cooled down to room temperature, H_2 was then introduced. Upon the introduction of H_2, Co surface became partially oxidized. Under 97 mTorr CO + 3 mTorr H_2 mixture, Co*2p* XPS spectrum indicated mostly metallic surface, but the oxide component at 529.8 eV increased slightly in the O*1s* spectrum. When H_2 partial pressure was higher than 10%, discernible oxide components at higher binding energies could be found in the Co*2p* spectra. When H_2/CO ratio reached 1:1, the oxidized Co component became dominant, as shown in Figure 3-5, with prominent satellite features similar to the spectrum of bulk CoO_x. Such bulk oxidation is particularly surprising, considering that H_2 is supposed to be a reducing agent. Similar oxidation was also observed in a control experiment when Co foil was cooled down in pure H_2 after the cleaning process.
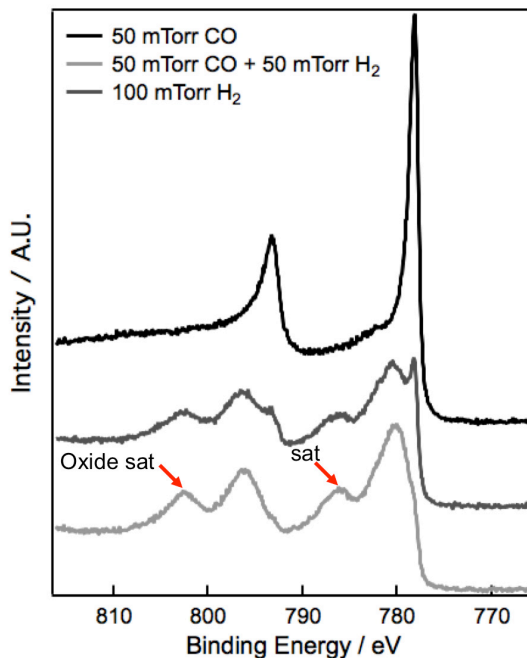

Figure 3-5. Co*2p* XPS spectra measured under pure CO, CO + H_2 and pure H_2.

The Co foil was slowly heated up under syngas with different CO/H_2 ratios, while chemical changes on the surfaces were monitored by recording XPS spectra at different temperatures. For all the CO/H_2 ratios tested, similar trends were observed. Figure 3-6 illustrates the O*1s* spectral evolution under 1:1 CO/H_2 mixture. While adsorbed CO began to desorb upon heating, Co surface first got more oxidized, as evidenced by growing intensity of the oxide component located around 529.8 eV (from the blue curve to yellow). When the temperature reached above 220°C, the oxide component stopped

growing and started to diminish rapidly, together with component related to adsorbed CO. When the temperature increased to ~300°C, the adsorbed CO peak almost disappeared, despite the presence of 50 mTorr CO in the gas phase. Meanwhile, the intensity of the oxide component substantially decreased, to an even lower level compared to what we started with, indicating that Co surface was metallic again. The metallic nature of the Co surface was also confirmed by Co2p XPS spectra. In the actual industrial applications, Co-catalyzed F-T processes that produces hydrocarbons usually operate around 300°C.[1] Therefore, the disappearance of adsorbed CO is possibly indicative of the occurrence of F-T reaction. Given that the probing depth of our XPS measurement is about 0.6 nm, we can conclude that the top surface of active Co catalysts under such conditions is indeed metallic.
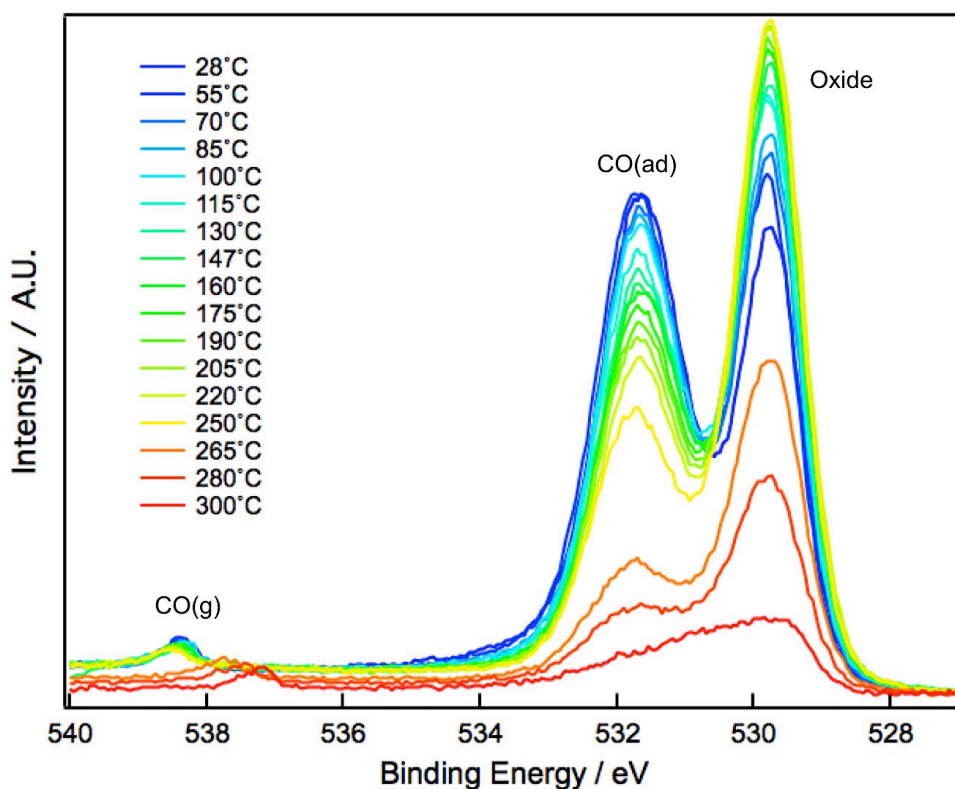
Figure 3-6. O*1s* XPS spectra measured under 100 mTorr of 1:1 mixture of CO/H$_2$ with increasing temperatures. Each spectrum was acquired at a different spot to avoid beam damage. Similar precautions were taken for all the measurements in the presence of CO.

Another noticeable trend is that the gas-phase CO peak at ~538 eV moved around during the entire process. At lower temperatures, the gas-phase peak shifted towards higher binding energy slightly (from blue curve to yellow). The moment when Co started to get substantially reduced, the gas-phase peak shifted towards lower binding energy rapidly (from yellow curve to red). The shift of gas-phase peak is related to the work function of

the surface, which is also correlated to the chemical states of the surface.[12] In this case, the shifts indicated that the work function of the foil surface first increased until ~250°C and then rapidly decreased. The correlation between the gas-phase peak shifts with the chemical changes observed in O$1s$ XPS spectra suggests that the surface oxide layer has a larger work function than the CO-covered metallic Co surface.

One interesting question still remains unexplained: What caused the oxidation of Co, even at room temperature? CO itself can oxidize Co if it dissociates and passes on the oxygen to Co. But CO dissociation occurs at elevated temperatures, as illustrated in the CO dissociation test (Figure 3-7). The inset of Figure 3-7 shows the intensity of the carbide-like component at ~283 eV as a function of temperature. The results indicate that CO only substantially dissociate on Co surface when the temperature is above 140°C. At room temperature, CO alone cannot oxidize Co. Another possibility is the impurities in H$_2$. It is known that small amount of water always exists in H$_2$. Although a liquid nitrogen
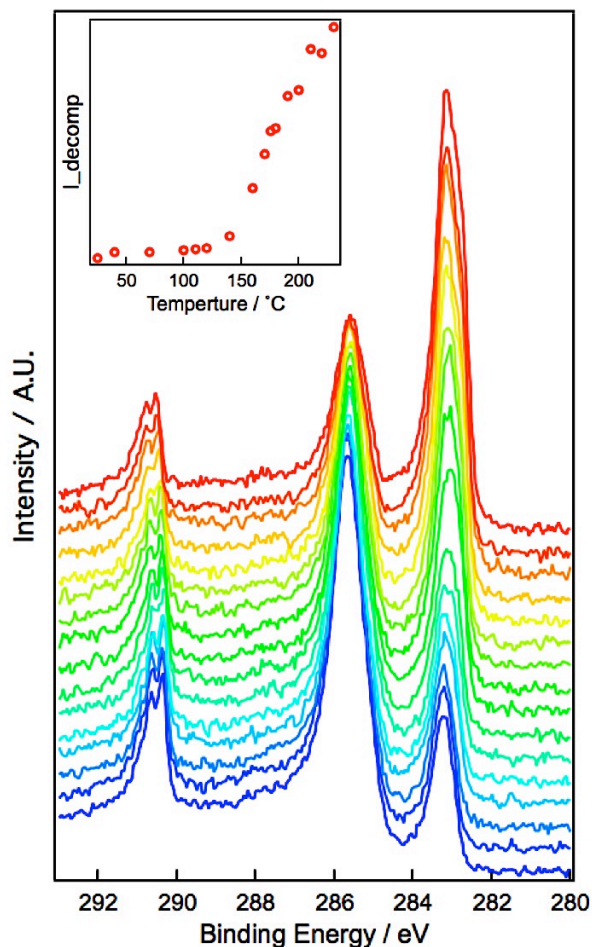

Figure 3-7. C$1s$ XPS spectra measured under 100 mTorr CO with increasing temperatures. The inset shows the intensity of the carbide-like component at ~283 eV, which is related to the CO dissociation products, as a function of temperature.

cold trap was used to freeze possible water contaminant before the H_2 gas was introduced into the analysis chamber, small percentage of H_2O could still be detected by the mass spectrometer equipped in the chamber. In order to find out how much water it takes to oxide Co surface, a control experiment was performed by dosing water vapor with low pressures onto clean Co surface at room temperature. In this experiment, Co foil was cooled down in vacuum without introducing CO for protection, and Co surface remained metallic with small amount of contaminants from the UHV background. Under 1×10^{-7} Torr of water vapor, the Co surface still remained metallic, as shown in the Co$2p$ spectrum in Figure 3-8. When the pressure of water vapor increased to 1×10^{-5} Torr, CoO$_x$ components and their satellite features already became prominent, indicating severe oxidation of Co surface. The control experiment suggests that very small amount of water alone can oxidize Co at room temperature. A third possibility is that at low temperatures, H_2 assists the dissociation of CO on the Co surface, as suggested by Tuxen et al.[13] However, more experiments are required to prove or disprove such possibility.

The oxidative ability of water has serious impact on the catalytic activity of Co. In F-T reactions, other than the long-chain hydrocarbons, water is also a reaction product. This means that on an active catalyst surface, water is constantly produced *in situ*. If the reaction temperature is not high enough, the water molecules produced at the surface will immediately oxidize Co and the catalytic activity will drop immediately. Only when the temperature is high enough to dissociate H_2 and then reduce CoO$_x$ back to metallic Co,
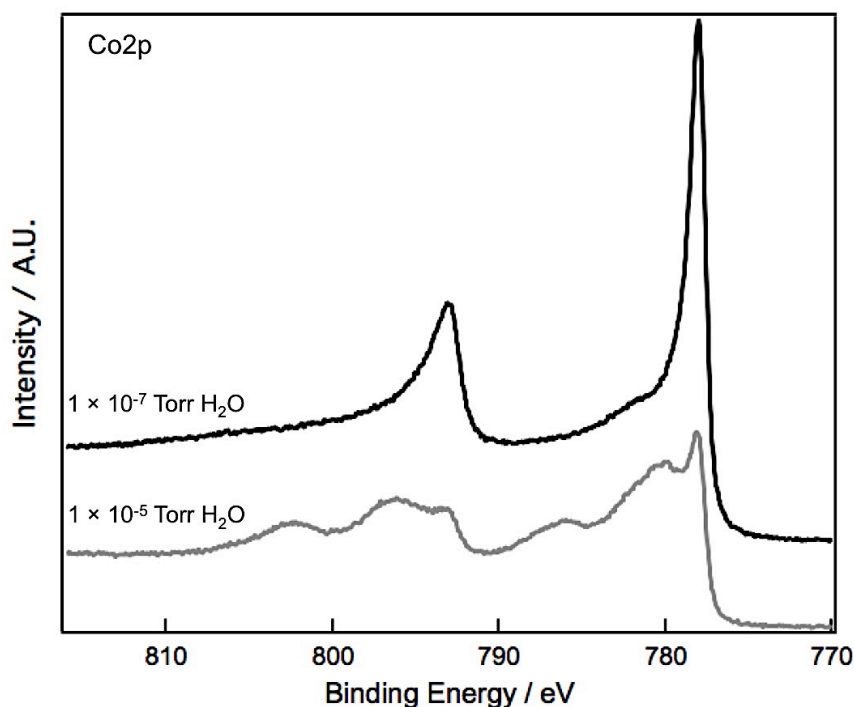

Figure 3-8. Co$2p$ XPS spectra measured under different pressures of water vapor.

the reaction can keep on going. This would explain why in the experiments under syngas, Co foil first got even more oxidized at relatively low temperature, and then became metallic again at temperature above 250°C. This also explains why Co-based catalysts are typically used under syngas with high H_2 content, as excess H_2 is necessary to keep the Co surface metallic and the catalyst active. In addition, some noble metal additives, such as trace amount of Pt, Pd, Ru, and Re, are commonly used to facilitate the dissociation of H_2 and the reduction of Co catalyst at lower temperatures.

3.2 Cobalt-Palladium Alloy Nanoparticles for CO Oxidation Reaction

CO oxidation is one of simplest prototype reactions for gas-phase catalysis. It also has important industrial applications, such as automobile exhaust treatment,[14,15] trace CO removal for proton-exchange membrane fuel cells.[16,17] Many Pt-based alloy nanoparticles such as Pt-Co, Pt-Ni, and Pt-Fe, have shown much improved activity in such catalytic reactions compared to single-element catalysts.[18–20] Recently, Pd-based alloy nanoparticles have also attracted much attention,[21–24] paralleling studies of Pt-based alloy catalysts. Co_xPd_y alloy nanoparticles are among the list of promising bimetallic alloy catalysts. These alloy nanoparticles showed promising activities in CO oxidation reaction compared to each of the metals alone, which makes such alloy system a perfect platform to investigate the synergetic effect of alloys in catalytic reactions.

3.2.1 Nanoparticle Synthesis and Composition-Dependent Catalytic Activities

Co_xPd_y alloy nanoparticles were synthesized via the thermal decomposition of Pd and Co precursors in a tributylphosphine(TOP)/oleylamine(OA) solution. Precursors $PdBr_2$ and Co(acetylacetonate)$_2$ (Co(acac)$_2$ for short) were dissolved in 20 ml OA with 1 mmol TOP pre-dissolved in it. The amount of $PdBr_2$ was fixed at 0.3 mmol, whereas different amount of Co(acac)$_2$ was added in the mixture to control the Co content in the alloy nanoparticles. The mixture was heated to 90°C and degassed in vacuum for 1 hour. Then the mixture was heated to 260°C under nitrogen protection and kept for 2 hours. After cooling down to room temperature, the nanoparticles were precipitated out of the solution by adding 50 ml ethanol and centrifuging at 8000 rpm for 8 minutes. The nanoparticles were further purified by dispersing in hexane and once again precipitating by ethanol for at least three cycles.

The alloy nanoparticles synthesized via the procedure described above have spherical shapes, with very narrow size distribution, as shown in the representative TEM images in Figure 3-9. By adjusting the ratio between the Pd and Co precursors, we can tune the Co content in the alloy nanoparticles, while retaining the monodispersity of the products. The

nanoparticles used in the catalytic measurements and *in situ* XPS characterization have an average diameter of ~4.5 nm with different Co content, ranging from 0% to 50%. The compositions of the alloy nanoparticles were confirmed by inductively coupled plasma mass spectrometry (ICP-MS). Before the catalytic activity tests, the alloy nanoparticles were loaded on mesoporous alumina support, heated in pure O_2 at 300°C for 5 hours to remove the organic ligands and then in pure H_2 at 150°C for 30 minutes.
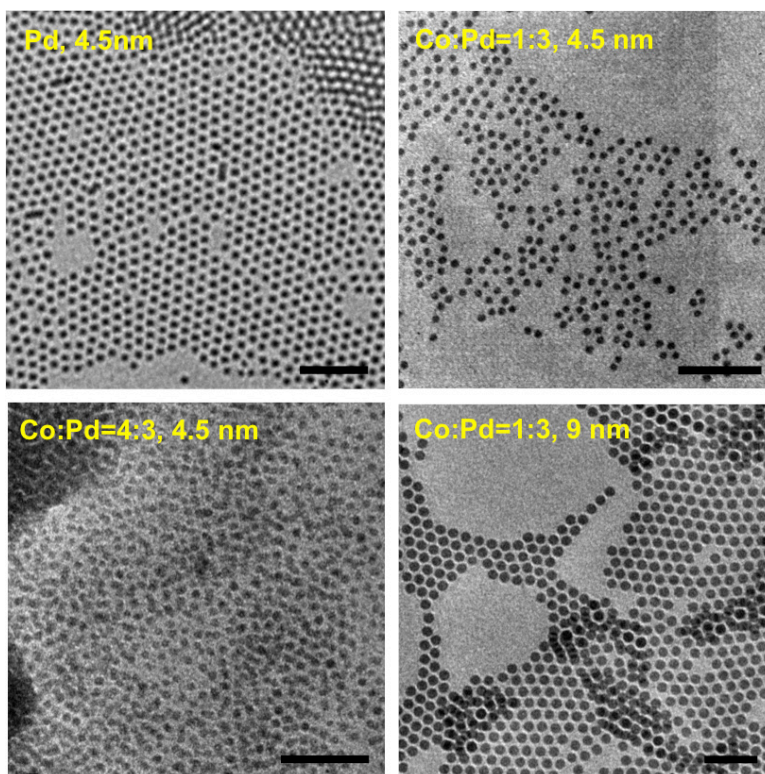

Figure 3-9. Typical TEM images of monodisperse Pd or Co_xPd_y nanoparticles with different compositions. The scale bar is 5 nm in all images.

Catalytic activities of these nanoparticles were tested in a flow reactor, equipped with a gas-chromatography (GC) detector to monitor the compositions of the gas mixture that had passed through the catalysts loaded on alumina support. CO_2 conversion yields were calculated based on the percentage of CO, O_2, and CO_2 in the gas mixture and plotted against the reaction temperatures. The results are summarized in Figure 3-10. A clear dependence of catalytic activity on the Co content was observed. With pure Pd nanoparticles, full conversion could be achieved at ~170°C. When small percentage of Co, up to 26%, was introduced in the alloy nanoparticles, the minimum temperature for full conversion dropped below 120°C. However, when the Co content in the alloy nanoparticles kept increasing, the minimum temperature for full conversion stopped decreasing but increased again. Once the Co content reached ~50%, the catalytic activity

became worse than pure Pd nanoparticles. The five samples with different Co content, from Pd to $Co_{52}Pd_{48}$, will be referred to as sample No.1 to No.5 in the following.
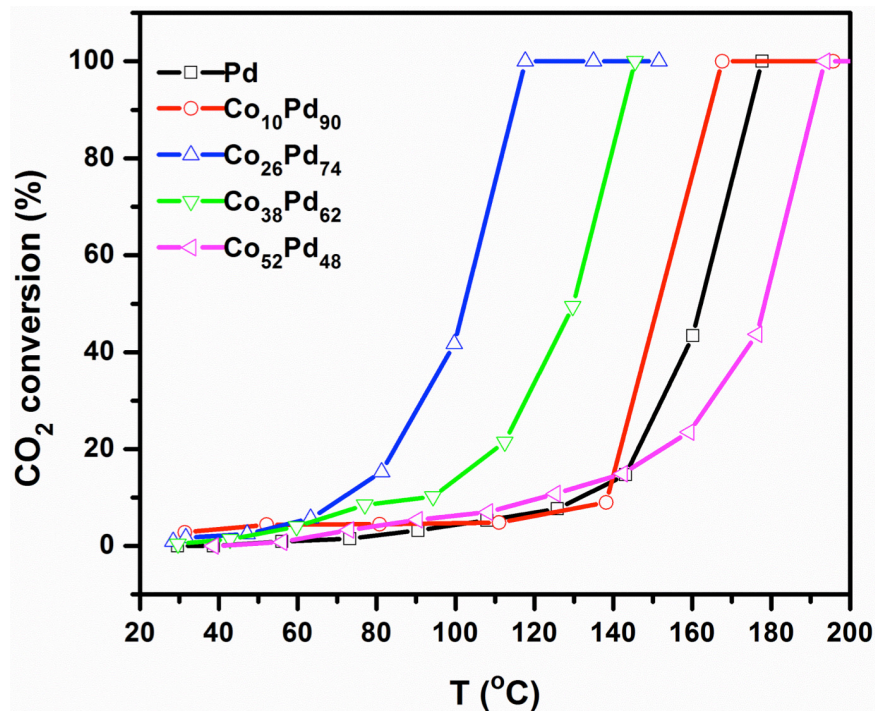

Figure 3-10. Temperature-dependent CO_2 conversion yield for nanoparticles with different Co content.

In order to understand the physical origin of the composition-dependence in catalytic activities, a series of *in situ* measurements were carried out at the AP-XPS endstation at Beamline 9.3.2.

3.2.2 Chemical Changes during Pre-Treatment Processes

As-synthesized alloy nanoparticles are usually wrapped in organic ligands, which potentially prevent the adsorption of reactants and the reaction between them. Before they can be used for catalysis, the nanoparticles have to go through some pre-treatment processes to remove the surface ligands. Typical pre-treatment processes involve a series of oxidation/reduction cycles: Oxygen helps combust the organic ligands, but also oxidize the metals, at least on the surface; then hydrogen is used to reduce the oxidized surface or oxidized particles back to its metallic phase. Since the same conditions (1 atm of O_2 or H_2) used before the catalytic activity tests cannot be realized in the AP-XPS chamber, we modified the pre-treatment procedure accordingly, and monitored the chemical changes at the nanoparticle surfaces by AP-XPS during the modified pre-treatment process. The detailed pre-treatment procedure involved a few cycles of

oxidation/reduction, until the carbon composition in the XPS spectra stayed mostly unchanged between two consecutive reduction cycles. The oxidation was performed under 500 mTorr O_2 at 300°C for 20 minutes, and the reduction was under 200 mTorr H_2 at 150°C for 20 minutes.

Because the insulating nature of alumina support can cause severe charging issues during XPS measurement, instead of loaded on alumina support, the nanoparticles were drop-casted on a piece of silicon substrate for AP-XPS measurements. The native oxide layer on the silicon surface serves as a substitute of inert oxide support for the catalysts. C*1s* XPS spectra were continuously monitored during the pretreatment. After each oxidation/ reduction step, XPS spectra in Pd*3d*, Co*3p*, and C*1s* regions were collected with incident photon energy of 730 eV or 500 eV. The energy scales were calibrated by setting the Fermi edge position of silicon substrates to zero with each incident photon energy.

Before any treatment, neither Pd nor Co was discernible in the XPS spectra, because the nanoparticles were wrapped in thick layers of organic molecules, which can be confirmed by the intense peaks in all the C*1s* spectra, shown as the black curves in Figure 3-11. The broad line shapes of C*1s* peaks indicate multiple carbon components involved. In
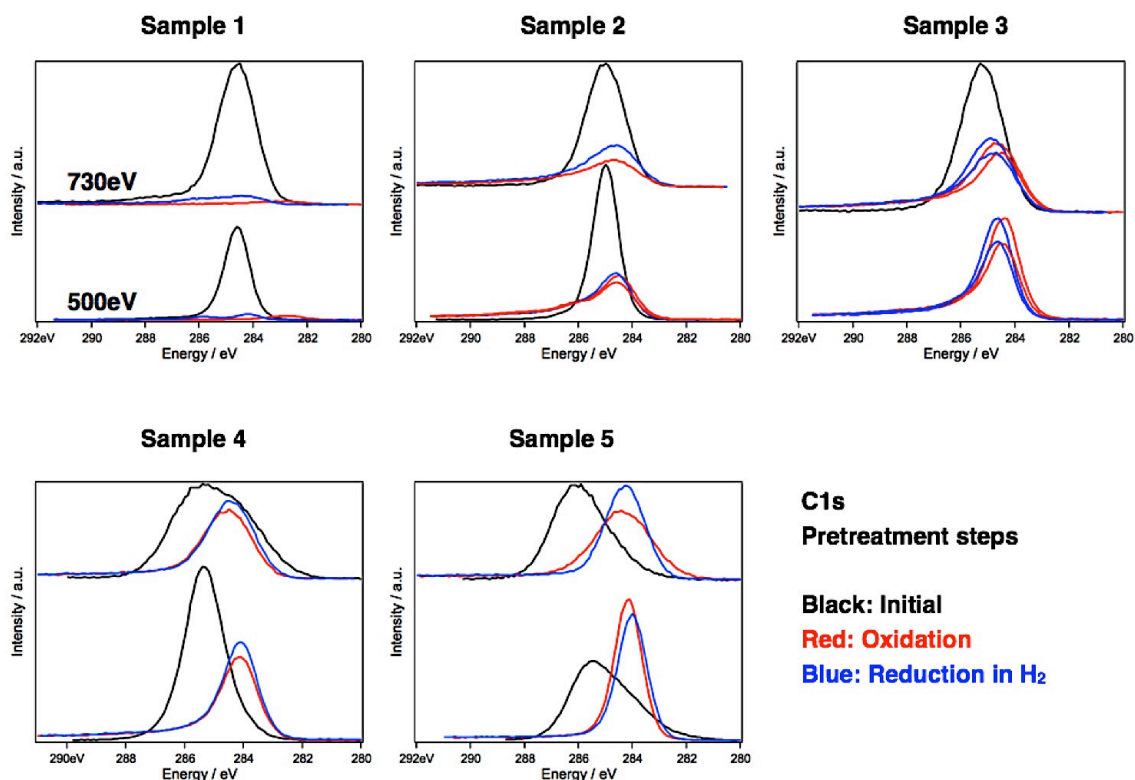

Figure 3-11. Summarized C*1s* XPS spectra of five different samples, measured with two different incident photon energies (500 eV and 730 eV) during the pre-treatment steps.

43

addition, the peak positions and detailed shapes are also different among the samples, which may be related to different coordination chemistry on the surface with different Co content. Nonetheless, the characteristics of surface ligand have very little relevance to the purpose of this study; therefore, initial C$1s$ spectra were not analyzed in detail.

During the treatment steps, Pd$3d$ and Co$3p$ peaks started to grow, as the surface carbon was gradually removed. According to the XPS spectra in the Pd$3d$ and Co$3p$ regions, Pd was oxidized and reduced as expected during oxidation/reduction cycles, but Co stayed mostly oxidized. Typically after two cycles of oxidation/reduction, the C$1s$ peak stopped decreasing substantially. If the intensities of the C$1s$ peak of untreated samples were used as a reference, an interesting trend can be observed after the last cycle of reduction: the more Co content in the alloy nanoparticles, the more carbon residue on the surface. This is probably a result of higher solubility of carbon in Co/CoO$_x$ than in Pd.[8] More cycles of oxidation/reduction were performed on sample No. 3, but the removal rate was very slow after the second cycle. It may be possible to remove more carbon using higher treatment temperature, but higher temperature will also induce severe sintering between nanoparticles as well as alloy effect between silicon substrate and the nanoparticles. After the pre-treatment, the alloy nanoparticles were cooled down to room temperature in vacuum.

3.2.3 Surface Evolution under Reaction Gases

In order to understand the interactions between the catalysts and individual reactants, the pre-treated Co$_x$Pd$_y$ alloy nanoparticles were first exposed to 100 mTorr O$_2$ or 100 mTorr CO separately at different temperatures. At 300°C, Co$_x$Pd$_y$ alloy nanoparticles were further exposed to the 100 mTorr mixture of CO and O$_2$ with different ratios (1:4 or 4:1). Pd$3d$, Co$3p$, and C$1s$ regions in the XPS spectra were monitored by AP-XPS under 100 mTorr gases at different temperatures, with incident photon energies of 500 eV.

Figure 3-12 shows the collection of all XPS spectra in the Pd$3d$ region. For the photoelectrons excited from Pd$3d$ orbitals with 500 eV x-ray photons, their kinetic energies are around 160 eV, which corresponds to approximately 0.5 nm probing depth.[9] All the red spectra correspond to O$_2$ only or O$_2$ rich conditions, whereas all the blue ones were acquired under CO only or CO rich conditions.

When pure Pd nanoparticles were exposed to O$_2$ or CO at 100°C, no obviously change can be observe in the line shapes of the Pd$3d$ spectra. But the intensity of Pd$3d$ peaks slightly decreased in the case of CO exposure. This is likely a result of strong CO adsorption on Pd surfaces. When the Pd nanoparticle surfaces are covered with large amount of CO molecules, the photoelectrons from Pd atoms will get scattered on their

way out, which reduces the overall intensities of Pd*3d* peaks. Since the surface carbon contamination can be almost completely removed on the surfaces of pure Pd nanoparticles, the adsorbed CO species could be resolved in the C*1s* spectra, as shown in Figure 3-13. At 100°C, the component at ~284 eV is related to the residual carbon contamination, which was future removed and almost disappeared after extended exposure to 100 mTorr O_2 at higher temperatures during the rest of the measurements. The component at ~291 eV corresponds to the CO molecules in the gas phase. The component at ~286 eV is associated with adsorbed CO on Pd surfaces, which disappear upon exposure to pure O_2. When exposed to 100 mTorr O_2 at higher temperatures, a prominent shoulder feature appeared on the higher energy side of the main Pd*3d* peak, indicating partial oxidation of Pd on the nanoparticle surfaces. When exposed to the mixture of CO and O_2 at 300°C, no matter O_2 rich or CO rich, Pd nanoparticle surface remained metallic, with negligible CO adsorption on the surface, indicative of fast kinetics of CO oxidation under such conditions.

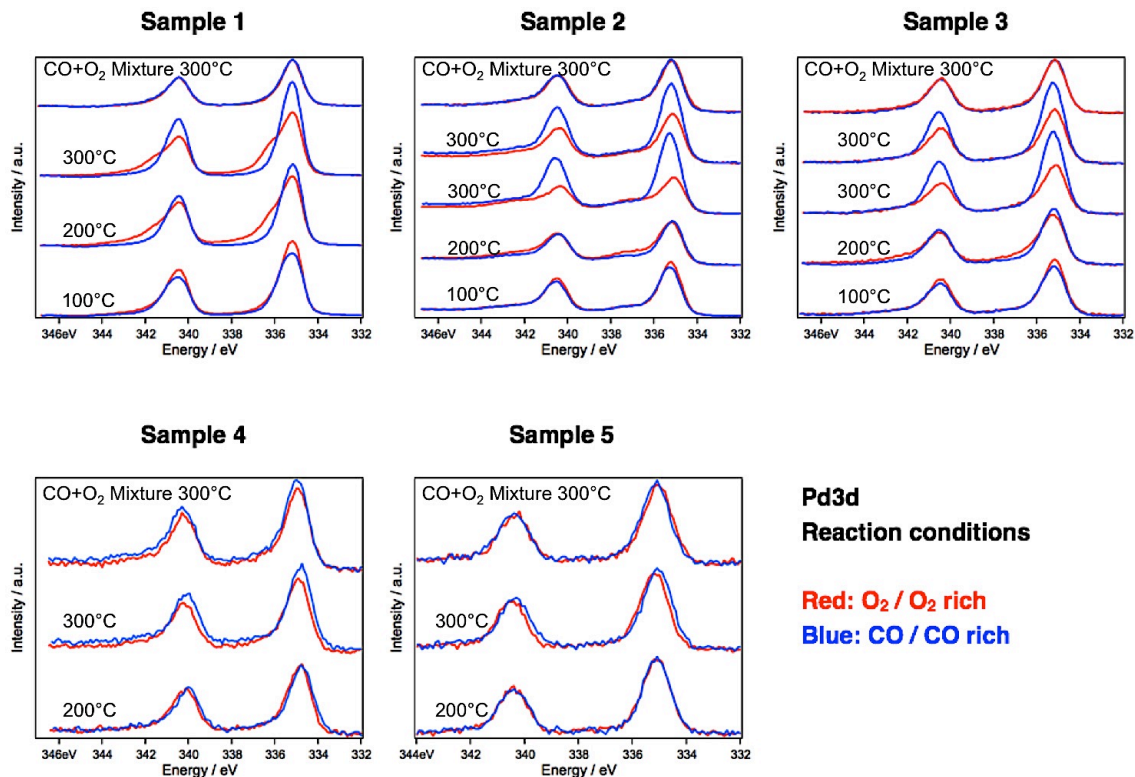**Figure 3-12.** Summarized Pd*3d* XPS spectra of five different samples, measured under 100 mTorr of pure O_2, CO, or mixtures of O_2/CO.

For alloy nanoparticles with small and medium Co content (10% and 26%), Co stayed oxidized under all the conditions. Unfortunately, the photon energy at Beamline 9.3.2 cannot reach Co*2p* region, therefore it is impossible to study the chemical states of Co in
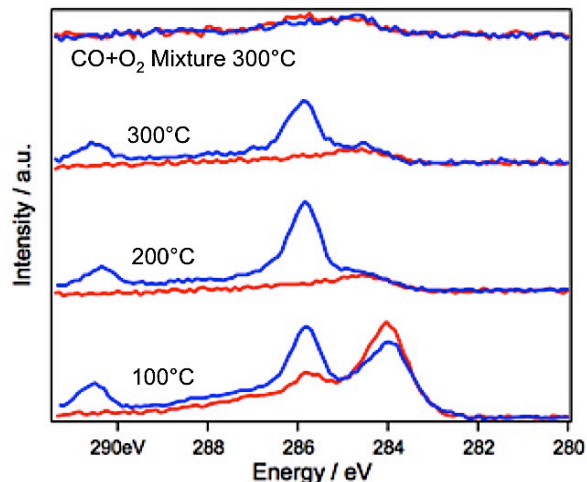
Figure 3-13. C*1s* XPS spectra of pure Pd nanoparticles measured under 100 mTorr of O_2, CO, or O_2/CO mixtures at different temperatures. Red spectra correspond to O_2 or O_2-rich conditions, and blue spectra correspond to CO or CO-rich conditions.

much detail. At 100°C, not much difference was observed in the Pd*3d* spectra under O_2 and CO, except slight intensity change resulting from the photoelectron scattering by surface adsorbed CO. But the adsorbed CO peak cannot be discerned in the C*1s* spectra, because of the carbon residuals as was discussed earlier. At 200°C, a very small oxide shoulder appeared with much smaller intensities compared to the case of pure Pd nanoparticles. At 300°C, other than the small oxide shoulder, large variation in the overall intensities was observed: under CO, Pd*3d* peaks are much more intense than under O_2. Such intensity variation is an indication of surface segregation of Pd under different gases.[25,26] Because CO binds strongly with Pd, more Pd atoms migrate to the surface under CO to lower the overall surface energy, which explains the higher Pd*3d* intensities. O_2 and related species are more likely to interact strongly with Co or CoO$_x$ on the surfaces; therefore more Co atoms stay on the surface under O_2 environment, leaving less Pd on the surface. For sample No.3, the shape of the Pd*3d* peaks are relatively more symmetric, indicating that more surface Pd atoms stayed metallic under O_2 in sample No.3; but in both samples, Pd was less oxidized compared to pure Pd nanoparticles under the same conditions. Lower level of oxidation of Pd also corroborated the argument that O_2 species preferentially bind to Co/CoO$_x$, which prevents the oxidation of Pd. For both samples, surface segregation of Co or Pd under O_2 or CO is somehow reversible, as illustrated in the Pd*3d* spectra during two cycles of O_2 and CO exposure at 300°C.

For samples with higher Co content (38% and 52%), more intense Co*3p* peaks were observed as expected. Co also remained oxidized during the entire process. Meanwhile, the signal-to-noise ratio in Pd*3d* spectra became noticeably worse, simply because Pd content was lower in these two samples. However, unlike the cases of sample No.2 and

No.3, when switching from O_2 environment to CO environment at 200°C, Pd$3d$ peak intensities didn't not change at all. At 300°C, the difference between Pd$3d$ spectra under O_2 and under CO was still quite small. One reasonable explanation of unchanged Pd$3d$ intensities is that after the pre-treatment process, larger amount of Co have already segregated to the surface and form a thin shell of CoO_x. This oxide shell on the surface prevents subsurface Pd atoms to migrate to the surface and bind with CO. As a result, the catalytic activity almost entirely depends on Co/CoO_x only.

Under total pressure of 100 mTorr O_2 and CO at 300°C, no matter O_2 rich or CO rich, Pd$3d$, Co$3p$, and C$1s$ spectra remained the same for all four alloy samples. Pd appeared to be metallic and Co was always oxidized.

3.2.4 Composition-Dependent Synergetic Effect

The activity test clearly showed synergetic effect of Co when added into Pd in the CO oxidation reaction. Based on the *in situ* XPS observations, a possible explanation for the composition-dependent activity is proposed, as illustrated in Figure 3-14.

In the as-synthesized alloy nanoparticles, Pd and Co are uniformly distributed, as evidenced by electron energy loss spectroscopy (EELS) elemental mapping. After the pre-treatment cycles, Co is segregated on the surface of the nanoparticles. The reduction temperature of 150°C is not high enough to fully reduce the surface-segregated Co into its metallic phase, leaving oxides on the surface.

When the initial Co concentration is low, surface-segregated CoO_x has very low coverage on the nanoparticle surface, with many metallic Pd atoms exposed on the surface. As a result, when the CO/O_2 mixture is introduced on the surface, CO preferentially binds to Pd, whereas O_2 binds to CoO_x and possibly dissociates. At the boundary of Pd/CoO_x, an oxygen atom bonded to the CoO_x surface can be passed on to a CO molecule adsorbed on neighboring Pd atom, and eventually form a CO_2 molecule. However, because of the low coverage of such CoO_x islands on the nanoparticle surfaces, the majority of surface Pd atoms still catalyze the CO oxidation reaction by themselves, just as in the case of pure Pd nanoparticles. Therefore, the improvement of catalytic activity is limited. When more Co is added to the alloy nanoparticles, the coverage of the surface-segregated CoO_x species after the pre-treatment processes becomes higher. As a result, more Pd/CoO_x boundaries are created, which further promote the CO oxidation reaction; and the synergetic effect of the alloy becomes more prominent. Once the Co content reaches beyond 25%, the surface-segregated CoO_x species dominate on the surface and eventually covered the entire Pd-rich core. With such oxide thin shell on the surface, the subsurface Pd atoms cannot migrate to the surface even at 300°C, and thereby can no

longer bind with CO molecules. Under such circumstances, the catalytic activity entirely depends on the CoO_x shell and has little to do with Pd.
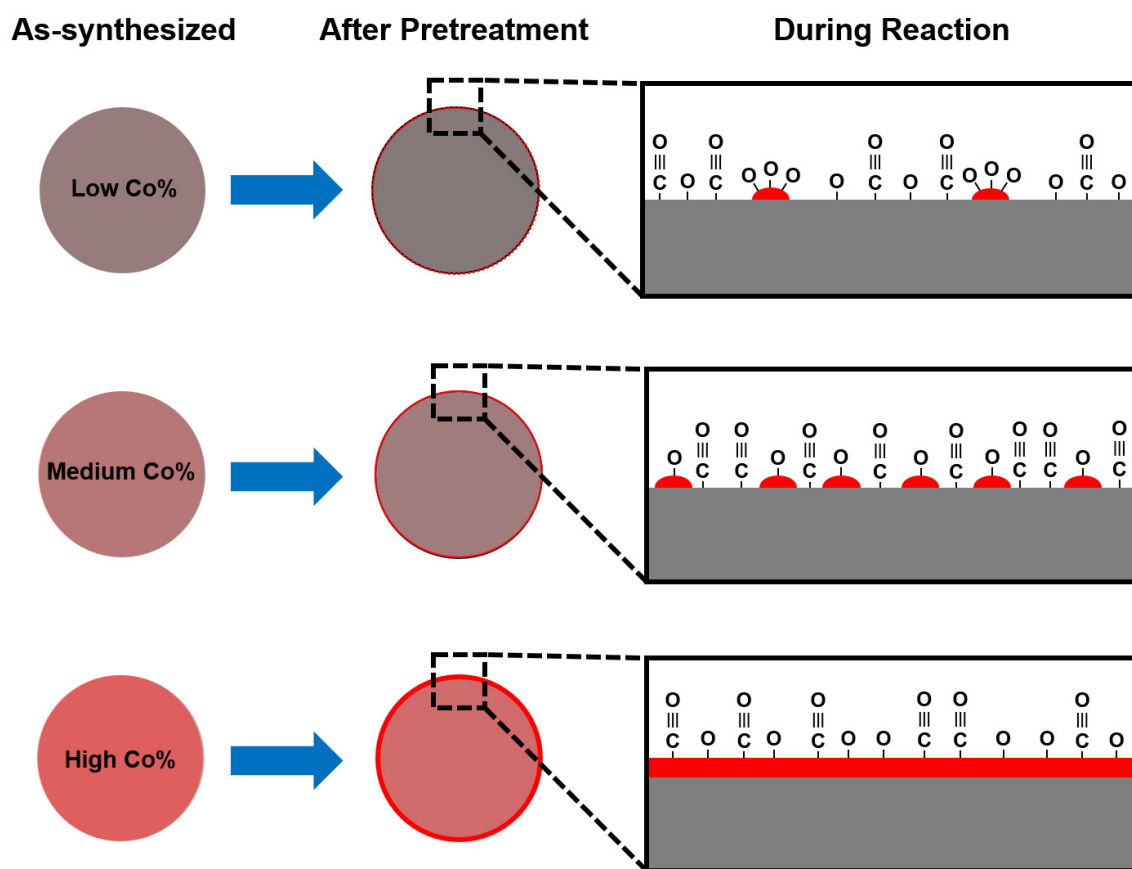

Figure 3-14. Schematic illustration of the proposed mechanism for the synergetic effect in Co_xPd_y alloy nanoparticles for catalyzing CO oxidation reaction.

The proposed mechanism for the synergetic effect in Co_xPd_y alloy nanoparticles explains why there exists an optimal Co composition for the catalytic CO oxidation reaction. The irreversibility of Co segregation and oxidation on the surface plays an important role. Similar synergetic effect was also observed in Ni_xPd_y nanoparticles as CO oxidation catalysts.[24]

If much higher reduction temperature is used to fully reduce CoO_x back to its metallic phase, one can expect the segregation of Pd atoms to the surface under CO even with high Co content, considering that Pd is more favored on the surface under reducing environment. With coexistence of both elements on the surface, the synergetic effect will become prominent again. A control experiment was performed to reduce the high-Co-content nanoparticles in H_2 at temperature above 400°C. Preliminary catalytic activity test showed enhanced activity initially. However, the activity dropped rapidly, possibly

because of surface CoO_x formation under CO/O_2 mixture. Although the strategy of full reduction of Co did not prove to be an effective solution for long-term improvement of the catalytic activity, but it did partially corroborate the proposed mechanism.

3.3 Conclusions

The two examples studied by ambient-pressure XPS illustrate the capability of such *in situ* and *operando* characterization techniques, especially for the investigation of reaction mechanisms and other fundamental aspects of gas-phase catalysis.

In the study regarding Co catalyst in Fischer-Tropsch synthesis, it was found that CO adsorbs strongly on the Co surface; but small amount of sulfur substantially weakens the CO adsorption and thus poisons the reaction. Under reaction conditions, the Co surface remains metallic. The water molecules in the reaction products can potentially oxidize the Co surface and hence hinder the catalytic reaction. When the temperature is high enough, H_2 is responsible for reducing Co to metallic phase and keeping the catalyst active.

In the study of Co_xPd_y alloy nanoparticles for catalyzing CO oxidation reaction, a clear dependence of catalytic activities on the nanoparticle compositions was observed. AP-XPS results helped to elucidate the physical origin of such dependence. It was found that Co segregates to the surface in the oxide form after the pre-treatment. Small amount of Co coexisting with Pd on the surface promotes the CO oxidation reaction synergistically and the synergetic effect becomes more prominent with increasing Co content. However, when Co/Pd ratio is too high, after the cleaning processes, the surface of the nanoparticles is fully covered by thin layers of CoO_x, preventing CO molecules from binding with Pd, which leads to significant drop in catalytic activities of those nanoparticles.

3.4 References

1   M. E. Dry, *Catal. Today*, 2002, **71**, 227–241.
2   M. E. Dry, *Appl. Catal. A Gen.*, 1996, **138**, 319–344.
3   M. Ehrensperger and J. Wintterlin, *J. Catal.*, 2014, **319**, 274–282.
4   H. Karaca, O. V. Safonova, S. Chambrey, P. Fongarland, P. Roussel, A. Griboval-Constant, M. Lacroix and A. Y. Khodakov, *J. Catal.*, 2011, **277**, 14–26.
5   N. E. Tsakoumis, A. Voronov, M. Rønning, W. van Beek, Ø. Borg, E. Rytter and A. Holmen, *J. Catal.*, 2012, **291**, 138–148.

6   G. L. Bezemer, J. H. Bitter, H. P. C. E. Kuipers, H. Oosterbeek, J. E. Holewijn, X. Xu, F. Kapteijn, A. J. van Dillen and K. P. de Jong, *J. Am. Chem. Soc.*, 2006, **128**, 3956–3964.

7   G. Melaet, W. T. Ralston, C.-S. Li, S. Alayoglu, K. An, N. Musselwhite, B. Kalkan and G. A. Somorjai, *J. Am. Chem. Soc.*, 2014, **136**, 2260–2263.

8   K. Ishida and T. Nishizawa, *J. Phase Equilibria*, 1991, **12**, 417–424.

9   C. J. Powell and A. Jablonski, *NIST Electron Inelastic Mean Free Path Database, version 1.1*, National Institute of Standards and Technology, Gaithersburg, MD, 2002.

10   M. Ehrensperger and J. Wintterlin, *J. Catal.*, 2015, **329**, 49–56.

11   G. A. Somorjai and Y. Li, *Introduction to Surface Chemistry and Catalysis*, John Wiley & Sons, Inc.: Hoboken, NJ, 2010, 2nd ed., 1997.

12   S. Hüfner, *Photoelectron Spectroscopy -Principles and Applications*, Springer Berlin Heidelberg, Berlin, Heidelberg, 2003.

13   A. Tuxen, S. Carenco, M. Chintapalli, C.-H. Chuang, C. Escudero, E. Pach, P. Jiang, F. Borondics, B. Beberwyck, A. P. Alivisatos, G. Thornton, W.-F. Pong, J. Guo, R. Perez, F. Besenbacher and M. Salmeron, *J. Am. Chem. Soc.*, 2013, **135**, 2273–8.

14   M. V. Twigg, *Appl. Catal. B Environ.*, 2007, **70**, 2–15.

15   R. M. Heck and R. J. Farrauto, *Appl. Catal. A Gen.*, 2001, **221**, 443–457.

16   A. U. Nilekar, S. Alayoglu, B. Eichhorn and M. Mavrikakis, *J. Am. Chem. Soc.*, 2010, **132**, 7418–7428.

17   Q. Fu, W.-X. Li, Y. Yao, H. Liu, H.-Y. Su, D. Ma, X.-K. Gu, L. Chen, Z. Wang, H. Zhang, B. Wang and X. Bao, *Science*, 2010, **328**, 1141–1144.

18   H. Xu, Q. Fu, Y. Yao and X. Bao, *Energy Environ. Sci.*, 2012, **5**, 6313.

19   H. Xu, Q. Fu, X. Guo and X. Bao, *ChemCatChem*, 2012, **4**, 1645–1652.

20   G. Chen, Y. Zhao, G. Fu, P. N. Duchesne, L. Gu, Y. Zheng, X. Weng, M. Chen, P. Zhang, C.-W. Pao, J.-F. Lee and N. Zheng, *Science*, 2014, **344**, 495–499.

21   X. Liu, C. Meng and Y. Han, *J. Phys. Chem. C*, 2013, **117**, 1350–1357.

22   F. C. H. Lim, J. Zhang, H. Jin, M. B. Sullivan and P. Wu, *Appl. Catal. A Gen.*, 2013, **451**, 79–85.

23   W. Tang, L. Zhang and G. Henkelman, *J. Phys. Chem. Lett.*, 2011, **2**, 1328–1331.

24   S. Shan, V. Petkov, L. Yang, J. Luo, P. Joseph, D. Mayzel, B. Prasai, L. Wang, M. Engelhard and C.-J. Zhong, *J. Am. Chem. Soc.*, 2014, **136**, 7140–51.

25   F. Tao, M. E. Grass, Y. Zhang, D. R. Butcher, J. R. Renzas, Z. Liu, J. Y. Chung, B. S. Mun, M. Salmeron and G. A. Somorjai, *Science*, 2008, **322**, 932–4.

26   F. Tao, M. E. Grass, Y. Zhang, D. R. Butcher, F. Aksoy, S. Aloni, V. Altoe, S. Alayoglu, J. R. Renzas, C.-K. Tsung, Z. Zhu, Z. Liu, M. Salmeron and G. A. Somorjai, *J. Am. Chem. Soc.*, 2010, **132**, 8697–703.

Chapter 4

In Situ and *Operando* X-ray Absorption Spectroscopy Studies of Solid/Liquid Interfaces

Abstract

This chapter presents two case studies on solid/liquid interfaces by *in situ* and *operando* x-ray absorption spectroscopy. The combination of *in situ* and *operando* XAS characterization and first-principle simulations helped elucidate the chemical processes that happened at the solid/liquid interface. At the Au/H$_2$O interface, the electronic coupling between water molecules and the gold substrate profoundly altered the electronic structure of the interfacial water molecules and thus their O*1s* XAS spectra. These interfacial polar molecules can respond to external electrical field and reorient, producing potential-dependent O*1s* TEY XAS spectra. At the Pt/H$_2$SO$_4$(aq) interface, similar reorientation behaviors of interfacial water molecules were observed in the negative potential region. In the positive potential region, the changes in the O*1s* XAS spectra are possibly related to the sulfate ion adsorption at the interface, contradicting many reports that proposed an oxide formation or oxygen/hydroxyl adsorption processes. Similar spectral evolution was also observed at the Au/H$_2$SO$_4$(aq) interface. The results presented here demonstrate the power and the potential of the newly developed *in situ* and *operando* XAS technique.

4.1 The Gold/Water Interface

(This section covers similar content as in J.J. Velasco-Velez, C.H. Wu, et al., *Science* **2014**, *346*, 831-834, with permission from AAAS, Copyright 2014.)

Water and aqueous solutions play a vital role in chemistry, materials sciences, and especially biology.[1] Despite of its importance, liquid water is still quite a mystery. Over the past century, many generations of scientists have been actively seeking explanations for the peculiar physical and chemical properties of liquid water, a few of which are listed below:

- anomalously high boiling point, melting point, and critical temperatures for a small molecule that is neither ionic nor metallic;
- high heat capacity;
- high dielectric constant;
- high mobility for H^+ and OH^- ions;
- volume decrease during melting;
- maximum density at 4°C in the ambient liquid range.

The strong dipole moment of water molecules (1.85D) and the hydrogen-bonding network give rise to some of these distinct properties, such as the high boiling point and melting point.[2] XAS is sensitive to the local environment of the excited atoms and has proven to be a valuable tool to study the hydrogen-bonding network in liquid water.[3]

The interface between gold surface and water was chosen to be the proof-of-concept system, to demonstrate the interface sensitivity of TEY-based *in situ* XAS technique. The main reason we chose gold/water interface to start with, is the relative inertness of gold in the electrolysis of water. Without introducing complicated reaction intermediates and gaseous products at the interface, we can focus more on the structure and behaviors of the solvent molecules.

4.1.1 Experimental Setup and Sample Preparation

The experiment system consists of a flow liquid cell with an ultrathin Si_3N_4 membrane window, an x-ray modulation system, and other electronics, including a pre-amplifier, a lock-in amplifiers, a function generator, and a potentiostat. The details regarding the flow liquid cell and the x-ray modulation system were described previously in Section 2.3.

The gold thin film (20 nm), as the working electrode in this case, was thermally evaporated onto the flat side of the Si_3N_4 window, which faces the liquid during the measurement. No adhesion layer (typically chromium or titanium) was introduced between the Si_3N_4 surface and gold thin film, in order to prevent potential signal

interference from possible oxidation products of those metals. The gold film is polycrystalline and continuous, and consists of agglomerated nanoparticles. The grain size is about 15 - 20 nm. As shown in the atomic force microscopy (AFM) image (Figure 4-1), the thin film is reasonably smooth, with RMS value ~1nm over a 3μm × 3μm area, without any pinholes.
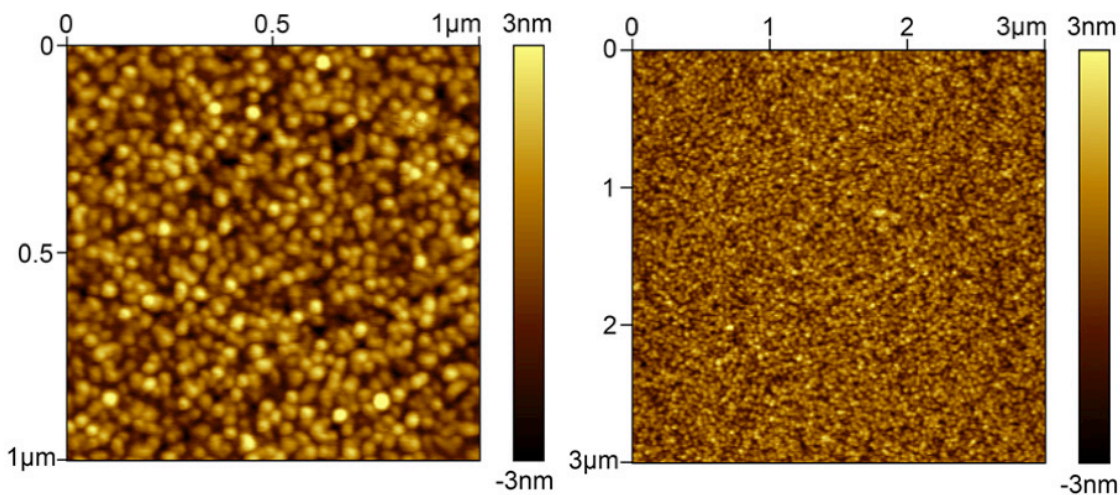

Figure 4-1. Typical AFM topographical images of the surface of the gold thin film deposited on the Si_3N_4 membrane. The RMS values for these two areas are 1.00 nm and 0.76 nm, respectively.

Slightly salted water (10μM NaCl solution) was used in the flow cell, to improve the conductivity of the liquid. Cyclic voltammetry (CV) result measured in a three-electrode configuration with a platinum counter electrode and a silver quasi-reference electrode, as shown in Figure 4-2, confirmed the lack of reactivity and ion adsorption at the interface between gold thin film and the dilute solution within the potential window in this study.

The hexadecane-thiol ($C_{16}H_{33}SH$) self-assembly monolayer (SAM) on gold substrate was prepared according to the procedure reported by Liu et al.[4] The Si_3N_4 window covered with 20 nm Au thin film was immersed in a ~2 mmol/L hexadecane-thiol ethanol solution for 36 hours at room temperature. After the complete formation of SAM, the window was taken out of the solution and rinsed with clean ethanol multiple times. The SAM formation could be readily verified by its super hydrophobicity. In order to prevent any water or oxygen molecules trapped in the array of alkyl chains, which may introduce extra features in the O*1s* spectra, the thiol-covered windows were kept in mild vacuum for more than 12 hours and then sealed in airtight packages inside an argon-protected glovebox. Shortly before the XAS experiments, the thiol-covered windows were taken out of the airtight packages inside a glove bag filled with nitrogen. Then static liquid cells were filled with water and assembled with these thiol-covered windows under nitrogen.
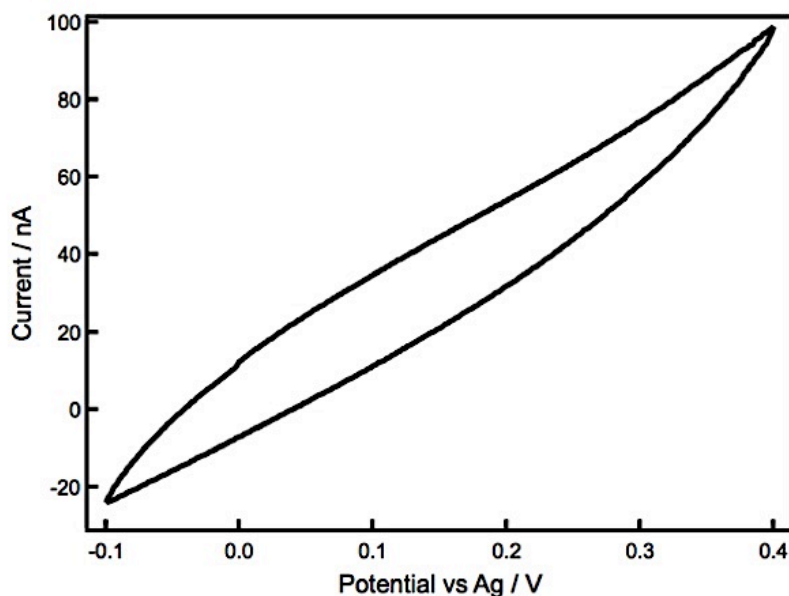
53

Figure 4-2. CV curve of the Au electrode in 10µM NaCl solution. Scan rate: 10 mV/s.

4.1.2 Spectrum Treatments and Simulation Procedures

The raw TFY and TEY spectra were first normalized to the photon flux, which is represented by a TEY current I_0, measured on a gold mesh at an upstream location inside the x-ray tube. Then a linear background was subtracted based on the fitted straight line in the flat region before the absorption edge. The energy scales were calibrated by comparing the measured t_{2g} and e_g peak positions in the O$1s$ spectra of standard reference TiO$_2$ sample with the values reported in the literatures. Finally, the spectra were normalized once more to the intensities at the onset of the continuum at 550 eV.[3]

The first-principle simulations were performed by the Prendergast group at the Molecular Foundry. *Ab initio* molecular dynamics (AIMD) simulations were used to explore the interfacial structure of water near the gold surface, followed by XAS spectra calculation with constrained-occupancy density functional theory (DFT) within the excited electron and core-hole (XCH) approach.[5] The details of the simulations were described in the article [*Science* **2014**, *346*, 831-834] and corresponding supplementary materials.[6]

4.1.3 Bulk Water vs. Interfacial Water

As discussed in Chapter 2, TFY spectra provide averaged information over several hundred nanometers of liquid water from the gold/water interface, which can be considered as bulk-sensitive spectra. The O$1s$ TFY XAS spectrum of water (curve (a) in Figure 4-3) that was measured from the liquid cell is indeed consistent with those

measured by other researchers,[7,8] which can be divided into three regions: pre-edge region, around 535 eV (I), main-edge region around 537 eV (II), and post-edge region around 540 eV (III). The pre-edge peak at ~535 eV is characteristic of the liquid phase and related to the dangling hydrogen bonds. The main edge is similarly related to the population of molecules with unsaturated hydrogen bonds, while the post-edge regions is associated with the fully saturated hydrogen-bonding network. In the O$1s$ XAS spectrum of bulk ice, the pre-edge and main-edge peaks are weak because almost all the hydrogen atoms participate in the hydrogen bonds. The pre-edge peak of liquid water is relatively prominent, while the post-edge is weaker compared to ice.
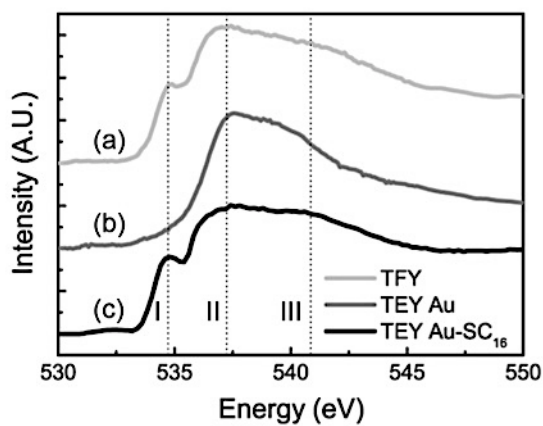

Figure 4-3. O$1s$ XAS spectra measured in the gold/water system.

Because of extremely small IMFP of electrons in liquids,[9,10] the secondary electrons collectable through the gold electrode are expected to come from just a thin layer of water molecules at close proximity to the surface of the gold electrode, given the fact that there is no oxygen atoms in the gold electrode. As a result, such TEY XAS spectra can provide interface-sensitive information at the gold/water interface. As can be seen in the O$1s$ TEY XAS spectrum (curve (b) in Figure 4-3) measured from the flow liquid cell at open circuit potential, no prominent spectra feature is visible at 535 eV, which might be interpreted as indicative of a much lower concentration of broken hydrogen bonds at the gold/water interface compared to bulk water.

However, first-principle simulations revealed that the contrary is true. Analysis of the AIMD trajectory indicated that 49% of the interfacial water molecules, i.e., water molecules within ~1nm of the electrode, lie flat on the surface with both hydrogen bonds saturated, denoted as double-donor (DD) species (Figure 4-4B). These molecules are characterized by an XAS spectrum with no substantial pre-edge feature. Another 49% of the interfacial water molecules have one broken hydrogen bond (single donor or SD), either parallel to the surface (SD$_\parallel$, 18%) or perpendicular with one hydrogen atom

pointing toward the gold surface (SD⊥, 31%). The population of molecules with broken hydrogen bond is substantially higher than 22% found in bulk water (Figure 4-4A).
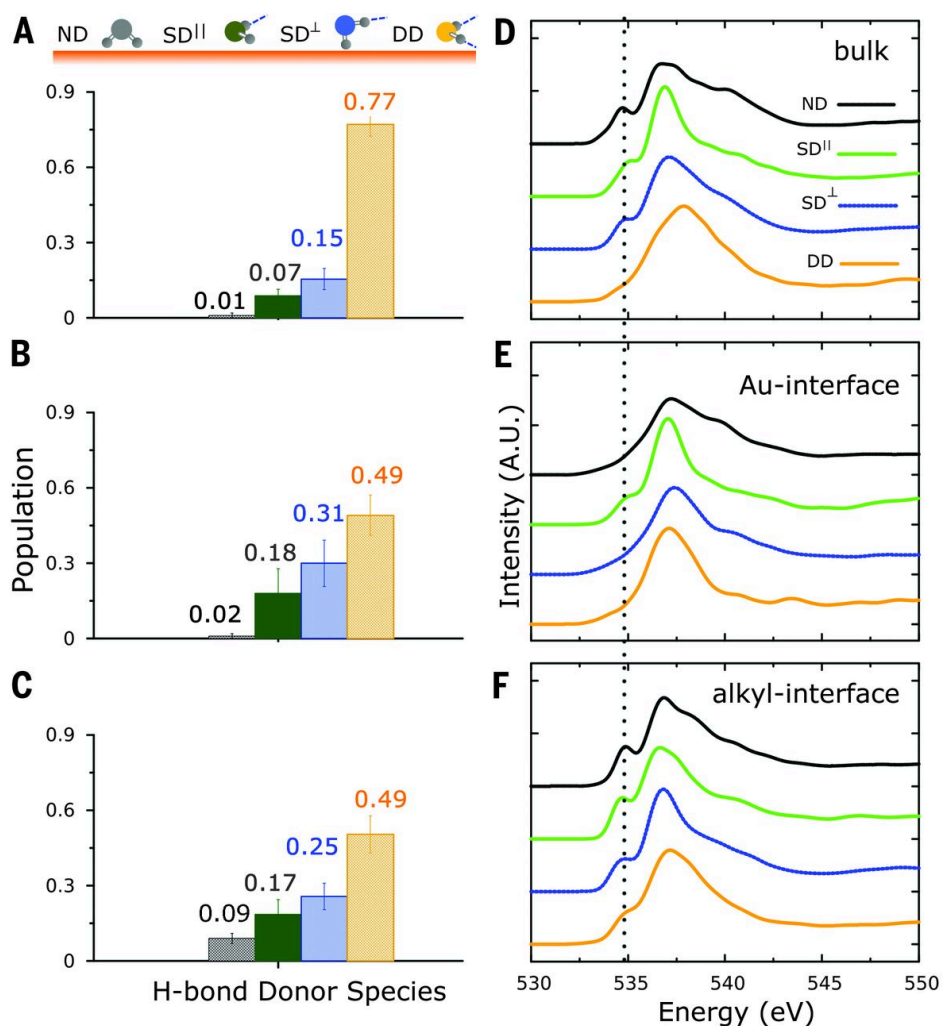

Figure 4-4. Populations of water molecules of various orientations obtained from AIMD simulations and calculated O*1s* XAS spectra.

Although the calculated XAS spectrum of SD∥ molecules resembles that of SD molecules in the bulk, with prominent pre-edge feature, the calculated XAS spectrum of those SD⊥ molecules does not present a pre-edge feature. Similarly, water molecules with two dangling hydrogen bonds (non-donor or ND species) are preferentially oriented with both hydrogen atoms pointing toward the gold surface and thus do not contribute to the pre-edge feature. Such suppression of the pre-edge feature of the SD⊥ species at the gold surface is a purely electronic effect. The core-excited state resulting from the absorption of a 535 eV x-ray photon is coupled to the gold band structure and delocalized over the surrounding gold atoms, as illustrated in Figure 4-5. This delocalization reduces the overlap of the core-excited electron with the *1s* core-hole at the excited oxygen atom,

thereby reducing the transition probability and thus the intensity of the corresponding peak. Furthermore, because the pre-edge peak arises from the anti-bonding σ* states centered on the hydrogen atom and extending directionally along the O-H bond vector, coupling to gold depends strongly on the orientation of the water molecule and affects primarily the water molecules in the first layer.
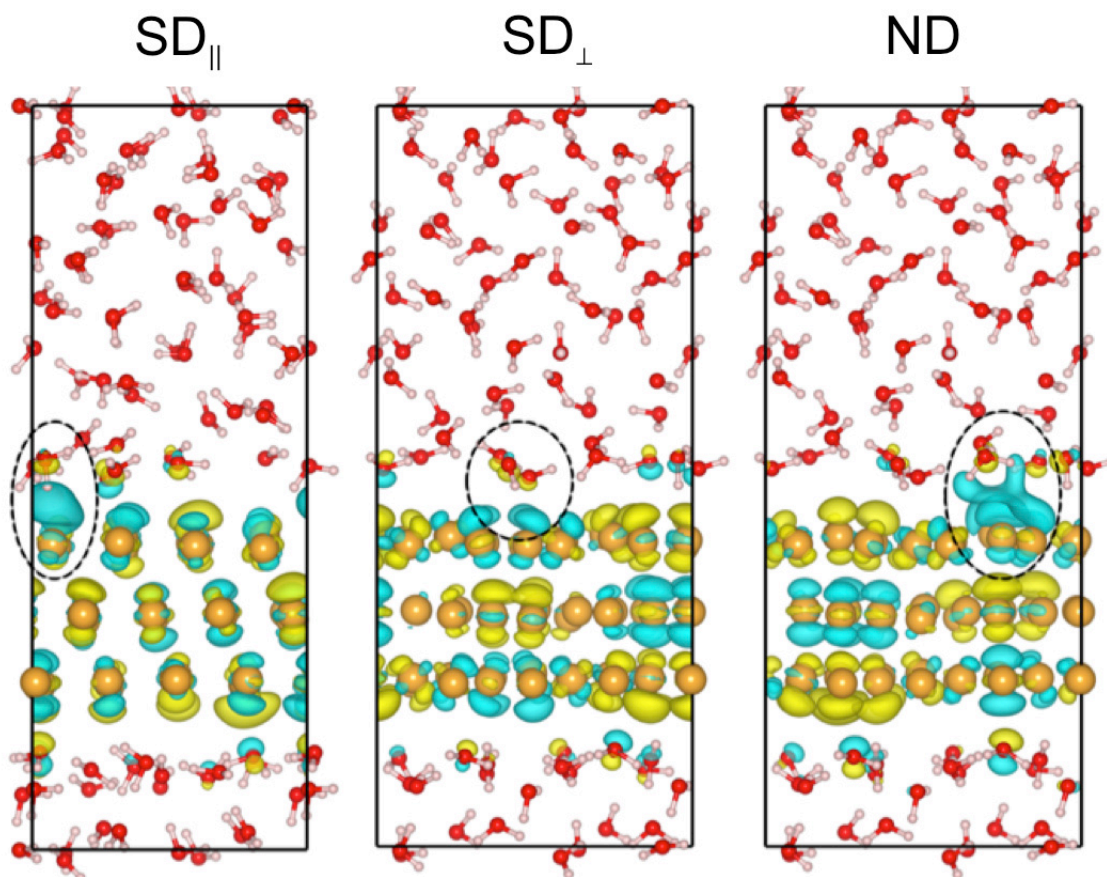

Figure 4-5. Schematic illustrations of the electronic coupling effects between the orbitals of gold atoms and the LUMO orbitals of the interfacial water molecules with broken hydrogen bonds.

The water molecules with broken hydrogen bonds in the second layer also have a reduced pre-edge intensity, although the reduction is only about 30% of that of the molecules in the first layer. The net result is that the overall XAS obtained from sampling the interfacial water molecules, i.e., first 2-3 layers of water molecules, shows a substantially reduced pre-edge feature. Curve (a) and (b) in Figure 4-6 are the weighted averages of the calculated O*1s* XAS spectra of bulk water and interfacial water based on the populations of water molecules of various orientations obtained from AIMD simulations. The spectral features in O*1s* TFY and TEY XAS spectra were qualitatively reproduced in the

calculated spectra. The good agreement between the calculated interfacial water XAS spectra and experimental TEY spectrum, confirmed the high interfacial sensitivity of XAS measurements in TEY detection mode.
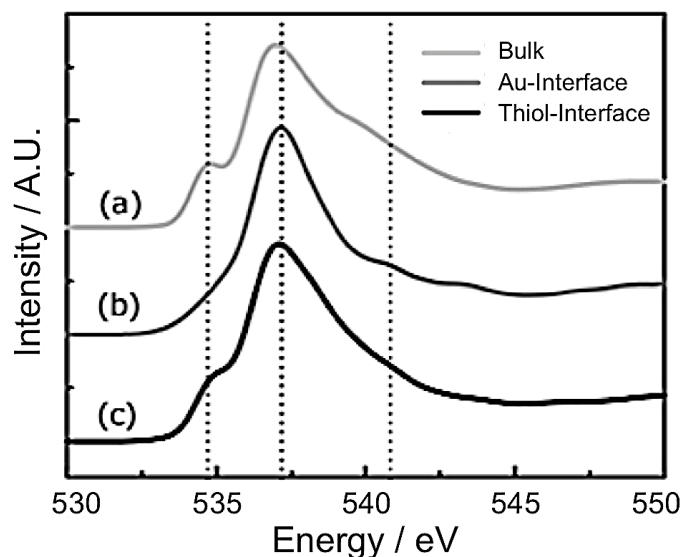

Figure 4-6. Weighted averages of the calculated O$1s$ XAS spectra based on the populations of water molecules of various orientations obtained from AIMD simulations.

4.1.4 The Interface between Thiol-Covered Gold Surface and Water

To verify that the suppression of the pre-edge feature in the XAS of interfacial water molecules is a result of electronic coupling to the gold electronic structure, a control experiment was performed, where the gold surface was fully covered with a monolayer of hexadecane-thiol ($C_{16}H_{33}SH$). This monolayer of thiol not only renders the surface hydrophobic, but also spatially separates the gold surface and water molecules. AFM images of this surface revealed the absence of defects that expose the gold substrate within the ~1 nm resolution of the technique.[4]

The AIMD results revealed an increase in the SD and ND populations at the interface (42% and 9%, respectively), compared to the bulk (22% and 1%, respectively), as shown in Figure 4-4C. The large population of SD and ND species from the AIMD simulations is consistent with the sum frequency generation (SFG) results by Shen et al., which showed a substantial amount of dangling hydrogen bonds in water at the alkyl-water interface.[11] Moreover, spectrum calculation indicate that the low-energy core-excited states of the interfacial SD and ND species are no longer coupled with the (now distant) gold and are highly localized on the excited molecules; therefore the pre-edge absorption feature is expected in the XAS spectra of the interfacial water molecules. Indeed, the

58

experimental O*1s* TEY XAS spectrum (curve (c) in Figure 4-3) and the calculated water spectrum at the thiol interface (curve (c) in Figure 4-6) both exhibit a prominent peak at 535 eV, characteristic of liquid water, whereas the TFY XAS remained the same as in the case of bare gold/water.

It is noteworthy that the photon flux at Beamline 8.0.1 is very intense, which can induce severe beam damage to the organic molecules upon continuous illumination. When the self-assembled thiol monolayer was continuously measured under x-ray beam, the TEY spectra evolved as a result of beam damage: Some spectral features below the pre-edge feature at 535 eV start to emerge, which is correlated to the hydroxyl and carboxyl groups. These species are very likely the decomposition products of the thiol molecules induced by the intense x-ray beam. Meanwhile, the pre-edge feature at 535 eV began to decrease, because the progressive decomposition of the hydrophobic thiol layer left increasing area of bare gold surfaces exposed to liquid water.

The pre-edge feature observed in the case of thiol-covered gold surface, as well as the disappearance of such feature upon decomposition of the thiol layer, proved that the electronic coupling between the interfacial water molecules and gold substrate is indeed the origin of the suppression of the pre-edge feature in the interfacial water spectra.

4.1.5 Potential-Dependent Reorientation of Water at Gold/Water Interface

Because water molecules have strong dipole moments (1.85 D), they are expected to respond to external electrical fields.[12] Infrared spectroscopy results have indeed suggested a bias-dependent orientation of water molecules by monitoring the intensity of O-H and O-H--O vibrational modes as a function of applied bias.[13] We thus investigated the influence of electric fields on the interfacial water structure in the EDL by *operando* XAS measurement.

The results are shown in Figure 4-7. At positive bias with respect to silver quasi-reference electrode, the pre-edge feature in the O*1s* TEY XAS spectrum remains suppressed, as in the case at open-circuit potential. Under negative bias, the pre-edge peak appears and grows when the potential is changed from -20 mV to -60 mV vs Ag. Given the fact that no electrochemical reactions or ion adsorption take place within such potential window, as evidenced by the CV measurement shown in Figure 4-2, a simple interpretation of the observations is that under negative bias, the electric field favors an orientation of the water molecules with their hydrogen atoms toward the gold surface, which increases the number of dangling hydrogen bonds.

According to electrochemistry theory, the surface of an electrode usually carries charges when immersed in a solution.[14] The sign and the quantity of the charges depend on the
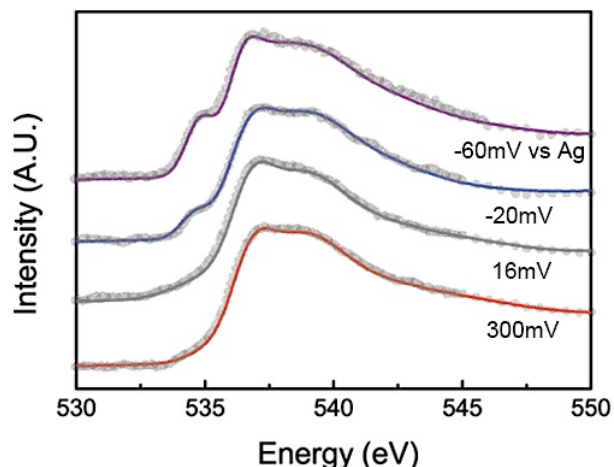
Figure 4-7. Potential-dependent O$1s$ TEY XAS spectra measured at Au/H_2O interfaces.

electrochemical potential that is applied to the electrode. At one particular potential, known as the point of zero charge (PZC), the surface becomes neutral. Accurate measurement of PZC is rather difficult, especially for polycrystalline electrodes. We used minimum capacitance measurement to estimate the PZC of the gold thin film electrode in the dilute NaCl solution. The results are shown in Figure 4-8. Each data point was calculated based on cyclic voltammetry curves within a 20 mV potential window centered at each potential. Based on the potential corresponding to the minimum capacitance, the PZC of the gold thin film was estimated to be around 80 mV with respect to Ag. This means that the charges on the gold surface and thus the direction of the electrical field are expected to switch sign around 80mV with respect to Ag. Our experimental data roughly agreed with this prediction, as the pre-edge feature first reappear and then grow when the applied potential drop below 80eV.
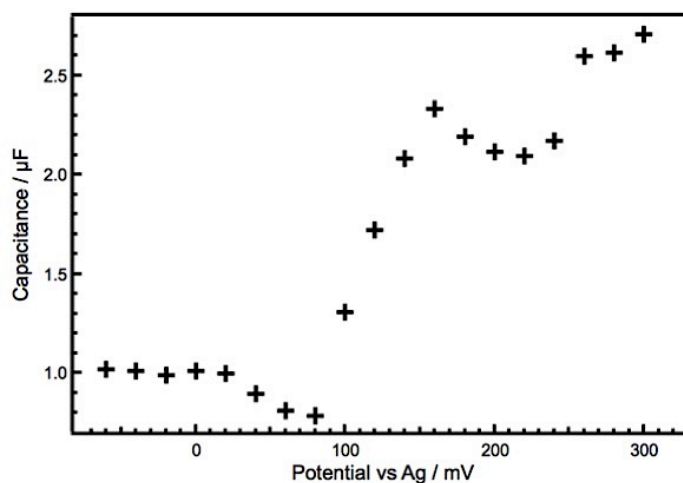

Figure 4-8. Minimum capacitance measurement on gold thin film electrode in 10μM NaCl solution.

The interpretation of potential-dependent spectral evolution was confirmed by the AIMD simulations, which showed an enhanced DD population at positive bias and an enhanced SD population (both SD⊥ and SD∥) at negative bias, as shown in Figure 4-9a. Indeed, the orientation of the water molecules was affected by applied bias, which, at negative bias, greatly disrupts the hydrogen-bonding network in the interfacial layer. This gives rise to an increased SD∥ population that causes a prominent pre-edge feature in the TEY XAS spectrum, as shown in both experimental (Figure 4-7) and calculated XAS spectra (Figure 4-9b).
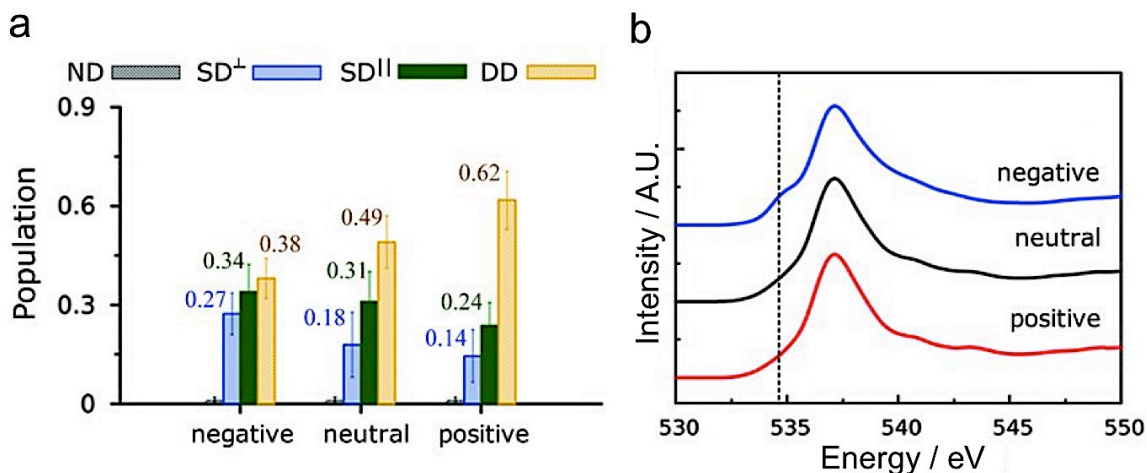

Figure 4-9. Populations of water molecules of various orientations at negative, neutral, and positive potentials, and calculated O*1s* XAS spectra based on the populations.

4.2 The Interface between Noble Metals and Sulfuric Acid Solution

Gold/water interface is a relatively simple system. Although in the 10 μmol/L NaCl solution, there are small amount of Na^+ and Cl^- (~10^{-5} mol/L) ions, as well as trace amount of H_3O^+ and OH^- ions (~10^{-7} mol/L) from self-dissociation of water, their concentration is too low to have noticeable impact on the hydrogen-bonding network on large scales. Considering that the effective concentration of water solvent is ~55 mol/L, the concentrations of H_3O^+ and OH^- ions are far below the detection limit of XAS in the O*1s* region. In addition, gold cannot be easily oxidized and is a relatively inert catalyst for the electrolysis of water. As a result, we can explore a relatively large potential window in our *in situ* characterization without introducing surface oxide or other surface reactions. All these factors make the gold/water interface a good proof-of-concept system for the demonstration of the new *in situ* and *operando* technique.

However, practical electrochemical systems are never this simple. Even the simplest ones, for example, Pt electrode in sulfuric acid, one classic system that has been studied

by numerous methods for decades, are much more complex compared to the gold/water system. Obviously, there are many different species in the solution: other than water molecules, H_3O^+ and SO_4^{2-} ions, considerable concentration of HSO_4^- and small amount of H_2SO_4 and OH^- are also present. In the bulk solution, the concentrations of these solute species are still small compared to that of water as solvent (~55 mol/L); therefore, their impact on the hydrogen-bonding network structure in the bulk solution is quite limited. However, at the solid/liquid interfaces, the situation can be completely different. Theory has predicted that the co-adsorption of multiple species can induce different superstructures at the interfaces between platinum and H_2SO_4 solution.[15] Furthermore, under different electrochemical conditions, the surface adsorption/reaction processes can not only alter the chemical composition of the interface, but also severely disrupt the hydrogen-bonding network structure of water molecules close to the interface.

The Pt/H_2SO_4 solution interface has already been studied by a few *in situ* characterization techniques. Electrochemical STM (EC-STM) studies revealed that sulfate ions can adsorb on single crystal Pt surfaces (as well as Au, Cu, and Pd) and form different ordered or disordered superstructure depending on the potentials applied to the electrode.[16–20] In some atomically resolved STM images,[18] one can even discern the adsorbates that exhibit three-fold symmetry, which very likely correspond to the tetrahedral SO_4^{2-} ions with three oxygen atoms landing on the metal surface. However, STM characterization is typically applied to flat surfaces on single crystal electrode. Other than STM, many other *in situ* techniques mostly provide indirect information, from which one can deduce the structure model. For example, *in situ* EXAFS or surface EXAFS measurements[21,22] can be used to determine the coordination numbers of Pt atoms, as well as the Pt-Pt, Pt-O, and Pt-S interatomic distances. Based on these structural parameters, an interface structure model can be constructed to match these experimentally determined parameters. *In situ* x-ray scattering has also been used to study $Pt/H_2SO_4(aq)$ and $Au/H_2SO_4(aq)$ interfaces.[23,24] To analyze the data, one usually needs to presume some interface structure based on the prior knowledge of the system, then simulate the scattering pattern of such presumed structure and compare that with the experimental data. Moreover, surface EXAFS and surface x-ray scattering typically require large flat sample surface, too. SFG vibrational spectroscopy can be used to study rough surfaces. But from SFG spectra, one can only obtain direct information regarding the chemical bonds that vibrate at the interface.[11] The structure models need to be deduced indirectly based on the collective information regarding all the bonds involved at the interface.

Until now it is still challenging to characterize such interface between Pt and H_2SO_4 solution, especially for polycrystalline electrodes with rough surfaces. As demonstrated in the case of gold/water interface, the newly developed *in situ* and *operando* XAS technique is a promising method for the investigation of solid/liquid interfaces.

4.2.1 Sample Preparation

The platinum thin film (15 nm), as the working electrode in this case, was evaporated onto the flat side of the Si_3N_4 window by an e-beam evaporator under 10^{-8} Torr base pressure. A thin titanium layer (2 nm) was deposited prior to the platinum deposition to achieve better adhesion between platinum thin film and the Si_3N_4 membrane. The platinum thin film is polycrystalline and continuous, and consists of agglomerated nanoparticles. The titanium adhesion layer is fully covered by platinum, as evidenced by the lack of titanium oxide signatures in the O$1s$ XAS TEY spectrum measured on a dry window. The gold thin film was prepared similarly as in the previous section. Standard 0.1N (0.05 mol/L) sulfuric acid solution was purchased from Sigma-Aldrich and used without any further purification or other treatment.

4.2.2 Potential-Dependent Spectral Evolution at Pt/H$_2$SO$_4$(aq) Interfaces

Under open circuit condition, the O$1s$ TEY XAS spectrum of Pt/H$_2$O interface is very similar to that of Au/H$_2$O interface: the pre-edge feature at ~535 eV is substantially suppressed, as shown in Figure 4-10. Nonetheless, as in the case of Au/H$_2$O, the pre-edge feature at ~535 eV does not completely disappear, which can be seen more prominently in the derivative spectrum in Figure 4-10. Similar suppression was also observed in the cases of Pt/H$_2$SO$_4$(aq) and Au/H$_2$SO$_4$(aq) interfaces. Such similarity indicates that in 0.1N H$_2$SO$_4$ solution, the concentration of solute species is not high enough to disrupt the interface water structure under open circuit condition.
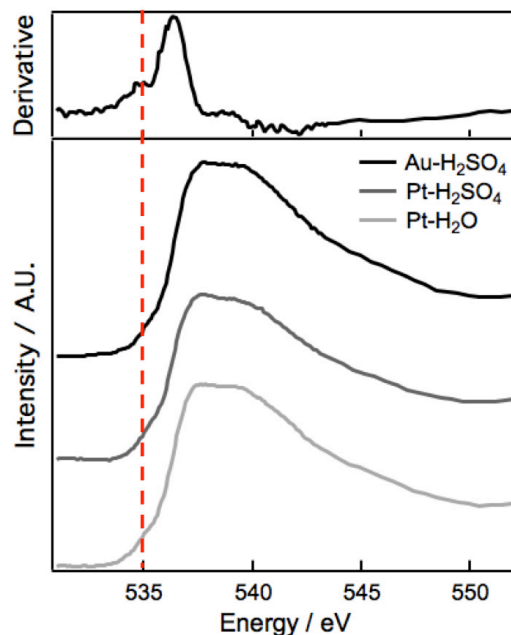

Figure 4-10. O$1s$ TEY XAS spectra measured at different interfaces. The top spectrum is the derivative of the Pt-H$_2$O spectrum in light grey.

Cyclic voltammetry measurement was performed inside the flow liquid cell with either a Ag quasi-reference electrode or a miniature Ag/AgCl reference electrode, and a Pt counter electrode. The result is consistent with the well-known shape of the CV curve for a Pt electrode immersed in H_2SO_4 solution,[14] as shown in Figure 4-11a. For comparison, CV curves measured from a single crystal Pt electrode[16] are presented in Figure 4-11b. Before reaching the oxygen evolution reaction (OER) potential, the broad feature starting from ~0.6V vs Ag/AgCl is commonly assigned to Pt oxide formation or oxygen/hydroxyl adsorption.[14,25-29] The negative peak showed in the opposite scanning direction is usually assigned to oxide reduction or oxygen/hydroxyl desorption. In our case this intense negative peak may also contain the reduction feature of the dissolved O_2 in the solutions.
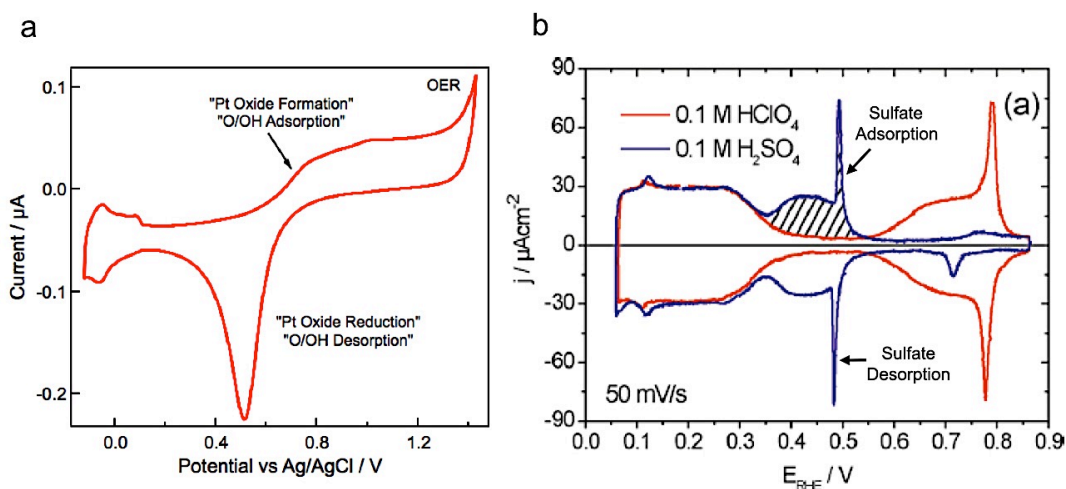

Figure 4-11. CV measurements of (a) the Pt thin film in 0.05M H_2SO_4 solution in the liquid cell; (b) single crystal Pt(111) electrode in $HClO_4/H_2SO_4$ solutions.[16]

During *operando* XAS measurements, the bias was applied between the working electrode (WE), i.e. the Pt thin film, and the Pt counter electrode (CE), by the SRS570 pre-amplifier, which has a bias output function. The reported potentials with respect to the reference electrode (RE), Ag or Ag/AgCl, were the average values of the measured potential difference between WE and RE, before and after the acquisition of each spectrum. Although it is feasible to directly use three-electrode configuration in the *operando* XAS measurement, such configuration introduces much higher level of noise in the TEY signal. The source of the noise is possibly associated with the feedback mechanism of the potentiostat, but is not entirely understood at this moment. Two-electrode configuration introduces much less noise and thus generates more reproducible results. However, the bias that can be applied between WE and CE has to be limited within the ±1.3V window to avoid water electrolysis, because the electrolysis reaction produces large volume of gases and leads to rapid pressure buildup and eventually the rupture of Si_3N_4 window. Between the double-layer capacitor region (~0.3V vs Ag/AgCl)

and the oxygen evolution region, which is referred to as the positive potential region in the following, the O$1s$ TEY XAS spectra change prominently with potential. Compared to the spectrum acquired at open circuit condition, a sharp pre-edge feature at ~534.8 eV emerges and grows with potential, as shown in Figure 4-12a. Different from the pre-edge feature that was observed at the Au/H$_2$O interface, the width of this new feature is noticeably smaller. In the case of Au/H$_2$O, the pre-edge feature typically grows like a shoulder; even when the height of the pre-edge feature grows up to about half of that of the main edge, no noticeable dip can be observed on the higher-energy side of the feature, as shown in Figure 4-7. In the Pt/H$_2$SO$_4$(aq) system, because of the smaller width of the pre-edge feature, a noticeable dip is always present on the higher-energy side of the peak, even when the intensity of the pre-peak is rather low, for example in the spectrum

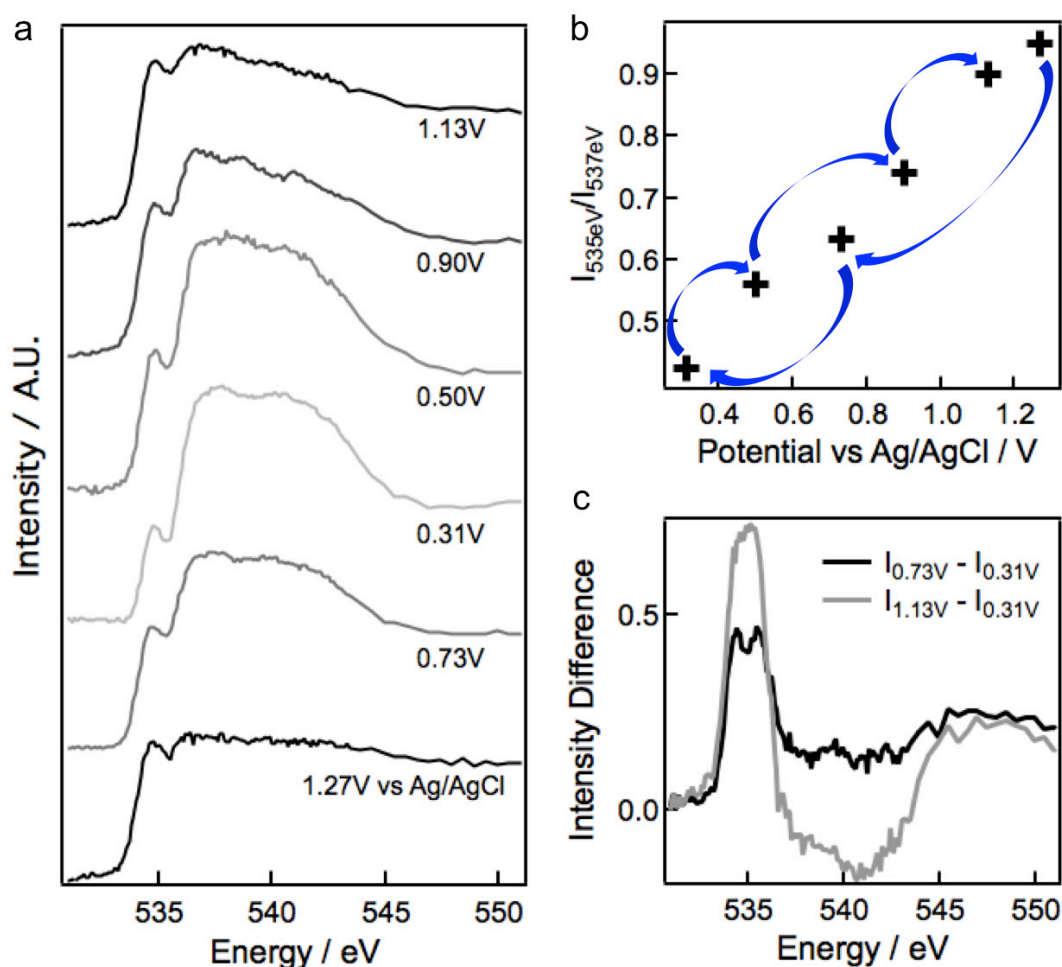

Figure 4-12. O$1s$ XAS measurements in the positive potential region. (a) O$1s$ TEY XAS spectra measured at different potentials. (b) The intensity ratios between the pre-peak and the main peak as a function of potential. Blue arrows highlight the order of the measurements. (c) The differences between the spectra measured at 0.73 V and 0.31 V, 1.13 V and 0.31 V (vs Ag/AgCl), respectively.

acquired at 0.31V vs Ag/AgCl. Moreover, the growth of the pre-peak is somewhat reversible. Figure 4-12b highlights the dependence of the pre-edge-to-main-edge ratio (I_{535eV}/I_{537eV}) on the electrochemical potential. The blue arrows indicate the order of spectrum acquisition. From 1.27 V to 0.31 V and then back to 1.13 V, the ratios roughly fall on the same trend.

Another subtle variation in the spectra shown in Figure 4-12a is the extension of the post-edge plateau towards higher energy when the potential becomes more positive. Such change can be better illustrated in the difference spectra as shown in Figure 4-12c. Other than the obvious sharp peak at ~535 eV, another broad feature can be seen above 540 eV.

Within the double-layer capacitor region, which is referred to as the negative potential region in the following, similar spectral changes were observed as in the case of Au/H$_2$O interface: a relatively broader feature emerges in the pre-edge region and grows with potential. Unfortunately, the spectra acquired in the negative potential region appear noisier than those in the positive region. Figure 4-13 shows one of the spectra (raw data and the fitted line) collected at the lowest possible potential (-1.25V between WE and CE), in comparison with two typical spectra acquired in the positive potential region. The height of the pre-edge feature is almost half of main-edge height. As discussed before, the dip on higher-energy side of the pre-edge feature is less prominent in the fitted spectra,
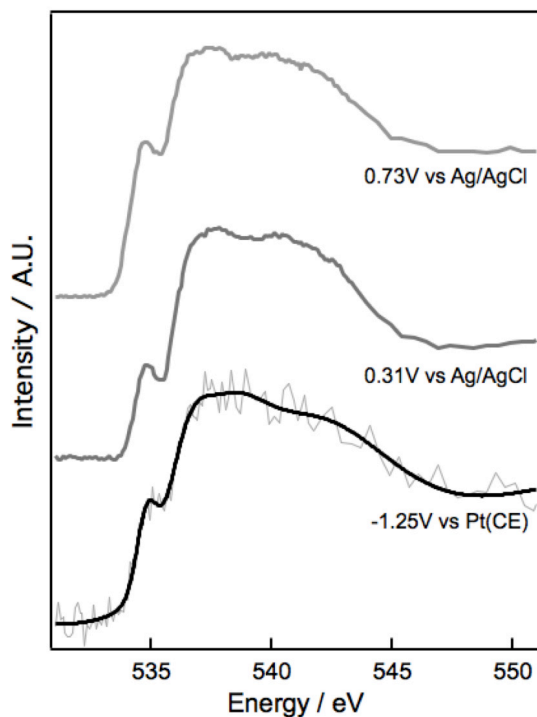

Figure 4-13. Comparison of typical O1s TEY XAS spectra measured in positive and negative potential regions.

compared to the spectra collected in the positive potential window.

4.2.3 First-Principle Spectra Calculations and Spectra Interpretation

Although potential-dependent spectral evolution was observed, the interpretation of these spectra is rather difficult. The difficulties mainly arise from the involvement of multiple species and the lack of reference spectra. Since there are many different ions/molecules possibly present at the interface, theory has predicted several different co-adsorption models at the interface, such as $H_2O + SO_4^{2-}$, $H_2O + H_3O^+ + SO_4^{2-}$, $H_2O + H_3O^+ + HSO_4^-$, etc.[15] When the electrochemical potential is positive enough, platinum oxide or hydroxide may start to form. These species all contain oxygen atoms and contribute to the overall O$1s$ signals. Therefore, proper deconvolution of the spectra may be necessary for quantitative analysis and interpretation. On the other hand, the O$1s$ reference spectra of several key species are unknown, such as hydronium ions and sulfate ions. Hydronium ions almost don't exist outside aqueous solutions. When they are mixed with large amount of water, their contribution to the overall O$1s$ spectra is almost negligible. Similar reason also makes the XAS measurement of solvated sulfate ions very difficult in aqueous solution. Without the reference spectra of these key species, it is almost impossible to interpret the potential-dependent spectra.
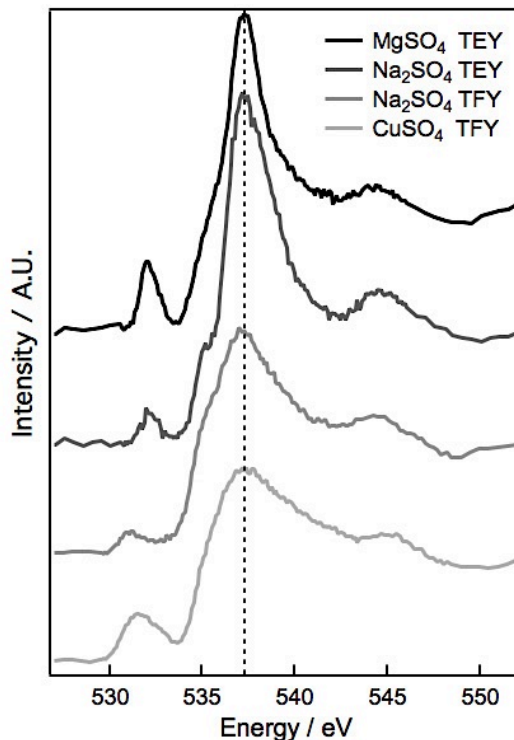

Figure 4-14. O$1s$ XAS spectra of various sulfate salts.

67

Although solid sulfate salt crystal can be readily measured by XAS, the O$1s$ spectra of the sulfate ions bound in an ionic crystal can be quite different from those of solvated sulfate ions. Figure 4-14 shows the O$1s$ XAS spectra of several different sulfate crystals. Two of the spectra were measured in the fluorescence mode (Na_2SO_4 and $CuSO_4$), while the other two in total electrode yield (TEY) mode ($MgSO_4$ and Na_2SO_4). All of the spectra exhibit three distinct features: a small peak centered at ~532 eV, a main peak at ~537 eV, and a broad feature around 545 eV. A small shoulder on the lower-energy side of the main peak, at ~535 eV, can be barely discerned. Clearly, the spectral features that grow in the positive potential region do not entirely match the salt spectra.

First-principle simulations prove to be a useful tool to help interpreting XAS spectra, as illustrated in the case of Au/H_2O interface[6] and several others.[30,31] In order to understand the physical origin of the changes in O$1s$ spectra, first-principle spectrum calculations were performed for sulfate ions and hydronium ions. Figure 4-15 shows the calculated O$1s$ XAS spectra of a hydronium ion, a sulfate ion, and a water molecule. Both ions are solvated by water molecules in the structure model. The main absorption edge in the hydronium ion spectrum appears at ~540 eV, higher than that of water molecule. It is because the third proton comes with an empty orbital, and the oxygen atom donates one of its lone electron pairs to this O-H bond, which reduces the electron density of the oxygen atom. The sulfate ion spectrum has a sharp pre-edge peak and an intense main
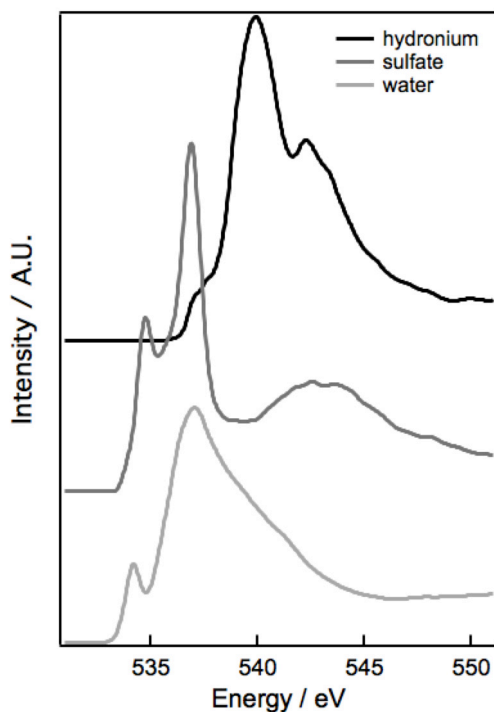

Figure 4-15. Calculated O$1s$ XAS spectra of hydronium ions, sulfate ions, and water molecules.

peak. The energy position of these two features is almost aligned with the pre-edge and main-edge features in the water spectrum, at ~535 eV and ~537 eV, respectively. However, both of them seem sharper in the sulfate ion spectrum. Another broad feature appears beyond the post-edge feature in water spectrum, between 540-550 eV, which is similar to the one seen in the sulfate salt spectra.

It is worth mentioning that as in the case of Au/H_2O interface, the electronic coupling between the interfacial species and the metal substrate was also observed in the calculations. When the sulfate ions and hydronium ions migrate to the close proximity of the platinum surface, the LUMO orbitals of both ions also delocalize by hybridizing with the platinum band structure. But the extent of suppression in the case of sulfate or hydronium ions is much less than that of water molecules. Therefore, in a qualitative analysis, such suppression can be neglected.

Comparing the calculated sulfate ion spectrum with the difference spectra in Figure 4-12c, the intense peaks at ~535 eV in the difference spectra possibly correspond to the pre-edge peak in the sulfate ion spectrum, given the fact that the pre-edge feature is substantially suppressed for the interfacial water molecules.[6] In experimental results, the observation of the intensity dip on the higher-energy side of the pre-peak also partially corroborate the finding in the calculations that the spectrum of sulfate ion exhibits a sharper pre-peak compared to water. The residual intensity at the higher-energy end in the difference spectrum is likely associated with the board post-edge feature of sulfate ions. Around the main-edge position, the calculated spectra of water molecules and sulfate ions both present intense peaks; therefore, the difference would depend on the ratio of these two species at the interface, as well as the detailed difference in the intensity of their main-edge features. Considering the sharpness of the pre-peak in the sulfate ion spectrum and the lack of other intense features in the pre-edge regions in other spectra, the intensity of the pre-peak (or pre-peak/main-peak ratio) is a reasonable indicator of the presence of sulfate ions on the Pt surface. As shown in Figure 4-12b, the pre-peak/main-peak ratio is positively correlated to the potential applied to the Pt working electrode, indicative of the increase in sulfate ion coverage with positive potentials.

The accumulation of sulfate ions at the Pt/H_2SO_4(aq) interface may have other consequences apart from simply excluding water and other absorbates. Accompanying the accumulation of the anions, negative charges will also build up at the interface, which can attract more cations into the double layer. Moreover, large concentration of sulfate ions at the interface can profoundly alter the hydrogen-bonding network of interfacial water molecules. Each of these effects can lead to variations in the O$1s$ XAS spectra. The absence of discernible features around 540 eV indicates that the concentration of hydronium ions is not high enough for XAS detection. The information regarding the

changes in hydrogen-bonding network is probably convolved with the substantial spectral change resulting from sulfate accumulation, and is extremely difficult to extract.

In the negative potential region, the feature corresponding to the hydronium ions around 540eV is still absent in the O$1s$ XAS spectra, indicating that the mass accumulation of hydronium ions may require more negative potentials. Instead, similar trend as in the case of Au/H$_2$O system was observed: as the potential goes more negative, the pre-edge feature grows up. This indicates that within the double-layer capacitor region, the water molecules can reorient themselves, like those at the Au/H$_2$O interfaces.

Although the broad peak around +0.6V vs Ag/AgCl in the CV curves measured with polycrystalline Pt electrode is commonly assigned as oxide formation or oxygen/hydroxyl adsorption in the literature,[14,25–29] our result says otherwise. XAS spectra of platinum oxides and various surface oxygen species on platinum were measured *in situ* by Miller et al. in an AP-XPS chamber, all of which present a main absorption edge at ~530 eV in the O$1s$ region.[32] None of our TEY XAS spectra exhibit discernible features around 530 eV. Based on our findings from *in situ* and *operando* XAS experiments, we believe that sulfate ion adsorption is the main chemical process that occurs within the broad peak region, starting from 0.6V vs Ag/AgCl in the CV curves measured with polycrystalline Pt electrode. Unlike the sharp peaks related to sulfate ion adsorption in the CV curves of single crystals, the peak in the case of polycrystalline Pt electrode is substantially broadened, possibly because many different facets are present on the polycrystalline surface, along with many edges, kinks, and grain boundaries. Platinum oxides may start to form when the electrolysis reaction starts at higher potentials, but unfortunately our liquid cell cannot accommodate fast gas evolution at this moment. It has to be pointed out that our results cannot rule out the oxidation of Pt at the interface, but it is clear that if oxidized, Pt doesn't bond to oxygen or hydroxyl group directly, but possibly coordinate with adsorbed sulfate anions.

4.2.4 Potential-Dependent Spectral Evolution at Au/H$_2$SO$_4$(aq) Interfaces

Similar sulfate adsorption phenomena have been observed by EC-STM on several other single crystal metal surfaces, such as Au, Cu, and Pd.[18–20] To corroborate the results on Pt/H$_2$SO$_4$(aq) interface, similar experiments were performed on a gold electrode in 0.05 mol/L H$_2$SO$_4$ solution.

Within the potential window that is accessible with a two-electrode configuration, the potential-dependent trend in O$1s$ TEY XAS spectra is similar to that at Pt/H$_2$SO$_4$(aq) interface, as shown in Figure 4-16. Within positive potential window, a sharp pre-peak at ~535 eV related to sulfate ion adsorption grows with increasing potential, accompanied

by an extension of the post-edge plateau to higher energy. At around +0.46V vs Ag/AgCl, almost all the sulfate ions desorb from the interface and the O$1s$ spectrum resembles the one measured at open circuit condition. When the potential goes more negative, water molecules start to reorient at the interface, creating more broken hydrogen bonds. As a result, a pre-edge feature emerges at ~535 eV, but no extension of the post-edge feature can be observed.

The spectral evolution is also reversible in this case. After measured in the negative potential region for several hours, a positive potential (0.70V vs Ag/AgCl) was applied to the working electrode. The sulfate-related sharp pre-peak, as well as the extension of the post-edge feature appeared once again in the O$1s$ TEY XAS spectrum.
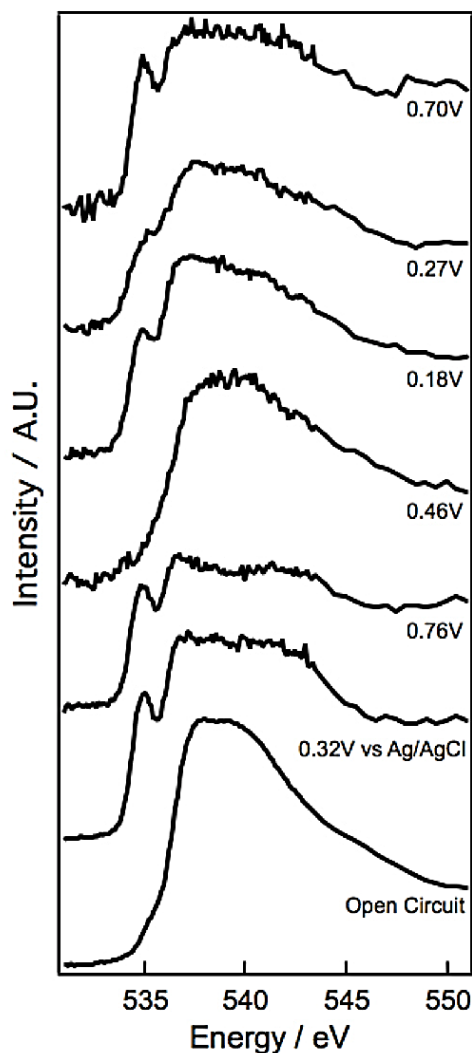

Figure 4-16. Potential-dependent O$1s$ TEY XAS spectra measured at Au/H$_2$SO$_4$(aq) interface.

This experiment revealed similar interfacial phenomena at Au/H₂SO₄(aq) interface. It also further excludes the existence of oxides formation within the potential window in this measurement, because gold is very difficult to oxidize.

4.3 Conclusions

The results presented above demonstrate the power and the potential of the newly developed *in situ* and *operando* XAS technique. The combination of *in situ* and *operando* XAS characterization and first-principle simulations helped elucidate the chemical processes that happened at the solid/liquid interfaces.

At Au/H₂O interface, the hydrogen-bonding network is largely disrupted by the interface, leaving more broken hydrogen bonds than in bulk water. But the delocalization of the LUMO orbitals of water molecules into the gold substrate, greatly suppresses the pre-edge feature that is typically associated with broken hydrogen bonds. These interfacial polar molecules can respond to external electrical field and reorient, producing potential-dependent O*1s* TEY XAS spectra.

At Pt/H₂SO₄(aq) or Au/H₂SO₄(aq) interfaces, similar water reorientation behaviors were observed in the negative potential region. In the positive potential regions, the spectral evolution is different from that of Au/H₂O system. The changes in the spectra are possibly related to the sulfate ion adsorption at the interface, contradicting many reports that proposed an oxide formation or oxygen/hydroxyl adsorption processes.

4.4 References

1   L. R. Pratt, *Chem. Rev.*, 2002, **102**, 2625–2626.
2   L. Pauling, *The Nature of the Chemical Bond and the Structure of Molecules and Crystals: An Introduction to Modern Structural Chemistry*, Cornell University Press, Ithaca, NY, 1960.
3   A. Nilsson, D. Nordlund, I. Waluyo, N. Huang, H. Ogasawara, S. Kaya, U. Bergmann, L.-Å. Näslund, H. Öström, P. Wernet, K. J. Andersson, T. Schiros and L. G. M. Pettersson, *J. Electron Spectros. Relat. Phenomena*, 2010, **177**, 99–129.
4   G. Liu and M. Salmeron, *Langmuir*, 1994, **10**, 367–370.
5   D. Prendergast and G. Galli, *Phys. Rev. Lett.*, 2006, **96**, 215502.
6   J. J. Velasco-Velez, C. H. Wu, T. A. Pascal, L. F. Wan, J. Guo, D. Prendergast and M. Salmeron, *Science*, 2014, **346**, 831–834.

7   L. Näslund, J. Lüning, Y. Ufuktepe, H. Ogasawara, P. Wernet, U. Bergmann, L. G. M. Pettersson and A. Nilsson, *J. Phys. Chem. B*, 2005, **109**, 13835–9.

8   J.-H. Guo, Y. Luo, A. Augustsson, S. Kashtanov, J.-E. Rubensson, D. K. Shuh, H. Ågren and J. Nordgren, *Phys. Rev. Lett.*, 2003, **91**, 157401.

9   D. Emfietzoglou and H. Nikjoo, *Radiat. Res.*, 2007, **167**, 110–120.

10   B. Frazer, B. Gilbert, B. Sonderegger and G. De Stasio, *Surf. Sci.*, 2003, **537**, 161–167.

11   Y. R. Shen and V. Ostroverkhov, *Chem. Rev.*, 2006, **106**, 1140–54.

12   M. F. Toney, J. N. Howard, J. Richer, G. L. Borges, J. G. Gordon, O. R. Melroy, D. G. Wiesler, D. Yee and L. B. Sorensen, *Nature*, 1994, **368**, 444.

13   K. Ataka, T. Yotsuyanagi and M. Osawa, *J. Phys. Chem.*, 1996, **100**, 10664–10672.

14   A. J. Bard and L. R. Faulkner, *Electrochemical Methods: Fundamentals and Applications*, Wiley, 1980.

15   A. Comas-Vives, J. Bandlow and T. Jacob, *Phys. Chem. Chem. Phys.*, 2013, **15**, 992–997.

16   B. Braunschweig and W. Daum, *Langmuir*, 2009, **25**, 11112–11120.

17   A. M. Funtikov, U. Linke, U. Stimming and R. Vogel, *Surf. Sci.*, 1995, **324**, L343–L348.

18   Y. G. Kim, J. B. Soriaga, G. Vigh and M. P. Soriaga, *J. Colloid Interface Sci.*, 2000, **227**, 505–509.

19   D. M. Kolb, *Angew. Chemie - Int. Ed.*, 2001, **40**, 1162–1181.

20   M. Wilms, P. Broekmann, M. Kruft, Z. Park, C. Stuhlmann and K. Wandelt, *Surf. Sci.*, 1998, **402-404**, 83–86.

21   E. L. Redmond, B. P. Setzler, F. M. Alamgir and T. F. Fuller, *Phys. Chem. Chem. Phys.*, 2014, **16**, 5301–11.

22   D. Koningsberger and B. Mojet, *Top. Catal.*, 2000, **10**, 143–155.

23   T. Kondo, J. Morita, K. Hanaoka, S. Takakusagi, K. Tamura, M. Takahasi, J. Mizuki and K. Uosaki, *J. Phys. Chem. C*, 2007, **111**, 13197–13204.

24   T. Kondo, T. Masuda, N. Aoki and K. Uosaki, in *224th ECS Meeting*, 2013, p. Abstract 2623.

25   H. Angerstein-Kozlowska, B. E. Conway and W. B. A. Sharp, *J. Electroanal. Chem. Interfacial Electrochem.*, 1973, **43**, 9–36.

26   G. Jerkiewicz, G. Vatankhah, J. Lessard, M. P. Soriaga and Y. S. Park, *Electrochim. Acta*, 2004, **49**, 1451–1459.

27   A. A. Topalov, S. Cherevko, A. R. Zeradjanin, J. C. Meier, I. Katsounaros and K. J. J. Mayrhofer, *Chem. Sci.*, 2014, **5**, 631.

28   S. Xiao, F. Xiao, Y. Hu, S. Yuan, S. Wang, L. Qian and Y. Liu, *Sci. Rep.*, 2014, **4**, 4370.

29   N. Ramaswamy and S. Mukerjee, *Adv. Phys. Chem.*, 2012, **2012**, 1–17.

30   T. Pascal, K. Wujcik, J. Velasco-Velez, C. Wu, A. Teran, M. Kapilashrami, J. Cabana, J. Guo, M. Salmeron, N. Balsara and D. Prendergast, *J. Phys. Chem. Lett.*, 2014, **5**, 1547–1551.

31   K. H. Wujcik, J. Velasco-Velez, C. H. Wu, T. Pascal, A. A. Teran, M. A. Marcus, J. Cabana, J. Guo, D. Prendergast, M. Salmeron and N. P. Balsara, *J. Electrochem. Soc.*, 2014, **161**, A1100–A1106.

32   D. J. Miller, H. Öberg, S. Kaya, H. Sanchez Casalongue, D. Friebel, T. Anniyev, H. Ogasawara, H. Bluhm, L. G. M. Pettersson and A. Nilsson, *Phys. Rev. Lett.*, 2011, **107**, 195502.

Chapter 5

Summary and Outlook

Abstract

This chapter summarizes all the studies presented in this dissertation as well as their significance in fundamental understanding of reaction mechanisms and future design of better catalysts. Some limitations of current AP-XPS and *in situ* XAS technique are also discussed, and possible solutions and optimizations are proposed.

5.1 Summary

Many gas-phase catalytic reactions and electrochemical reactions have important industrial applications. All of these applications have similar goals: high efficiency, low cost, and minimum environmental impact. In order to achieve these goals, designing better catalysts and electrode materials is the key. The first step towards designing better catalysts or electrode materials is to understand the reaction mechanisms of existing systems, particularly the interfacial phenomena in these heterogeneous reactions. The goal of this dissertation is to use x-ray photoelectron spectroscopy (XPS) and soft x-ray absorption spectroscopy (sXAS) to investigate some relevant solid/gas and solid/liquid interfaces under reaction conditions.

XPS and sXAS are two element-specific and chemical-state-specific characterization techniques, but traditional XPS and sXAS instrument operates in ultra-high vacuum environment. Recently, researchers have demonstrated that with proper modifications, these vacuum-requiring techniques can be used to characterize solid/gas or solid/liquid interfaces under ambient conditions, which opens the way towards *in situ* and *operando* characterization of many heterogeneous reaction systems.

In the study regarding Co catalyst for Fischer-Tropsch (F-T) synthesis, AP-XPS characterization confirmed that CO adsorbs strongly on Co surface and desorbs at around 90°C. Small amount of sulfur contamination on the Co surface substantially weakens the CO adsorption and thus poisons the reaction. Under reaction conditions, the Co surface remains metallic. The water molecules in the reaction products can potentially oxidize the Co surface and consequently hinder the catalytic reaction at lower temperature. When the reaction temperature is above 250°C, H_2 is responsible for reducing Co to metallic phase and keeping the catalyst active. These findings corroborated the empirical knowledge obtained from industrial practice and helped the understanding of the reaction mechanism in Co-catalyzed F-T reactions.

In the study of Co_xPd_y alloy nanoparticles for catalyzing CO oxidation reaction, the dependence of catalytic activities on the nanoparticle compositions was explained by surface segregation of CoO_x and synergetic mechanism of coexisting Co/CoO_x and Pd on the catalyst surface, revealed by AP-XPS measurements. Such synergetic effect can be useful for designing other multi-component catalysts for CO oxidation and other similar reactions.

Two solid/liquid systems were characterized by our newly developed *in situ* and *operando* XAS technique. XAS results combined with first-principle simulations confirmed the potential-dependent reorientation behavior of water molecules at the

Au/H$_2$O interfaces, which has been proposed by other researchers based on indirect evidences provided by vibrational spectroscopy and surface x-ray scattering techniques. In the Pt/H$_2$SO$_4$(aq) and Au/H$_2$SO$_4$(aq) systems, potential-dependent XAS spectra indicated sulfate ion adsorption at the interface with unnoticeable Pt oxide or hydroxide species in the positive potential regions, which challenged the long-established "Pt oxide formation" or "oxygen/hydroxyl adsorption" mechanism within such potential window.

All four cases presented here in this dissertation illustrate the power of these two *in situ* and *operando* x-ray spectroscopy techniques, i.e., AP-XPS, and *in situ*/*operando* XAS. The information acquired from these experiments not only helped elucidate the reaction mechanisms and other fundamental aspects in these heterogeneous reactions, but also provided useful insight to guide the material design for the applications based on these reactions.

5.2 Outlook

At current stage, most AP-XPS instrument can tolerate pressures up to several Torr.[1] Although the characterization under such conditions provides much more relevant information of solid/gas interfaces compared to traditional surface science techniques operating in UHV, the accessible pressure range is still far below that in the actual industrial applications. Some of the industrial applications require tens or even a hundred of atmospheric pressure, 4 or 5 orders of magnitude higher than the maximum operating pressure in AP-XPS. Such pressure gap seems unlikely to be overcome by current AP-XPS instrumentation.

As discussed in Chapter 2, similar design as the flow liquid cell can be used to design an *in situ* gas cell.[2] Depending on the mechanical strength of the Si$_3$N$_4$ membranes, the gas cell can tolerate much higher pressure than AP-XPS instrument. For example, the 100nm-thick Si$_3$N$_4$ membranes that were used in the liquid cell experiments are able to sustain a pressure difference up to 3-4 bar. With slightly thicker membranes, even higher pressure can be achieved in the gas cell, with some sacrifice in the transmitted x-ray photon flux. As demonstrated by Tuxen et al.,[3] such gas cell can be useful when studying gas-phase catalytic reactions involving 3d transition metal and their oxides.

As for the study on solid/liquid interfaces, one of the obvious shortcomings is the incompatibility with gas evolution reactions. The closed tiny reaction chamber with only two small-diameter outlets cannot accommodate rapid pressure buildup in gas evolution reactions. One possible solution is to design a third outlet that connects the reaction chamber directly with the atmosphere, allowing immediate pressure release during gas

evolution. Nevertheless, rapid bubble formation at the solid/liquid interfaces, as well as the ionized gas molecules produced by x-ray photons, raises serious concerns about signal interference.

Another promising approach to investigate solid/liquid interfaces is to use the thinnest possible materials, e.g., graphene, graphene oxide, and other two-dimensional (2D) materials, as the membrane. These 2D materials, with just one or few layers of atoms, are transparent to not only x-ray photons but also electrons, as demonstrated in many recent *in situ* TEM studies using graphene liquid cells.[4,5] Such electron-transparency makes it possible to collect photoelectrons ejected from the materials sealed underneath these membranes. As demonstrated by Kolmakov et al.,[6] a single layer of graphene oxide is mechanically robust enough to seal ambient-condition solutions underneath for XPS measurement. Our group is currently developing new liquid cells with such ultra-thin windows. Current AP-XPS instrument can only be used to study liquid samples in equilibrium with their vapors, or more precisely liquid/vapor interfaces. If successfully made, the liquid cells with ultra-thin membranes will enable *in situ* XPS measurement of real ambient-condition liquid. Furthermore, partial electron yield (PEY) or Auger electron yield (AEY) XAS spectra of the ambient liquid can also be collected by the electron analyzer in the XPS chamber. As explained in Chapter 2, these two detection modes collect electrons with specific kinetic energies or within a narrow kinetic energy window, which provide information with more well-defined probing depth.

5.3 References

1   M. Salmeron and R. Schlogl, *Surf. Sci. Rep.*, 2008, **63**, 169–199.

2   C. Escudero, P. Jiang, E. Pach, F. Borondics, M. W. West, A. Tuxen, M. Chintapalli, S. Carenco, J. Guo and M. Salmeron, *J. Synchrotron Radiat.*, 2013, **20**, 504–508.

3   A. Tuxen, S. Carenco, M. Chintapalli, C.-H. Chuang, C. Escudero, E. Pach, P. Jiang, F. Borondics, B. Beberwyck, A. P. Alivisatos, G. Thornton, W.-F. Pong, J. Guo, R. Perez, F. Besenbacher and M. Salmeron, *J. Am. Chem. Soc.*, 2013, **135**, 2273–8.

4   J. M. Yuk, J. Park, P. Ercius, K. Kim, D. J. Hellebusch, M. F. Crommie, J. Y. Lee, A. Zettl and A. P. Alivisatos, *Science*, 2012, **336**, 61–64.

5   Q. Chen, J. M. Smith, J. Park, K. Kim, D. Ho, H. I. Rasool, A. Zettl and A. P. Alivisatos, *Nano Lett.*, 2013, **13**, 4556–4561.

6   A. Kolmakov, D. A. Dikin, L. J. Cote, J. Huang, M. K. Abyaneh, M. Amati, L. Gregoratti, S. Günther and M. Kiskinova, *Nat. Nanotechnol.*, 2011, **6**, 651–657.